The Physics of Early Drosophila Development

Claudio Hernández-López

SORBONNE UNIVERSITÉ

LPENS
LABORATOIRE DE PHYSIQUE DE L'ÉCOLE NORMALE SUPÉRIEURE

THÈSE DE DOCTORAT
DE LA SORBONNE UNIVERSITÉ

Spécialité : Physique

École doctorale n°564: Physique en Île-de-France

réalisée

au Laboratoire de Physique de l'École Normale Supérieure

sous la direction de Massimo VERGASSOLA

présentée par

Claudio HERNÁNDEZ-LÓPEZ

pour obtenir le grade de :

DOCTEUR DE LA SORBONNE UNIVERSITÉ

Sujet de la thèse :

La Physique du Développement Précoce de la Drosophile

soutenue le 26ème septembre 2024

devant le jury composé de :

Mme	Nathalie DOSTATNI	Présidente du Jury
M.	Matthias MERKEL	Rapporteur
M.	Karsten KRUSE	Rapporteur
Mme	Claude LOVERDO	Examinatrice
M.	Boris SHRAIMAN	Examinateur
M.	Massimo VERGASSOLA	Directeur de thèse

Table des matières

Remerciements

I would like to begin by thanking my thesis supervisor Massimo Vergassola. Not only a very sharp (intellectually and wardrobe-wise) person but very kind and understanding. There were many challenging moments during the development of this work, most of the time unrelated to its content in itself, yet you were always extremely supportive. One of the moments that inspired me to start working with you was during the first lecture of the biophysics lecture you were giving in the ENS ICFP M1 program, where you showed various videos of waves in biological systems, in particular during the development of *Drosophila Melanogaster*. I hope you keep inspiring other students to find their way in research and be amazed at what the natural world has in store for us.

I thank Stefano di Talia, alias "Mister Físico", for your constant input and support in the development of this work. Not having done any experiments myself in many years, our meetings made me realize how important it is to stay in touch with reality and know the constraints of biological systems. I was so happy to meet you in Paris in 2024 after years of talking to you on Zoom. I also thank the rest of our experimental collaborators : Alberto Puliafito, Yitong Xu, and Ziqi Lu.

Je voudrais remercier les membres du jury, Nathalie Dostatni, Matthias Merkel, Karsten Kruse, Claude Loverdo, et Boris Shraiman pour leur disponibilité, leur évaluation, et nos échanges lors de la soutenance. Je remercie aussi Vincent Hakim et Martine Ben-Amar d'avoir fait partie de mon comité de suivi de thèse pendant ces années, et de leur feedback constructif, non seulement sur le déroulement de ma thèse, mais aussi sur mon désir de poursuivre un postdoctorat.

I am very grateful to the people in my lab, who have made this experience an incredible one. Those lunches by Rue Mouffetard, getting a sandwich at the Lebanese market in Place Monge, or my classic Bibimbap would not have been the same without you guys. Thank you Marie for all the fun conversations that we had, ranging from French politics on Twitter and cat memes, to our civilized fights for computing time in the Procida cluster. Thank you Argo for your input, physical insight, and your help in revising part of this work. I have enjoyed our collaborative back and forth which has led to some of the results that I am showing here. I wish you the very best in the new joys and challenges that are coming into your life. Thank you Antonio for being so supportive and nice, I want to thank you especially for those conversations we had in AQV about life and Brazilian funk. Thank you Jacqueline for all the funny moments that we shared in the office and La Montagne. Even if you were the last one to join the gang, your arrival brought me so much joy. Thank you Nicola for bringing your big bobo energy every day and our interesting discussions about so many topics.

My experience in Paris would not have been the same without all the incredible people

that I've met, especially during my stay in Cité Universitaire. I want to thank Gia for so many wholesome moments, either cooking together, listening to Ben & Ben, talking about our lives, or in the Norway house library. Thank you Gourangi for joining me on multiple bobo ice cream hunting missions in the city, you've always been very nice and supportive. Abir, for our numerous inspiring scientific and silly conversations, but above all, for our shared soft spot for Nolan's movies and a very particular Ed Sheeran song. Ingrid, we shared so many fun tennis sessions, gossip lunches, and nice moments in Paris and Oslo. Thank you Eline for joining me on oh-so-many concerts at the Philharmonie de Paris, our cultural discussions illuminated my days, and I have learned so much about cinema thanks to you. Thank you Rafi aka "poto galactique", Okan, Jason, and Frith for letting me crash in your rooms so many times during my apartment hunting season. Thank you, Ellen and Antoine, for always organizing fun board game sessions and apéros, and also revising some of this manuscript. Bad boy Odin helped me write a little as well ! Y a Andrea Iglesias, que siempre disfruto cuando salimos a comer por ahí o tenemos una conversación, apoyando con todo.

Agradezco profundamente a mi familia por acompañarme a la distancia en estos procesos. A mi papá, Claudio, por inspirarme a esforzarme en mi carrera. Quisiera recordar aquellos momentos de antaño en que llegabas a la casa con tu casco de ingeniero o con tus planos, y yo tan contento de ponerme el casco y rallar los planos. A mi mamá, Yasna, por escribirme todos los días. Yo sé que el alejamiento fue muy difícil en un principio para tí, pero creo que en la distancia hemos sabido siempre encontrarnos. A mi hermano, Alonso, por darme momentos llenos de luz y risas. Te veo tan grande cada vez que voy de viaje a Chile, y ahora estudiando biología. Estoy muy orgulloso de que seas un niño muy bueno.

Quisiera agradecer a mis amigos en Chile, particularmente a quienes conocí hace muchos años, y de quienes me distancié en 2019 una vez que me mudé a París. A Felipe Avello, por inspirarme en las ciencias y tu visión sobre la vida. A Felipe Urcelay, por tantas conversaciones desde Dream Theater a Ghibli. A Héctor Zúñiga, por todos esos momentos musicales en diversos projekcts. A Maria José Vergara, por tantas risas, tu bondad y apañe desde aquellos años de Crea+. A Santiago Abeliuk, por tu pasión tanto artística como de director. A Gabriel Ordoñez, por tu activismo y sentido de entrega. A Felipe Gallardo, por aquellas tardes de cine y de Smash Bros.

Quiero agradecer también a mi supervisor de tesis de licenciatura Gustavo Düring. Siempre me apoyaste en momentos claves antes de mi postulación a Francia, y ahora eres un gran colaborador.

Quiero dar un caluroso agradecimiento también a quienes fueron profesores de ciencias increíbles durante mi paso en el colegio San Ignacio en Santiago, ellos son Daniela Frigerio, Edgardo Alegría, y Javier Guzmán. Gracias por inspirarme, por una que otra conversación fuera de clase para responder a mis locas preguntas. Reconozco inmensamente su labor como docentes, y espero que sigan inspirando a más estudiantes a cumplir sus sueños.

Y un último cariñoso reconocimiento para mi primo Vicentín, quien luchó por años contra una terrible enfermedad neurodegenerativa, dejando su vida terrenal y llenándose de paz el día 23 de Mayo del año 2023. Me pesa en el alma haber estado tan lejos de tí estos años, en que te veía cada vez más cansado. Son incontables las memorias que tengo contigo, el niño más fuerte que conoceré.

I – Introduction

Después agregó animales que inventaba, pegando medio elefante con la mitad de un cocodrilo, sin saber que estaba haciendo con barro lo mismo que su tía Rosa, a quien no conoció, hacía con hilos de bordar en su gigantesco mantel, mientras Clara especulaba que si las locuras se repiten en la familia, debe ser que existe una memoria genética que impide que se pierdan en el olvido.

La Casa de los Espíritus (Isabel Allende)

I.1 Why biophysics ?

The natural sciences are a set of disciplines that try to make sense of the world around us in a way that we humans can understand. Initially motivated by survival, for instance trying to predict weather patterns to develop agriculture, this titanic endeavor probes the smallest scales and fastest times by crashing particle beams into each other, replicating the moments right after the Big Bang [1], and the largest scales and slowest times by analyzing the sounds [2] and the light [3] that reaches the Earth as it wanders through the Universe. Needless to say, in between these two extremes there is ample room to explore and indulge our curiosity.

Living systems sit comfortably at a scale that we can experience with our senses, whether it is large-scale flocks of birds [4], the delicate wing movements allowing the flight of the honeybee [5], or seeing a neutrophil chasing a bacterium through a microscope. [1] Why would a physicist be useful, or interested in working on such problems ? One part of the answer is that, as we will observe later, living systems "need physics" to regulate themselves, and more relevant to this work, multicellular systems "need physics" to develop. This presumes that we can draw the line between what is and what is not "physics", which is rather arbitrary. One could argue that, deep down, everything is physics, and life is nothing but the integration of the standard model Lagrangian. In practice, this is not particularly useful, or insightful in describing the world at the scale of living systems with our current mathematical and computational tools. Rather, we will consider physics as the mesoscopic approaches of fluid mechanics and elasticity, supplemented by the regulatory elements that drive these processes.

1. Classic movie from the 1950s by David Rogers. See https://embryology.med.unsw.edu.au/embryology/index.php/Movie_-_Neutrophil_chasing_bacteria.

The other part of the answer comes by identifying how people pose questions and construct models in the different branches of science, factors which many times stem from tradition. Two of the branches of biology whose areas of interest overlap significantly in this thesis are cell and molecular biology. Their approach is methodic and detailed, carefully probing the interplay between different chemical species involved in intricate metabolic pathways. The physics approach is reductionist, trying to find the minimal amount of ingredients necessary to describe a phenomenon, and searching for "universal" laws that hold in a wide range of situations, such that many problems can be reduced to a form that can be understood in the light of an analogous simpler situation. The fascination of a physicist comes from the realization that many phenomena at different scales can behave in a similar way, even if their fundamental interactions have a completely different origin. Such a "sloppy" approach can be the object of ridicule, such as the plethora of jokes about spherical cows moving in the absence of friction. However, in doing so, we can make general statements about a particular process, decomposing it into important and negligible contributions. If our frictionless spherical cow does a good enough job at reproducing what we observe, and even predicting further results, then it is likely the shape and friction are not particularly relevant to the phenomenon in question. As with any natural science, the ultimate test to challenge our intuition, and our sense of a "good enough job", is experimentation [6].

In broad terms, we will define biophysics as the use of modeling approaches and techniques that are standard in physics to characterize and study biological phenomena.

Living systems have many characteristics that are amenable to such a treatment, emerging from their multiscale nature, exemplified in Fig. I.1. At the molecular scale, the genetic material of cells is encoded into a polymer chain, DNA, that can be replicated and translated depending on the occupancy of different binding sites, such that genes can be expressed under specific circumstances [7]-[10]. At a larger, coarse-grained mesoscale, the interactions between different molecules give rise to controllable proliferation and actomyosin deformations, giving structure, functionality, and motility to different cells and tissues [11], [12]. Finally, at an organism scale, the integration of different environmental stimuli by living systems allows them to adopt different behaviors and strategies to find resources and mates [13]-[15].

Hence many questions arise. How did this complexity evolve in the primordial stages of our planet ? How do living systems find ways to solve problems and survive in their environments ? What constraints does physics impose on living systems ? Furthermore, we cannot but marvel at the wide plethora of living beings that have evolved on our planet, displaying spectacular colors and shapes [16], [17], and adapting to different biomes. On a personal note, I believe that beyond the limited understanding of the inner workings of living systems that we may acquire in the span of our human activities, their astounding diversity holds value in itself. Unfortunately, the fate of our ecosystems has been left at the mercy of "bigger" interests that are terraforming our planet at a rate far exceeding the adaptation time of many species [18]. These questions and challenges are far too many to treat in depth in a single work, however, they must be stressed as a motivation for our scientific endeavor. This thesis will tackle the challenge of development in multicellular organisms under a mesoscopic, physics-driven perspective.

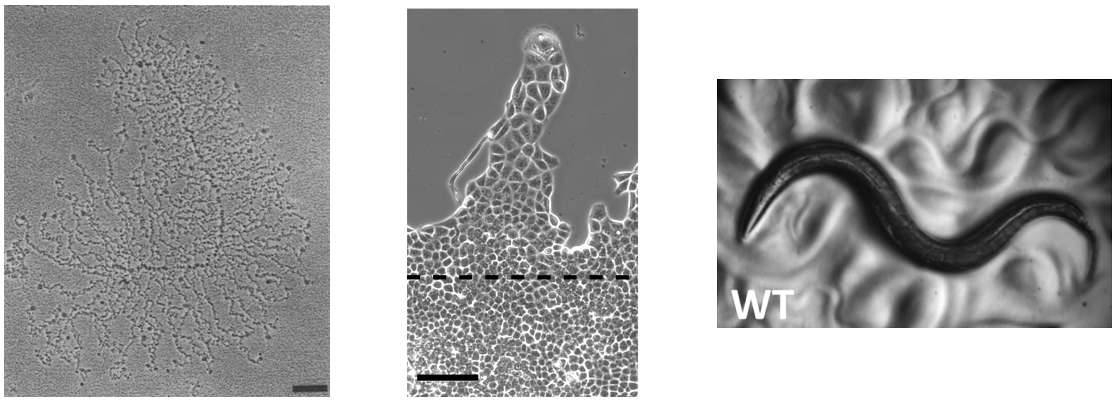

FIG. I.1 ***Living systems at multiple scales.*** *Left : Electron micrograph image of DNA during transcription in the Xenopus embryo. Branches represent the nascent transcripts, and the RNA polymerases are shown at the base of the branches. Scale bar :* 0.2 µm. *Adapted from [19]. Center : Migrating Madin-Darby canine kidney (MDCK) epithelial cells in an in-silico experiment emulating wound healing. The dashed line represents the edge of the cell collective at the start of the experiment, end configuration after* 22 h *shows displacement and fingering. Scale bar :* 100 µm. *Right : The worm Caenorhabditis elegans displaying one of its many postures, each associated to different behaviors. Typical length corresponds to* 1 mm. *Adapted from [20].*

I.2 Development

All multicellular organisms emerge from the proliferation of a single cell or nucleus. A fascinating problem as a consequence of this is how to transition from a completely symmetric state of one cell to an organism comprising different organs, folds, and highly specialized tissues in specific locations. In addition to form and function emerging from this state, such a process must be robust against intrinsic and extrinsic perturbations.

Many natural phenomena exhibit pattern formation, meaning that even if the initial conditions in space are completely homogeneous, the interaction between different constituents of the system will lead to an instability that will grow over time and produce spatial features. These range from completely physical phenomena, such as the formation of convective cells in boiling pots [21] or active stars [22], to biochemical mechanisms resulting in the patterning of feathers in penguins [23]. A big breakthrough in the mathematical modeling of pattern formation in biochemical systems came from the work of Alan Turing. The so-called Turing mechanism characterizes how reaction-diffusion systems of as little as 2 chemical species allow for patterns to emerge [24]. All of this is to say that chemistry can find a way to generate patterns. However, that is only half of the picture, as these patterns must materialize as morphological changes or material transport.

At the mesoscopic scale spanning cells and tissues, mechanics comes to life. As cells duplicate their genome and grow, they continually exchange material with their environment to regulate their size and the forces acting on them [25]. And when cells aggregate, they can present fluid-like [26] and elastic-like [27], [28] behaviors for different timescales and confining

geometries. As a result, a typical framework to study development considers the interplay between mechanics and biochemistry.

Much work has been devoted to understanding how biochemistry influences mechanics. For instance, the localization of certain chemical species can drive the activity of actin filaments [29]. Furthermore, concentration gradients of chemoattractants drive the remodeling of fungal networks [30], and tune the activity of molecular motors in chemotactic bacteria to produce a bias in their translational direction [31].

The converse feedback must not be forgotten, as the deformation of tissues and the flow of fluids will mediate the transport of different chemical species, and the production of forces can trigger changes in gene expression through mechanotransduction [32]. When the molecular species that are being transported or activated/repressed by the mechanical forces are involved in regulating such forces, we have the perfect setting for mechanochemical pattern formation [33], [34].

Space is not the only coordinate where patterning is important, because biological processes, and development in particular, consist of sequences of events : how are "time patterns" achieved ? And, how relevant are they to life ? The building block of living systems, cells, are constantly cycling through different phases of the cell cycle to grow, transcribe new mRNA, and duplicate [37]. And at the organism scale, the development of the body axis in vertebrates depends on rhythmic oscillations that give rise to disjointed segments, with different organisms having a characteristic oscillation frequency [38]. These oscillatory processes require a stable limit cycle to exist in the phase space of relevant variables, and the key to achieving them is having a dynamical system with suitable nonlinear interactions. The Van der Pol oscillator is a prime, simple example that can be realized by electrical circuits [39]. Another example is the Brusselator, a system of three chemical species which reaches a limit cycle at steady state [40]. More generally, Belousov–Zhabotinsky reactions are a whole class of biochemical clocks that produce spatio-temporal patterns [41]. Even extremely simple mathematical abstractions, so-called "cellular automata", have been shown to produce nontrivial spacetime patterns emerging from a small set of rules that determine the evolution of a given density field [42]. With all of this in mind, we may wonder, how are developmental processes coordinated at the scale of the developing embryo ? This will be explored in a posterior section of this work.

One last remark that we would like to mention before delving into the specifics of development in different organisms is that the same interplay between mechanics and chemistry that drives flows, waves, and decision-making in development is involved in the growth and spreading of cancer [43] and regeneration [44], [45]. Hence, the theoretical framework of development could shed light on various areas of interest in relation to living systems.

Different developmental plans can be found in nature, and each one of them showcases different ways in which physics interacts with biochemistry to transition between different stages. Some notable examples come from established model systems in biology. For example, the early embryo of the quail is a disk-shaped structure that rests on top of the egg yolk. Symmetry breaking and cell migration driven by actomyosin tension deform a region of the tissue that lies at the boundary between the embryo and the extra-embryonic medium. The flows, shaped like counter-rotating vortices, lead the boundary region to form a dense structure

in the mid-embryo called the primitive streak, which sets the stage for differentiation later on [35], [46], [47] (see Fig. I.2 top). Another example comes from zebrafish embryos. Their early structure is roughly spherical, separated between the blastoderm, a mass of dividing cells, and the yolk cell. The structure undergoes a process called epiboly or doming, where the top blastoderm layer spreads and migrates covering the yolk, precluding the formation of the ectoderm and future differentiation. The driving force behind this process has been linked to controllable changes in tissue rigidity [36], [48], [49] (see Fig. I.2 bottom).

This work will focus on the early, i.e. pre-gastrulation development of another model system in biology, *Drosophila Melanogaster*, a species of fruit fly.

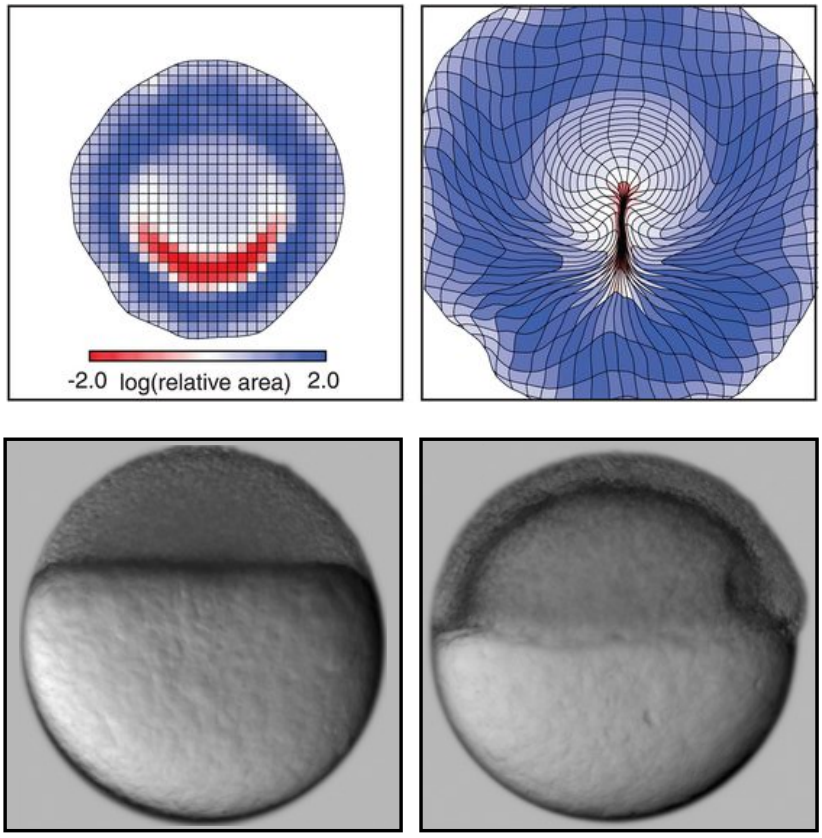

Fig. I.2 ***Physical mechanisms drive development.*** *Top : PIV reconstruction of the early quail embryo before and after the formation of the primitive streak due to actomyosin-driven cell migration. Colors indicate the relative area of different regions : extraembryonic region in blue and primitive streak in red. Adapted from [35]. Bottom : Images of the early zebrafish embryo showing the blastoderm, a mass of cells, sitting on top of the yolk cell. Proliferation of the blastoderm cells leads to a thinning and spreading of this external layer over the yolk cell. Adapted from [36].*

FIG. I.3 ***The star of the show.*** *Adult female Drosophila Melanogaster specimen. Typical size : 3mm. Retrieved from* https://bugguide.net/node/view/901568.

I.3 Enter *Drosophila*

Drosophila melanogaster (see Fig. I.3) has been utilized in genetic and developmental studies for more than a century. Experimentally, it is a practical system to work with. They are readily available to catch, have an approximate time from fertilization to hatching of 10 days at room temperature, and females can lay around 24 eggs per day, depending on the available substrate [50], [51]. Decades of research on this model organism have produced an astonishing number of mutant lines that are well-kept by different research institutes. As an example of the impact that research on the fruit fly had during the 20th century, the 1995 Nobel Prize in Physiology or Medicine was awarded to Edward Lewis, Christiane Nüsslein-Volhard, and Eric Wieschaus for their experimental work on the genes that regulate the development of *Drosophila*. Understandably, the whole process from egg to adult larva is beyond the scope of a single work. We will focus on one small fraction of development that has had relatively less attention in comparison to other studies, which is the pre-gastrulation embryo (see [52] for a detailed review).

After fertilization, the embryo of *Drosophila* goes through several rounds of nuclear division. Nuclear cycles 4 to 7 occur concomitantly with cytoplasmic flows that spread the nuclei along the anterior-posterior axis of the egg [53], [54]. Then, after cycle 8 the flows stop, and most of the nuclei migrate to the cortex of the embryo [55]. The nuclei will continue dividing at the cortex, and during cell cycle 14 the nuclei will develop cellular membranes, forming an epithelial tissue. Before cellularization, the nuclei share a common cytoplasm, hence the early egg is a syncytium. This process is summarized in Fig. I.4.

It must be stressed that the initial cycles are extremely fast compared to regular cellular cycles, clocking in about 8 minutes each [55], [56]. Speculatively, it is evolutionarily advantageous to be fast to avoid being eaten by predators [52]. The way in which the fly reaches these fast nuclear cycles is by skipping the G phases entirely and alternating between the S and M phases. Consequently, there is little to no DNA transcription in these early cycles, and the embryo depends on maternally provided RNA transcripts and proteins to progress through its developmental plan.

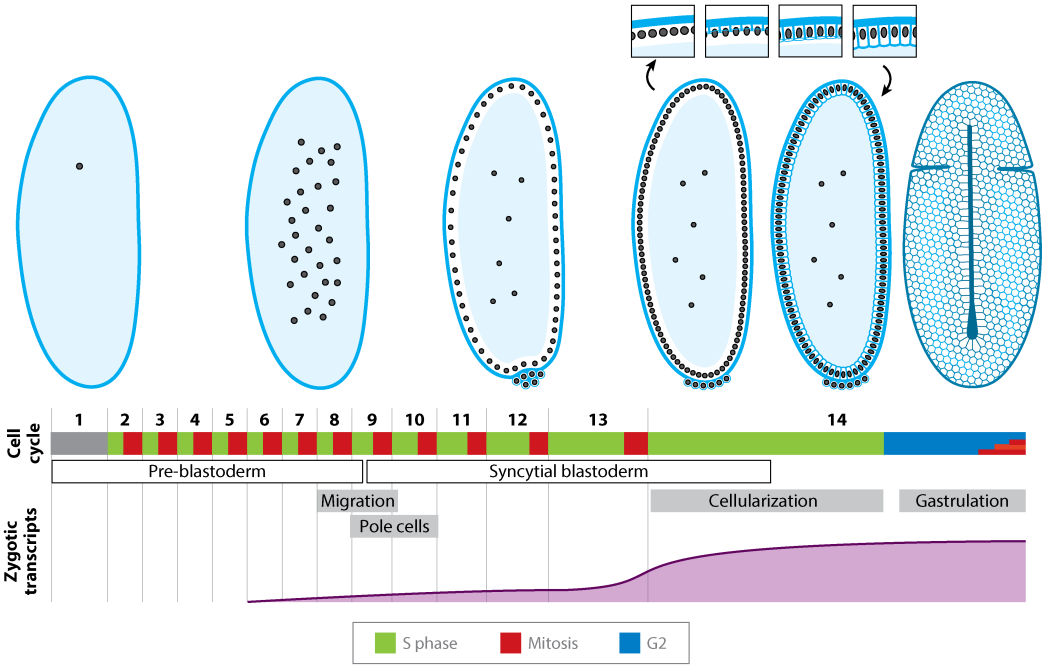

Fig. I.4 *Scheme showing the early stages of development of Drosophila Melanogaster from fertilization to the beginning of gastrulation. Scheme displays changes in the nuclear distributions, cell cycle duration, and transcriptional activity in the egg. Adapted from [52].*

Drosophila has evolved an elegant solution to the problem of symmetry breaking and differentiation. For the cells to differentiate adequately, they activate specific transcriptional pathways depending on the concentration of particular "map" proteins, so-called morphogens, at their location [8]. The space-time concentration of these morphogens as development goes forward is the result of the initial deposition of maternal mRNA in different positions of the embryo [57]. Modifying this morphogen map yields amazing, yet predictable results, such as producing an embryo with two tails when the maternal gene that determines anterior-posterior polarity, bicoid, is lacking [58]. From this, it is clear that to produce a viable embryo, the positions of the cells matter, hence gastrulation must put cells in the right places.

In order for cellularization and gastrulation to happen, new biochemical pathways must activate. This requires that nuclei start transcribing their DNA [59], [60], and hence, slowing down the cell cycle is a must [61]. Experiments have shown that the slowdown is controlled by the ratio of DNA content to cytoplasm, with the wild-type concentration at cycle 14 defining the so-called midblastula transition (MBT) [62]-[64]. As an example of how such a regulatory process could lead to a non-uniform slowdown, the *shkl* mutant has reduced cytoplasmic flows in the initial nuclear cycles, and hence reduced nuclear spreading. As a result, the nuclear density is non-uniform and the embryos present compromised synchrony at the MBT [65], leading to lethality when going beyond a certain asynchrony threshold.

The bottom line is that the nuclei must be in the correct positions, even before gastrulation, for development to progress adequately. Having illustrated the importance of these processes, this thesis will be concerned more particularly with this nuclear positioning and

the synchrony of the pre-gastrulating mitotic divisions in the early embryo of *Drosophila*.

I.4 Structure of this thesis

Chapter I introduced the big picture of biophysics as a way of approaching living systems with the mesoscopic tools and the eyes of a physicist. We described the development of multicellular organisms under this light by highlighting the importance of symmetry breaking and pattern formation in space and time. Then, we briefly mentioned some key physics-driven developmental processes in quail and zebrafish embryos. Finally, we briefly summarized the early development of *Drosophila Melanogaster* to contextualize the research questions and results presented in later chapters.

Chapter II will study the nuclear positioning during cycles 1-7, i.e. from fertilization until the nuclei achieve a uniform distribution in the bulk of the embryo. We will present previous experimental results that argue for the production of actomyosin contractions induced by the cell cycle biochemistry, in particular the activation of the phosphatase PP1 in regions surrounding the nuclei, which in turn drive cytoplasmic flows. We built up a mathematical two-fluid (Cytosol + actomyosin contractile gel) model including all the necessary regulatory chemical species and the nuclei. Our model reproduces experimental results on the large and small-scale structure of the flows, the positioning of the nuclei, and non-trivial myosin transport. We made novel predictions on the transport of morphogen proteins by the flows, and the perturbations to the flow geometry and strength when the embryo geometry is altered. These predictions were successfully verified by experimental observations. We also suggest future experiments that could probe the predicted micron-thin boundary layer close to the cortex where the active fluid entrains the cytosol.

Chapter III considers a simplified mathematical model of the flows by separating them into a gel layer close to the cortex and a cytosol in the bulk. By stripping the regulatory biochemistry to its simplest elements, we were able to analytically study an actomyosin instability driven by its chemical reaction-advection diffusion system, resulting in pattern formation in the gel layer, and the production of sol flows in the bulk. Next, we studied the production of flows in different geometries by the nuclei-activated PP1 concentrations. Finally, we were able to obtain relevant timescales of centering in a circular geometry, and to give an intuition to situations with multiple nuclei in various geometries. These results can help better understand how life uses cytoplasmic flows, and help in designing novel, smart materials.

Chapter IV jumps to the stage where the nuclei have migrated to the cortex of the egg due to microtubule-mediated interactions. During cycles 11-13, the S phase slows down in preparation for arrest at cycle 14. We will discuss how synchrony is relevant, especially given the size of the embryo and the typical diffusion time of molecules in light of how fast divisions must happen. We will present experimental data that show that nuclear density, the DNA content in the nuclei, and temperature are all factors that affect this synchrony. We will build a mathematical model that brings together previous modeling work and experimental observations to reproduce observations on the duration and synchrony of the pre-gastrulating cell cycles, making novel predictions that open up opportunities for future experimentation.

II – Cytoplasmic flows and nuclear positioning

On sait qu'au moment du flux, les eaux resserrées entre les îles Feroë et Loffoden sont précipitées avec une irrésistible violence. Elles forment un tourbillon dont aucun navire n'a jamais pu sortir. De tous les points de l'horizon accourent des lames monstrueuses. Elles forment ce gouffre justement appelé le « Nombril de l'Océan », dont la puissance d'attraction s'étend jusqu'à une distance de quinze kilomètres. Là sont aspirés non seulement les navires, mais les baleines, mais aussi les ours blancs des régions boréales.

Vingt mille lieues sous les mers (Jules Verne)

(This chapter and corresponding appendix are adapted from the publication "Two-fluid dynamics and micron-thin boundary layers shape cytoplasmic flows in early Drosophila embryos" [66], by Claudio Hernández-López, Alberto Puliafito, Yitong Xu, Ziqi Lu, Stefano di Talia, and Massimo Vergassola)

II.1 Motivation & Established facts

II.1.1 Cytoplasmic flows in living systems and *Drosophila*

Cytoplasmic flows are ubiquitous in biology, ranging from flows in large *Physarum* cells [67]-[69] to flows in the extracellular space controlling left-right asymmetry in development [70], [71]. Oogenesis and embryogenesis are two biological processes where flows play key roles [72], [73]. Flows are central in both *C. elegans* and *Drosophila* for the specification of oocytes [74]-[79] and play a crucial role in nuclear and spindle positioning in oocyte mouse meiosis [80], [81]. In most species, cytoplasmic flows are observed in the early stage of embryogenesis [53], [82]-[84]. While the functional role of these flows is not fully understood, we have recently demonstrated that flows drive proper nuclear positioning in early *Drosophila* [54]. The early fly embryo develops as a syncytium, i.e., a multinucleated cell where molecules are free to diffuse. The embryo is large (about $500\mu m$ in length) and thus nuclei following fertilization have to migrate distances as large as $200 - 300\mu m$ to fill the entire embryo [53], [54], [85] (see Fig. II.1). Nuclear movements must be fast, as development proceeds very

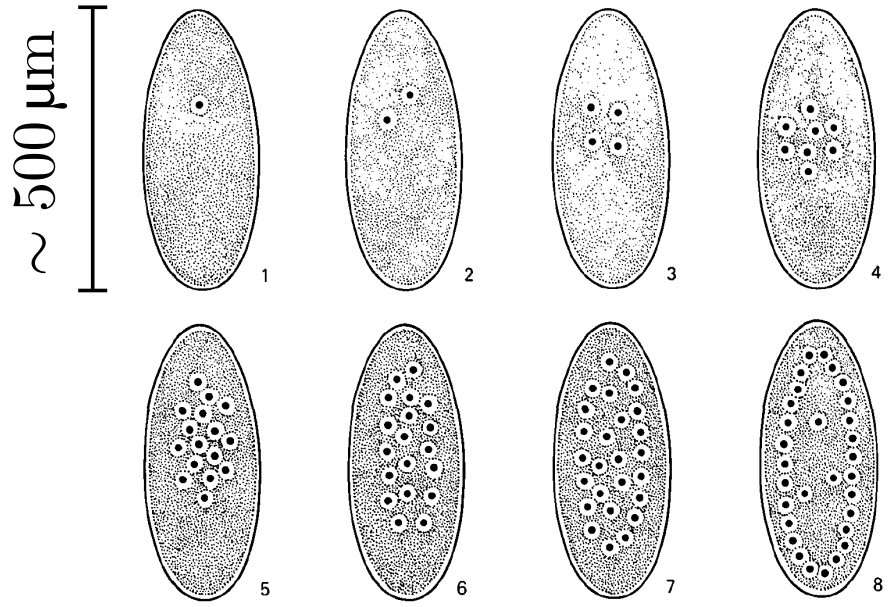

FIG. II.1 ***Nuclear positioning in the embryo of Drosophila after fertilization.*** *Adapted from [55].*

rapidly to avoid predation and pathogens' infection [86]. Upon fertilization, nuclei undergo fast and synchronous cycles of cleavage divisions, lasting about 8 minutes each [56], [87]. We have previously shown that during those divisions, flows transport nuclei along the anterior-posterior (AP) axis ensuring that they occupy the entire embryo uniformly [54].

Cytoplasmic flows in early *Drosophila* arise from the coupling between cell cycle oscillations and actomyosin contractility [53], [54], [85]. At mitotic exit, the activity of Cdk1, a master regulator of the cell cycle, begins to decrease near the chromosomes [88]-[90]. This local down-regulation triggers the activation of the mitotic phosphatase PP1 (and likely PP2A as well) which, together with downregulation of Cdk1, can effectively dephosphorylate mitotic targets in a region of $\sim 50\mu m$ around the nuclei [54]. This size is sufficient to trigger dephosphorylation of mitotic targets near the cortex. Thus, PP1 activity effectively couples nuclear and cortical dynamics. Higher PP1 activity at mitotic exit triggers the differential activation of actomyosin contractility at the cortex. Thus, nuclei can drive the spatiotemporal pattern of cortical actomyosin contractility through the regulation of the cell cycle oscillator. Notably, when cortical actomyosin contractility is blocked via optogenetic perturbations, flows are abolished and nuclei do not spread properly [54] . As a result of this reduced nuclear movement, nuclear density across the embryos is highly non-uniform. In turn, this results in asynchronous cell cycles prior to the maternal-to-zygotic transition (MZT), which demonstrates the functional role of the flows [54], [65], [91].

Our previous experimental results strongly argue that cytoplasmic flows observed in early embryos are driven by cortical contractility [54] (see Fig. II.2). Yet, we are still lacking a quantitative picture of how cortical contractions drive the flow of cytoplasm across the embryo and its consequences. Previous models have described the cytoplasm as a viscous

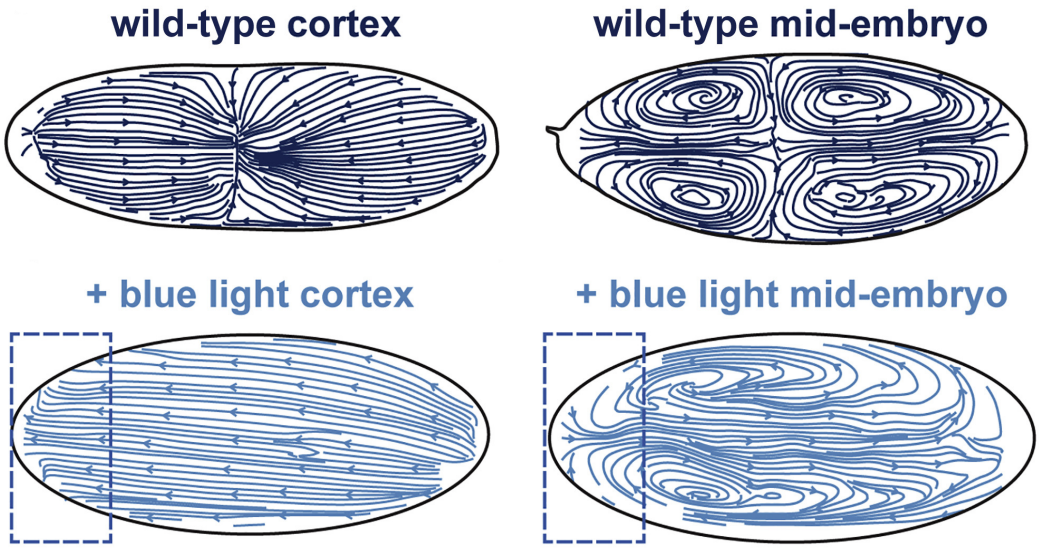

Fig. II.2 ***Actomyosin contractions determine flow geometry.*** *Cytoplasmic flows measured at the cortex of the embryo and at a mid-plane. Top : Wild type flow profiles. Bottom : Altered flow profiles due to the recruitment of myosin-II motors in the anterior side using an optogenetic tool. Adapted from [54].*

fluid with cortical flows imposed as boundary conditions [54], [82], [92]. This model presents severe limitations, both fundamental and practical. First, the model ignores interactions of the actomyosin network at the cortex and the cytosol. In particular, the cytosol should obey the usual no-slip boundary conditions of normal fluids, which is not the case in the above model. Moreover, our analysis of the cytoplasmic vorticity field shows that its small-scale structure in early *Drosophila* embryos deviates from the behavior of a simple viscous fluid. Specifically, vorticity of a Stokes' flow is a harmonic function and should then have maxima and minima only at the boundary whilst they are experimentally observed in the interior of the embryo [54].

A more advanced framework for cytoplasmic flow is offered by multiphase models with multiple fluids [93]. However, these models can become very cumbersome with a large number of mathematical terms and couplings. A simpler approach is offered by models inspired by poroelasticity, which were shown to capture the dynamics of blebbing and response to microindentation [94]-[96]. Here, we present a two-fluid physical model for cytoplasmic flows in *Drosophila* embryos, namely, we consider the interactions between a gel, the contractile actomyosin network, and a passive viscous fluid, the cytosol. We will validate this model by showing that it can capture the basic properties of cytoplasmic flows and then develop its predictions and functional consequences. Our description will start by giving a brief modeling introduction to fluids at low Reynolds numbers and to the behavior of actomyosin networks.

II.1.2 Physics of fluids in living systems

Newton's famous equation $\boldsymbol{F} = \frac{\mathrm{d}\boldsymbol{p}}{\mathrm{d}t}$ relates the rate of change of the momentum of an object to the external forces that act on it. In an analogous way, the Navier-Stokes equation relates the rate of change of the momentum density in a fluid as it flows to the different forces that act on it. This equation is supplemented by the continuity equation associated with the fluid density. They can be written in the following form :

$$\rho \frac{\mathrm{D}\boldsymbol{v}}{\mathrm{D}t} = \nabla \cdot \underline{\underline{\sigma}} + \boldsymbol{f} \ , \tag{II.1}$$

$$\frac{\partial \rho}{\partial t} + \nabla \cdot (\rho \boldsymbol{v}) = 0 \ , \tag{II.2}$$

where D represents the material derivative that accounts for the motion of the fluid parcel in study :

$$\frac{\mathrm{D}}{\mathrm{D}t} = \frac{\partial}{\partial t} + \boldsymbol{v} \cdot \nabla \ , \tag{II.3}$$

and $\boldsymbol{f}$ are volume forces acting on the fluid.

The stress tensor $\underline{\underline{\sigma}}$ contains, in a nutshell, the information of the response of the system to the flow by characterizing the forces that adjacent fluid parcels exert on each other. A constitutive equation is a mesoscopic description of this response, arising from the integration of the molecular interactions between the components of the fluid. The simplest constitutive equation that we can write considers the friction forces between adjacent parcels that are flowing at different speeds, such that it must be an expansion of spatial derivatives of the fluid velocity.

A Newtonian fluid has a stress tensor consisting of three main parts. First, there is an isotropic pressure term that accounts for the kinetics of particles at the molecular scale. Then, there is a bulk viscosity term that describes the resistance of a fluid to volume changes. Finally, there is a shear term that describes the resistance of a fluid to shape changes. A key assumption, that underlies the Newtonian classification, is that the viscosity coefficients do not change as the fluid deforms, otherwise, we would deal with the rheology of non-Newtonian fluids.

With all this, the Navier-Stokes equation for a Newtonian fluid can be written as :

$$\rho \frac{\mathrm{D}\boldsymbol{v}}{\mathrm{D}t} = -\nabla p + \eta_s \Delta \boldsymbol{v} + \left(\frac{1}{3}\eta_s + \eta_b \right) \nabla (\nabla \cdot \boldsymbol{u}) + \boldsymbol{f} \ . \tag{II.4}$$

Now we can perform a dimensional analysis of these equations. Ignoring the influence of external forces :

$$\rho \frac{V}{T} \sim \frac{P}{L} + \eta \frac{V}{L^2} \ , \tag{II.5}$$

where $\eta_s \sim \eta_b \sim \eta$, in a scaling fashion. Also, $T \sim L/V$. The ratio between the viscous and inertial terms is the Reynolds number :

$$\mathrm{Re} = \rho \frac{V^2}{L} \frac{L^2}{\eta V} = \frac{\rho V L}{\eta} \ . \tag{II.6}$$

If $\mathrm{Re} \ll 1$, inertial effects are negligible, in an analogous way to the overdamped limit in mechanical systems, and the left side of Eq. II.4 can be dropped. A very rough estimate, considering the cytoplasm as water, a typical length 500 µm, velocities $1\,\mu\mathrm{m\,s^{-1}}$, density $1000\,\mathrm{kg/m^3}$, and viscosity 1 mPa s yields $\mathrm{Re} \sim 2 \times 10^{-2}$. This means that we can safely discard the inertial terms from the equation.

In essence, at the scale of cells and bacteria, swimming in water is akin to humans trying to swim in a very viscous fluid. More importantly, Stokes' equation is symmetric under time-reversal, which has the profound consequence of preventing net motion from reciprocal motion [97], i.e. the beating of a fin [98] or the swimming of scallops [99].

One possibility of locomotion at low Reynolds numbers is non-reciprocal motion, i.e. deformations that are not symmetric under time reversal. Such is the case of flagellar turning in bacteria [100], or breast-swimming-like motion in *Chlamydomonas* [101].

Another possibility is to spend energy to induce changes in the environment to achieve propulsion. A canonical example is the pathogenic bacterium *Listeria monocytogenes*, which polymerizes an actin comet using the monomers of its host, achieving propulsion opposite to the comet [102], [103]. In a similar spirit, the strategy adopted by the nuclei in the embryo of *Drosophila* is rooted in the behavior of actin networks and their control via molecular motors.

II.1.3 Actomyosin : mechanical properties and activity

Different types of filaments endow structure, motility, and functionality to living systems. Such is the case of actin filaments. They consist of aggregates of G-actin monomer (see Fig. II.3A), that have a typical length and persistence length of around 18 µm. Thanks to the Arp2/3 complex, new branches can polymerize from existing filaments, as shown in Fig. II.3B. In addition to molecular cross-linkers that link monomers in different filaments, this setting allows for the construction of a mesh-like actin network. Such a network exists in the egg of *Drosophila* (see Fig. II.3D).

These networks can be deformed due to the activity of a particular molecular motor called myosin-II, depicted in Fig. II.3B. Molecular motors utilize ATP to drive conformational changes in their structure such that they can bind to different kinds of filaments and walk along them by cycling through these conformations, sketched in Fig. II.3C. Two-headed myosin motors walk in opposite directions in two different filaments, producing relative motion between them (see Fig. II.3E). By externally controlling the binding rate of the motors to actin filaments, it is possible to tune the timing and location of these displacements, which is exactly the strategy adopted by *Drosophila*. From an energetic point of view, instead of spending energy driving molecular motors that actuate cilia or flagella, the nuclei spend energy in activating a particular molecular species, PP1, which increases the binding rate of myosin.

There are two approaches to modeling the behavior of such actomyosin networks. The first one is a molecular approach, simulating the kinetics of actin monomers, the transport of molecular motors, and the resultant forces [107]. This approach is very detailed and very useful to simulate phenomena at short timescales, yet it is computationally intensive. The

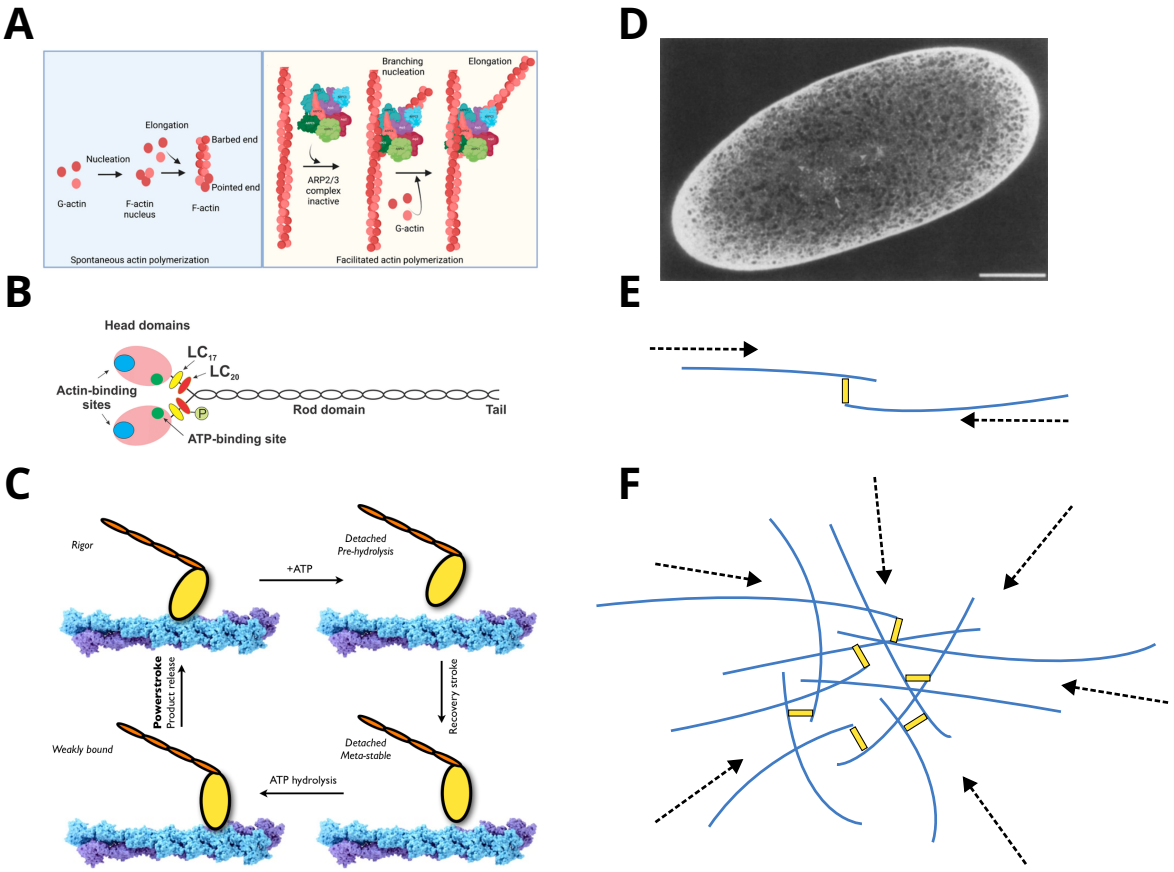

FIG. II.3 ***Structure and behavior of actomyosin networks.*** *A) Scheme showing the aggregation of actin monomers to form actin filaments, and their further branching mediated by the ARP2/3 complex. Adapted from [104].*
B) Scheme depicting the structure of myosin-II. Adapted from [105].
C) Scheme depicting the ATP-driven power cycle that allows myosin-II to walk on the actin filaments. Adapted from [106].
D) Fluorescent image showing the actin network in the embryo of Drosophila Melanogaster. Adapted from [53].
E) Sketch depicting the contractile effect of a myosin-II motor in between two actin filaments.
F) Sketch depicting the bulk contractile effect of an inhomogeneous distribution of myosin-II motors in a quasi-isotropic actin network.

second approach is a mesoscopic description where the network is simulated as a continuous material [108]. In general, the behavior of actomyosin networks can be described as viscoelastic. However, on the timescale of development, i.e. minutes, elasticity can be ignored. Hence, the passive stress tensor of the material contains the contribution of shear and bulk viscosity.

The forces generated by myosin motors will have a clear direction depending on the orientation of the filaments. Naively, if the network is completely isotropic, the contribution from all the different motors would produce forces in every direction, resulting in a net zero force. However, there is an asymmetry between tensile and compressive actions on the filaments due to buckling, such that at the mesoscopic scale, tensile stresses that compress the medium prevail [109], [110], as sketched in Fig. II.3f). In such a case, at the lowest order, we can describe this compressive activity by an isotropic tensor :

$$\sigma^a_{ij} \propto \rho_b \delta_{ij} \ , \tag{II.7}$$

where ρ_b is the concentration of bound myosin. As an effective description of the depletion of sites when too many myosin motors are bound, saturation is incorporated into the stress, in a familiar Hill form :

$$\sigma^a_{ij} \propto \frac{\rho_b}{\rho_b + K_a} \delta_{ij} \ . \tag{II.8}$$

Some further details can be incorporated into the model, like the changes in unbinding kinetics as a function of stress [111]. These details are not relevant to the phenomenology that we are interested in studying.

This actomyosin network (gel) coexists with the cytosol. Consider a space of constant volume V, with $N_s(\boldsymbol{x})$ the number of water molecules and $N_g(\boldsymbol{x})$ the number of actin monomers at a given position in space. Considering each primitive constituent as incompressible, the (constant) volume per water molecule is ν_s, and ν_g per actin monomer. The concentrations $\rho_s = \lim_{\Delta V \to 0} \frac{N_s}{\Delta V}$ and $\rho_g = \lim_{\Delta V \to 0} \frac{N_g}{\Delta V}$ satisfy the following continuity equations :

$$\frac{\partial \rho_s}{\partial t} + \nabla \cdot (\boldsymbol{v} \rho_s) = 0 \ , \tag{II.9}$$

$$\frac{\partial \rho_g}{\partial t} + \nabla \cdot (\boldsymbol{u} \rho_g) = 0 \ , \tag{II.10}$$

where $\boldsymbol{v}$ is the sol velocity, and $\boldsymbol{u}$ is the gel velocity. Assuming that all the space is occupied, then necessarily, for every infinitesimal volume element, $\Delta V = \nu_s N_s + \nu_g N_g$. In another way :

$$1 = \nu_s \rho_s + \nu_g \rho_g \ . \tag{II.11}$$

We may rename $\nu_g \rho_g = \phi$, and $\nu_s \rho_S = 1 - \phi$, where ϕ is the gel volume fraction. Taking the time derivative and using Eqs. II.9,II.10 :

$$\nabla \cdot (\boldsymbol{v}(1 - \phi) + \boldsymbol{u}\phi) = 0 \ . \tag{II.12}$$

Finally, assuming that $\phi \ll 1$:

$$\nabla \cdot \boldsymbol{v} = 0 \ , \tag{II.13}$$

such that we can assume an incompressible sol and a compressible gel.

II.2 Results

II.2.1 Stokes' flows fail to explain cytoplasmic streaming

To gain insight into the physics of cytoplasmic flows, let us start with the simplest possible option : a single fluid obeying Stokes' equations, which describe a normal fluid dominated by viscous effects. The Navier-Stokes equations for an incompressible fluid reduce then to [112] :

$$\eta \nabla^2 \boldsymbol{v} = \nabla p \,; \qquad \nabla \cdot \boldsymbol{v} = 0 \,, \tag{II.14}$$

where η is the dynamic viscosity, $\boldsymbol{v}$ the velocity field, and p the pressure field. These fields are three-dimensional, but experimental data in [54] considered horizontal and vertical mid-planes going through the AP axis. Given the roughly ellipsoidal geometry of the embryo, the flows in those planes are expected to be approximately two-dimensional with vanishing components in the respective off-plane directions. That was checked in [54] and it is further verified in Appendix Fig. A.1 by comparing the two orthogonal orientations of the mid-planes. In the sequel, we shall therefore simplify our equations by working in a two-dimensional setting. The full three-dimensional geometry is computationally more demanding but is a straightforward generalization of the results presented hereafter.

Three main arguments can be put forward against such a simple description of the cytoplasm. The first two arguments are empirical and data-driven. First, we found that the Stokes' flows that fit a set of measured data are unable to correctly predict the rest of said data. Specifically, we found that, in order to fit the velocities in the bulk of the embryo, the flow speeds near the embryo cortex ($\lesssim 10\mu m$) should significantly exceed the measured flow. That suggests that Stokes' flows cannot capture the behavior of cytoplasmic flows near the embryo boundary. Second, while the large-scale patterns are visually similar, quantitative properties of the experimental flows clearly deviate from Stokes' flows. A convenient way to highlight those effects is the vorticity field $\omega_v = \nabla \times \boldsymbol{v}$ [112]. This quantity measures the local circulation of fluid elements and the presence of a derivative in its definition highlights small-scale properties of the velocity $\boldsymbol{v}$. From Eq. (II.14), we can derive :

$$\eta \nabla^2 \omega_v = 0 \,, \tag{II.15}$$

which implies that the vorticity ω_v is a harmonic function. This is relevant as extrema of harmonic functions must be located at the boundary of the domain, whilst the vorticity of our measured flows systematically features four extrema well inside the embryos [54]. That manifestly demonstrates deviations of cytoplasmic flows from a Stokes' structure.

The third argument on boundary conditions relates to the first point above. A normal fluid obeys no-slip conditions at the boundary, i.e., it should move at the same velocity as the boundary. Since we do not observe the vitelline membrane undergoing significant movement, we can assume that the perivitelline fluid should be at rest at the boundary. In the pre-blastoderm stage, the plasma membrane is in most places adjacent to the vitelline membrane, thus no-slip boundary conditions are a reasonable approximation, which contradicts imposing a non-trivial velocity as boundary condition.

In sum, a single passive Stokes flow is insufficient and a better physical model is needed to capture the dynamics of flows in early *Drosophila* embryos. As we show in the next Section, a parsimonious way out of these limitations is the introduction of two fluids, which will be shown to lead to the formation of a boundary layer near the cortex and differential motion of gel and cytosol.

II.2.2 Two-fluid model for cytoplasmic flows

To establish a more relevant model for cytoplasmic flows, we explicitly consider both the actomyosin network and the cytosol, described as an active gel and a passive viscous fluid, respectively. We describe the interaction between the two fluids with a simple friction term. Moreover, we include the nuclei and their cell cycle regulation to obtain a model that can describe nuclear positioning by the flows. Thus, our formulation has four components : the cytosol, the gel, the nuclei, and the activity of PP1 which couples nuclear and cortical dynamics. These components, their interactions and their spatial localization have been summarized in Fig. II.4. We describe the cross-section under study as an ellipse of major axis $250\mu m$ and of minor axis $90\mu m$. We then obtain the following equations :

$$\Gamma(\boldsymbol{u}-\boldsymbol{v}) - \nabla p + \eta\nabla^2\boldsymbol{v} = 0\,;\; \nabla\cdot\boldsymbol{v} = 0\,;\; \Gamma(\boldsymbol{v}-\boldsymbol{u}) + \nabla\cdot\sigma = 0\,. \tag{II.16}$$

Here, Γ is the gel-sol friction coefficient, $\boldsymbol{v}$ is the sol velocity, $\boldsymbol{u}$ is the gel velocity, p the pressure field, η the shear viscosity of the cytosol and the gel stress tensor σ decomposes as :

$$\sigma_{\alpha\beta} = \sigma^a_{\alpha\beta} + \sigma^d_{\alpha\beta}\,. \tag{II.17}$$

Note that kinetic and friction coefficients may *a priori* depend on the location via the gel concentration : here, we make the simplest choice of assuming them constant.

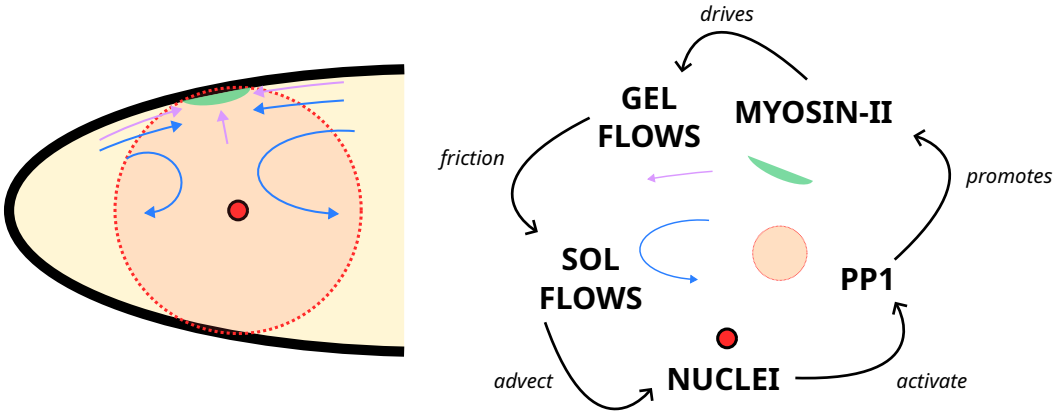

FIG. II.4 **A scheme of the mechano-chemical coupling underlying our model for cytoplasmic flows** *Left : Sketch depicting a slice of the anterior side of the egg, along with the ingredients of our model and their location in space. Right : captions and interaction sequence detailing the mechano-chemical coupling that results in nuclei being transported in the embryo.*

The passive component reads

$$\sigma^d_{\alpha\beta} = \eta_b \left(\nabla \cdot \boldsymbol{u}\right) \delta_{\alpha\beta} + \eta_s \left(\frac{\partial u_\alpha}{\partial r_\beta} + \frac{\partial u_\beta}{\partial r_\alpha} - \left(\nabla \cdot \boldsymbol{u}\right) \delta_{\alpha\beta} \right) \tag{II.18}$$

where η_b and η_s are the gel bulk and shear viscosity. The active term models contractions of the actomyosin network driven by gradients in bound myosin concentration, as illustrated in Fig. II.4. The simplest option for the stress tensor is an isotropic term with saturation :

$$\sigma^a_{\alpha\beta} = \zeta \frac{\rho_b}{\rho_b + K_a} \delta_{\alpha\beta} \,, \tag{II.19}$$

where ρ_b is the concentration of active myosin (myosin bound to actin) [113]. ζ is the contraction strength and K_a is the active saturation parameter (see the below section on vorticity for the rationale and tests of this choice).

The cytosol satisfies no-slip boundary conditions $\mathbf{v}|_{\partial\Omega} = 0$ at the boundary of the domain (cortex) $\partial\Omega$. Conversely, the active gel must satisfy the no-penetration condition $\left(\mathbf{u} \cdot \mathbf{n}\right)|_{\partial\Omega} = 0$, where $\mathbf{n}$ is the normal to the cortex, but can slide along it. The balance of the forces between the cortex and the gel layer in contact with it yields the tangential traction boundary condition $\left(\sigma^T \mathbf{n} \cdot \mathbf{t}\right)|_{\partial\Omega} = \Xi$, where $\mathbf{t}$ is the local tangent vector to the cortex. If the gel were free to slip, then $\Xi = 0$, which is contradicted by the experimental observation of a (weak) backflow following antero-posterior expansions. This observation makes it more appropriate to consider the elastic response discussed hereafter.

As the gel flows, actomyosin filaments attach and detach from the cortex. When detached, filaments are carried by the flow $\mathbf{u}$. When attached, filaments are getting strained and, if the contracting force vanishes, they will tend to flow back to their anchoring point. To describe the evolution of the straining displacement s, we denote by k_c the binding rate to the cortex and by τ_c the cortical unbinding time. The derivative $\dot{s} = u_t = \mathbf{u} \cdot \mathbf{t}$ if the filament is in the bound state and $\dot{\mathbf{s}} = 0$ in the unbound state. The probability of the former is $\frac{k_c\tau_c}{1+k_c\tau_c}$ and the duration t of the binding event is exponentially distributed as $e^{-t/\tau_c}/\tau_c$. Taking the average to identify typical effects over many filaments, it follows that the average displacement

$$\begin{aligned} \langle s \rangle &= \frac{k_c\tau}{1+k_c\tau_c} \int_0^\infty \frac{e^{-t'/\tau_c}}{\tau_c}\, dt' \int_{t-t'}^{t} u_t(t'')\mathrm{d}t'' \\ &= \frac{k_c\tau_c}{1+k_c\tau_c} \int_0^\infty e^{-t'/\tau_c} u_t(t-t')\ \mathrm{d}t' \,, \end{aligned} \tag{II.20}$$

where the second equality is obtained integrating by parts. Given the displacement, the tangential traction is finally :

$$\Xi = -k_e \langle s \rangle \,, \tag{II.21}$$

where k_e is the spring constant of the elastic restoring force.

II.2.3 Modeling the control of actomyosin contractility by the cell cycle

Biochemical regulation of myosin activity is controlled by the cell cycle oscillator, viz., the spatiotemporal activity of PP1. Experimental observations suggest the following dependence

of PP1 activity on space and time :

$$\rho_p(\mathbf{r},t) = g(t) \sum_{i \in nuclei} e^{-|\mathbf{r}-\mathbf{r}_i|/\lambda}\,, \tag{II.22}$$

where $g(t)$ is a suitable oscillatory function that embodies the phase of the cell cycle (see Fig. A.2), $\mathbf{r}_i$ is the position of the i-th nucleus, $\mathbf{r}$ is the point of interest, and $\lambda \simeq 30\mu m$ is the decay length of the PP1 activity cloud generated by each nucleus, as illustrated in Fig. II.4.

We now present the dynamical equations for myosin II and its regulation by the above PP1 field. We consider myosin II to exist in two states : unbound and bound (active) to actin filaments. The unbound and bound states are described by a reaction-diffusion equation :

$$\frac{\partial \rho_k}{\partial t} + \nabla \cdot J_k = G_k\,, \tag{II.23}$$

where J_k is the flux of species k and G_k is a reaction term. We consider two kind of fluxes : advection and diffusion. The unbound myosin will be advected by the sol, whereas the bound myosin by the gel, so that :

$$\mathbf{J}_b = \mathbf{u}\rho_b - D_b \nabla \rho_b\,; \qquad \mathbf{J}_u = \mathbf{v}\rho_u - D_u \nabla \rho_u\,, \tag{II.24}$$

where D_b and D_u are the respective diffusion constants and myosin diffuses much less when bound, i.e., $D_b \ll D_u$.

As for the reaction terms, the two myosin species are coupled by binding/unbinding kinetics, with the total amount of myosin assumed to be constant. Considering these reactions in a linear regime, one obtains :

$$G_k = \sum_j R_{kj}\rho_j \tag{II.25}$$

where the elements of the matrix R are the reaction rates. Since the total myosin is constant, $R_{jk} = -R_{kj}$. We assume that the myosin unbinds at a constant rate so that $R_{bu} = -R_{ub} = -k_u$. The activation of myosin is promoted by Rho activity, which is in turn regulated by PP1 and cortical mechanisms, as sketched in Fig. II.4. It is observed experimentally that the timing of myosin activation is delayed with respect to that of PP1 and Rho activation [54]. That motivated us to introduce an effective intermediate field ρ that responds to PP1 activity with a characteristic time τ and mediates the activation of myosin according to the equation :

$$\frac{\partial \rho}{\partial t} = -\frac{1}{\tau}\rho + k'\rho_g \frac{\rho_p}{\rho_p + K_p}\,. \tag{II.26}$$

The field ρ_g effectively accounts for the preferential activation of myosin close to the cortex, likely due to the localization of ρ-GEF molecules mediating the Rho/myosin activation process, as well as molecules that help organize the cortical actin network. The field rapidly decays away from the cortex as $\rho_g = e^{-r/\mu}$ (see Fig. II.5), where r indicates the distance from the cortex and μ is the characteristic decay length (the value used in the rest of the paper is $\mu = 8\mu m$). The field ρ controls the rate of myosin activation as :

$$\frac{\partial \rho_b}{\partial t} + \nabla \cdot (\mathbf{u}\rho_b) = D_b \Delta \rho_b - k_u \rho_b + k_b \rho \rho_u\,; \tag{II.27}$$

$$\frac{\partial \rho_u}{\partial t} + \nabla \cdot (\mathbf{v}\rho_u) = D_u \Delta \rho_u + k_u \rho_b - k_b \rho \rho_u\,. \tag{II.28}$$

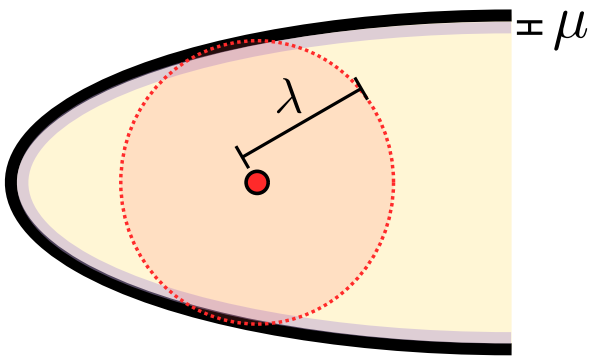

FIG. II.5 ***Localized myosin binding*** *Sketch showing the concentration of Rho-GEF next to the cortex, and the PP1 cloud of a single embryo. Characteristic lengthscales are μ and λ respectively*

II.2.4 Modeling the transport of nuclei, their divisions and positioning

The last step to complete our model is to define the dynamics of nuclei. Nuclei are advected by the local sol velocity $\mathbf{v}$ according to the following overdamped equation for the position $\mathbf{r}_i$ of the i-th nucleus :

$$\dot{\mathbf{r}}_i = \mathbf{v}(\mathbf{r}_i) - \nu \sum_{j \neq i} \left(\partial_{\mathbf{r}_j} V_{ij} \right) \hat{\mathbf{r}}_{ij} \,, \tag{II.29}$$

where ν is the mobility. The interaction potential V_{ij} between nuclei i and j follows an inverse power law with an exponential tail :

$$V_{ij} = \left(\frac{\ell_i + \ell_j}{r_{ij}} \right)^{\alpha} \exp\left(-\frac{r_{ij}}{\ell_i + \ell_j} \right) \,, \tag{II.30}$$

which provides an effective description of the forces acting among nuclei that result from the action of microtubule spindles, asters and/or actin caps [114], [115]. The simple idea is that when the typical extension of those microtubule structures is comparable/longer than the distance r_{ij} between the two nuclei i and j, a repulsive force will result. The length ℓ_i of the microtubule structure radiating from the i-th nucleus depends on the phase of its cell cycle. Specifically, based on the observation that microtubule asters are inhibited by Cdk1 and grow at mitotic exit/early interphase [116], [117], we take the following linear dependence on the local PP1 concentration :

$$\ell_i = \ell_{\min} + \beta \rho_p(\boldsymbol{r_i}) \,. \tag{II.31}$$

Finally, in Eq. II.30 we take the exponent $\alpha = 6$, as in molecular dynamics (other choices leave our results unchanged).

Nuclear divisions are regulated by the temporal function $g(t)$ that controls the PP1 concentration in Eq. II.22. In particular, the minima of this function mark each mitotic entry, at which point every nucleus is replaced by two nuclei separated by a distance of four microns, centered around the original one. As there is no PP1 at the beginning of

division, microtubules have their minimal length, and nuclei are progressively moved apart by the growing filaments. The division axis is chosen randomly for each division event ; tests were also performed using a deterministic rule, namely splitting nuclei along the direction perpendicular to the net force exerted on each nucleus. Our main results and conclusions were found unaltered. As the microtubules grow according to Eq. II.31, the nuclei move apart as a result of the effective potential, thus completing mitosis.

II.2.5 Myosin-driven contractions drive the large-scale geometry of embryonic flows

Our model for cytoplasmic flow is defined by the ensemble of Eqs. (II.16-II.31), along with the chosen parameters (see Appendix Table A.1). Values have been obtained from the literature, e.g., η, from previous experiments, e.g. λ, and through parameter scanning. Among these, some of them have been directly compared to previously reported values, e.g., τ_c, η_s, whereas others have been justified through scale arguments, e.g., Γ, (see Eq. II.33). In particular, we observed that changing Γ for fixed η_s changes the relative strength of the vortices induced by the flows. We chose a value that captures the experimentally measured velocity profiles. Furthermore, a parameter scan around our chosen values showed that no parameter value is critical at a fine-tune level to reproduce the flows qualitatively.

We simulated the model starting with a single nucleus, which undergoes seven cycles of divisions and transport by cytoplasmic flows generated by the above dynamics. Fig. II.6 shows that the model captures experimental observations. In particular, the large-scale structure of the flow and its timing with the cells cycles are correctly reproduced. The large-scale pattern of the flow features four vortices and a stagnation point that arises near the center of the nuclear cloud where cortical flows converge. A strong antero-posterior (AP) extensive flow is observed during interphase, at the peak of myosin activation and contraction (see Figs. II.6A-B). The basic mechanism is as in Ref. [54] : PP1 activity drives cortical myosin gradients, which lead to contractility and motion of the actomyosin gel ; The sol is then entrained by the friction with the gel and its incompressibility produces its ingression in the bulk of the embryo and the four vortices pattern. As for the backflows seen in Figs. II.6C-D, they are generated by the elastic restoring force Eq. II.21. The force pushes back the actomyosin filaments when the action of myosin contractions vanishes as the cell progresses into mitosis. As in the case of the forward flow, the sol is then entrained by friction and creates its own flow. Its structure is similar to the reverse of the forward flow, albeit the amplitude is smaller since the elastic force is weaker than myosin contractility.

Note that the nuclear positions and flows are strongly coupled by the PP1 profiles being centered around the nuclei. In particular, the positions of the stagnation and the ingression points will move together with the center of the nuclear cloud. This is the basis of the self-correcting properties of cytoplasmic flows that will be discussed later below. As for the dependence on the cycles, cortical and cytoplasmic speeds increase gradually in magnitude from cycles 4–6 and then significantly reduce by cycle 7. The reason for the increase is the growing number of nuclei and the strength of their effects. However, by cycle 7, a new effect sets in : nuclei are almost uniformly spread along the AP axis, which implies that gradients of myosin activation tend to fade and eventually vanish. That is the reason for the minor

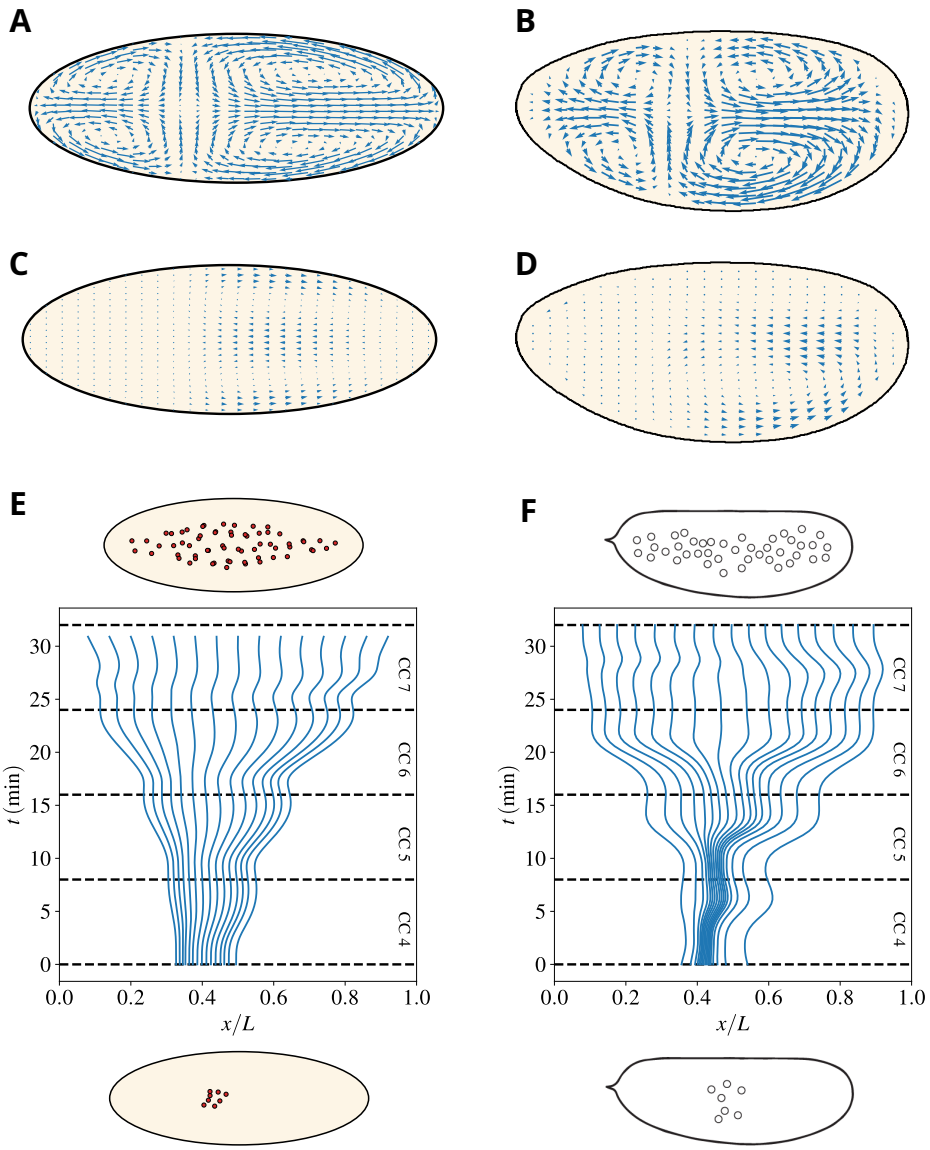

FIG. II.6 **The two-fluid model captures the large-scale feature of embryonic flows.** *A)-B) Typical cytoplasmic flow observed during the AP expansion phase in our model (A) and experiments (B). C)-D) Typical cytoplasmic backflow observed during the AP contraction phase in our model (C) and experiments (D). The length of the arrows is in the same units as in panel (A,B) so as to highlight the reduced speed of backflow. E)-F) Reconstructed initial distributions to achieve a uniform nuclear distribution at the end of cell cycle 7 in our model (E) and wild-type experiments (F). Particles are uniformly distributed along the AP axis at the end of cycle 7 and simulated (E) or measured (F) cytoplasmic flows are used to evolve their position backward in time until the beginning of cycle 4.*

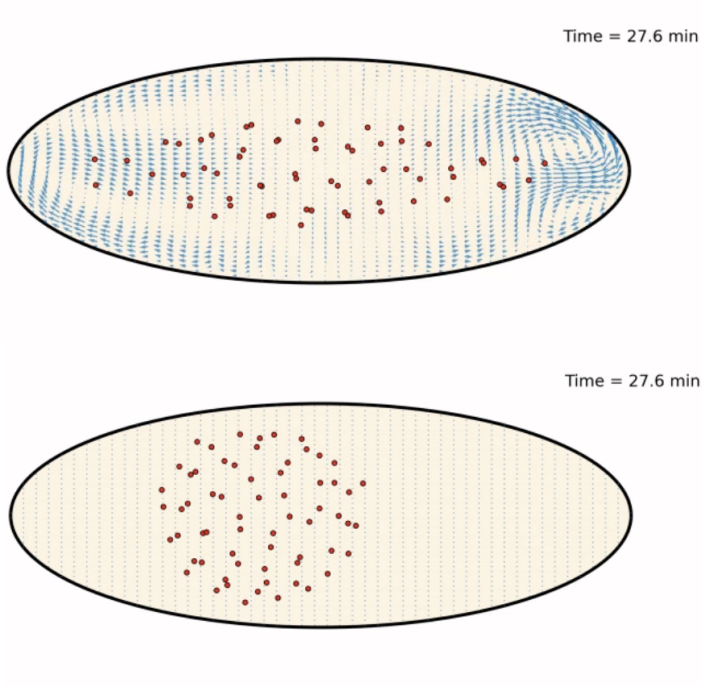

Fig. II.7 *Final nuclear distribution and residual flow profile in the egg with (top) and without (bottom) actomyosin deformations.*

role of cytoplasmic flows in late cycles.

In sum, Eqs.(II.16-II.31) produce effective dynamics to spread uniformly the nuclei over the embryo. A striking way to condense this message is provided by Figs. II.6E-F, which trace back nuclei distributed uniformly at the end of cycle 7. To this aim, we computationally positioned uniformly distributed particles in the mid-embryo along the AP axis at the end of cycle 7. We then used the simulated or experimentally measured cytoplasmic flows to evolve their position backward in time until the beginning of cycle 4. The figure clearly shows that nuclei would start from a small cloud centered in the mid-embryo at the beginning of cycle 4 both in the model and the experiments. We also performed numerical simulations where the coupling between the PP1 activation and myosin-II recruitment is impaired, such that the only forces driving nuclear motion are the microtubule-microtubule interactions. In such a case, as shown in Fig. II.7, spreading is severely compromised and the nuclear distribution remains centered around its initial position.

II.2.6 Sol-gel friction induces extremal points of the vorticity inside the embryo

The experimental vorticity field in Ref. [54] highlighted the fundamental discrepancy between cytoplasmic and Stokes' flow explained in the above Section. Conversely, we show here that our model reproduces the presence of extrema of the vorticity field inside the embryo.

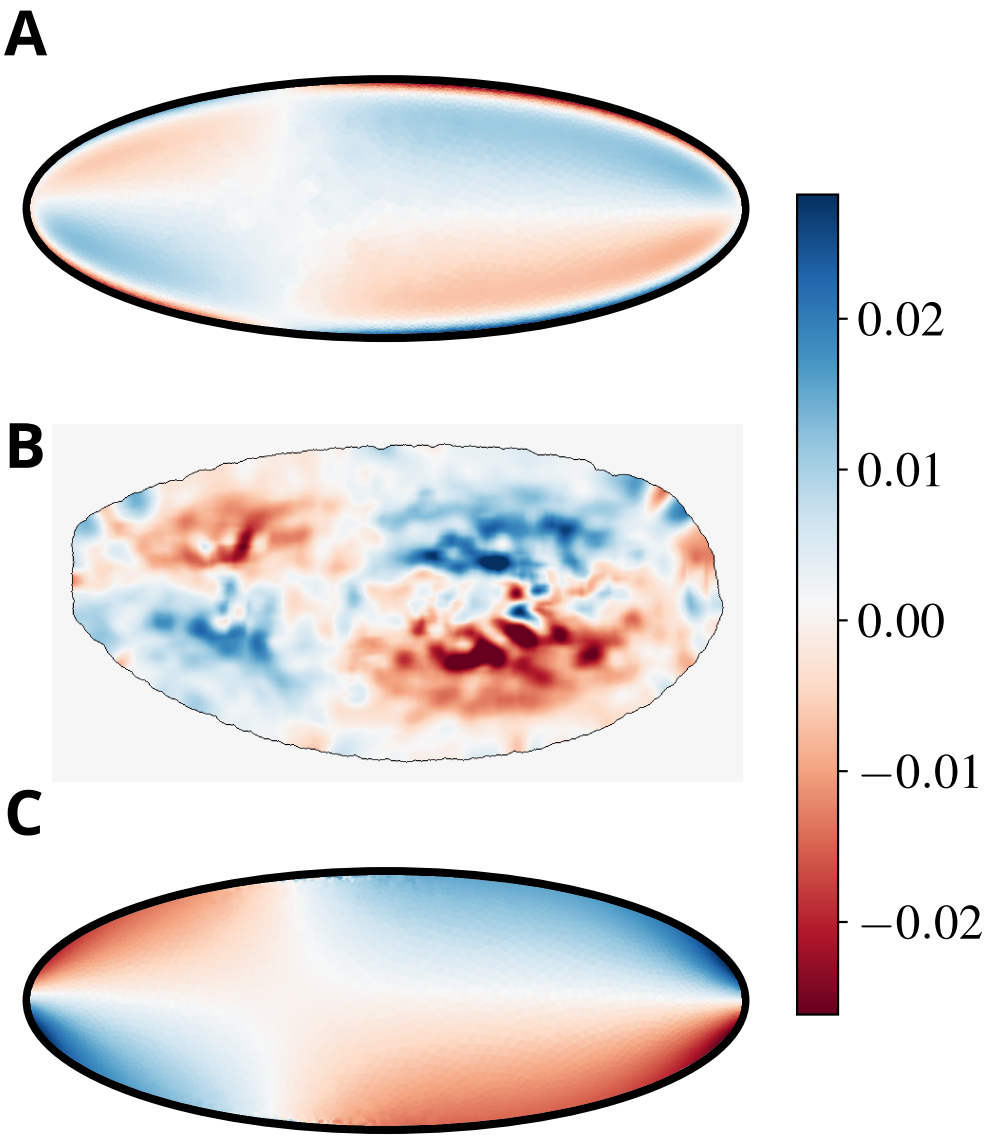

FIG. II.8 **Our model explains experimental observations of the sol vorticity.** *A)-B) A heatmap showing the vorticity field ($\omega_v = \nabla \times \mathbf{v}$) of the sol flow in our model (A) and in experiments (B). C) The total vorticity $\eta_s \omega_u + \eta \omega_v$ (normalized by $\eta + \eta_s$ to preserve its physical dimensions), showing its extrema at the boundary of the domain, which reflects the harmonic nature of the field in our specific model (see discussion in the body of the paper).*

By taking the curl of Eq. II.16, we obtain

$$\eta\nabla^2\omega_v = \Gamma\left(\omega_v - \omega_u\right) ; \qquad \eta_s\nabla^2\omega_u = \Gamma\left(\omega_u - \omega_v\right) . \tag{II.32}$$

Remark indeed that all the terms in the stress tensor that are $\propto \delta$ do not contribute as they yield terms $\propto \epsilon_{ij}\nabla_i\nabla_j$, where the tensor $\epsilon_{12} = -\epsilon_{21} = 1$ is anti-symmetric. It follows from Eq. II.32 that, while the sum of the two vorticities $\eta_s\omega_u + \eta\omega_v$ is still harmonic, each individual component is not. We conclude that extrema are *a priori* possible for the individual components whilst they are not for their weighted sum. This property is explicitly confirmed in Fig. II.8.

Note that while the dissipative part of the gel stress tensor in Eq. II.18 is fixed, the active component (Eq. II.19) could be non-isotropic and therefore take a non-diagonal form, e.g., in the presence of nematic order [108]. This would *a priori* lead to a non-vanishing contribution to the vorticity balance, which would break the harmonicity of the total vorticity $\propto \eta_s\omega_u + \eta\omega_v$. In the absence of data on the gel velocity, we cannot locate the extrema of the total vorticity and test its harmonicity. Furthermore, we show here that the simple isotropic form in Eq. II.19 captures the main phenomenology available at this stage. That was the rationale for such a minimalistic choice (and constant friction and kinetic coefficients), which should of course be tested and possibly revisited as gel flow data become available.

II.2.7 Spatio-temporal distributions of sol and gel flows are qualitatively different, with a sharp micron-thin boundary layer at the cortex

An essential feature of our model is the explicit modeling of two fluids : cytosol and gel. Such a model accommodates of course the possibility of an effective single fluid, i.e., that the friction between the two fluids makes their flow similar to each other. The purpose of this Section is to show that that is not the case, which is evidenced by Fig. II.9, where snapshots of sol and gel flows (at the same time) are compared. The most striking difference is that the sol flows in its circulating four-vortices patterns with major components along the anteroposterior axis whilst the gel mainly flows from the inside of the embryo towards the cortex. The latter drives the accumulation of gel components to the surface that will be quantified in the next Section. As already mentioned, experimental data on gel flow are not available yet and would be crucial to test our predictions.

The difference in the flow patterns of the two fluids should not mislead the conclusion that friction is irrelevant and does not play any role. On the contrary, friction is what drives the flow of the sol, which would be at rest without the entrainment by the gel. Most of the entrainment is provided in the micron-size boundary layer observed in Fig. II.10 close to the cortex, where most of the active myosin accumulates, see Fig. II.11. These observations are consistent with the fact that cytoplasmic flows are mainly driven by cortical rather than bulk actomyosin, as demonstrated by optogenetic experiments in Ref. [54]. The thin, micron-size width of the boundary layer is consistent with the experimental observation that cytoplasmic flows are observed very close to the cortex in spite of the membrane appearing to be essentially immobile and the no-slip boundary condition applying to the sol. The physical explanation and prediction of our model are that a very thin boundary layer exists, where

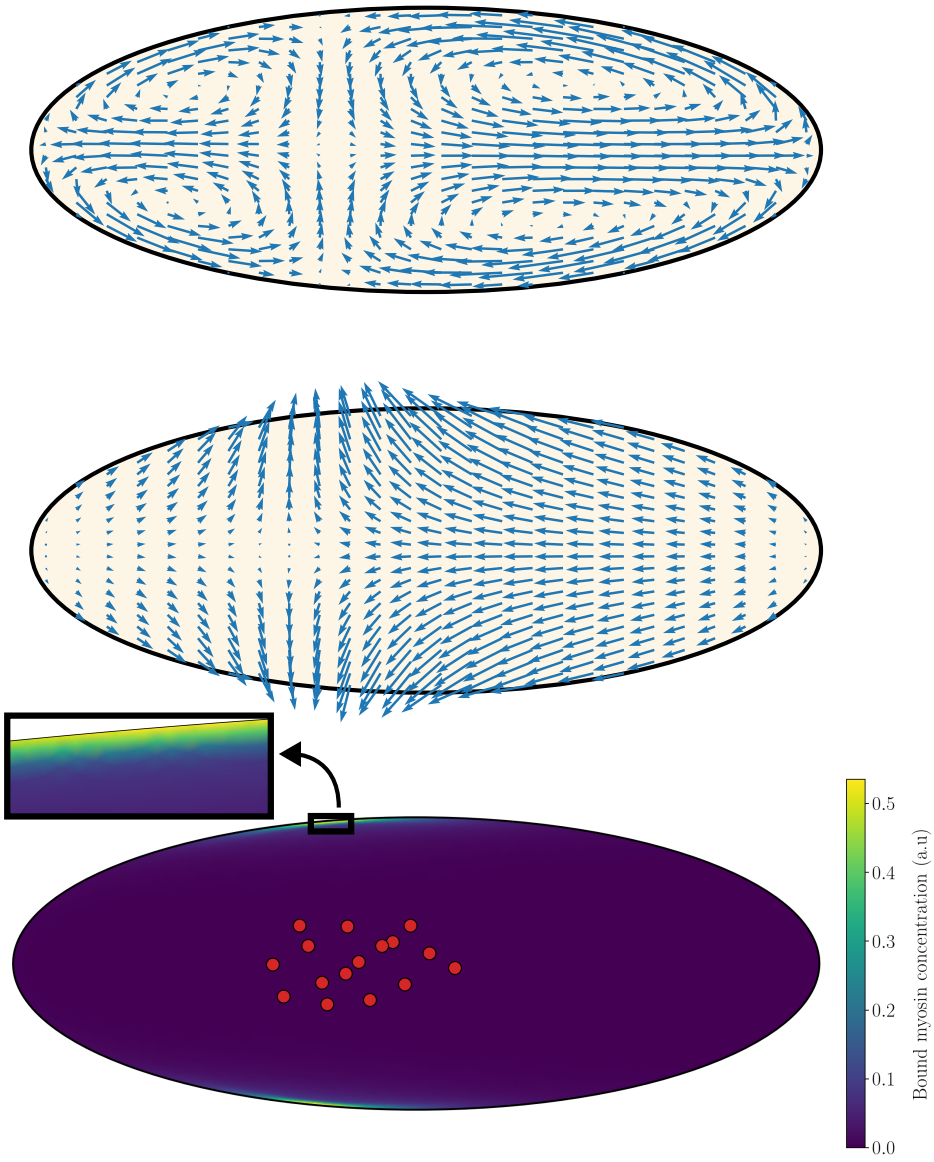

FIG. II.9 **The multiphase nature of the dynamics in our model is germane.** *Typical flow of the sol (Top) and the gel (Center). Note that, contrary to the sol, the gel mainly flows from the inside of the embryo towards the cortex, driving the peaks in myosin concentration in Fig. II.11. The gel velocity component perpendicular to the cortex vanishes when getting closer to it. Heatmap (Bottom) shows the thin cortical region where bound myosin accumulates and where the two fluids are entrained.*

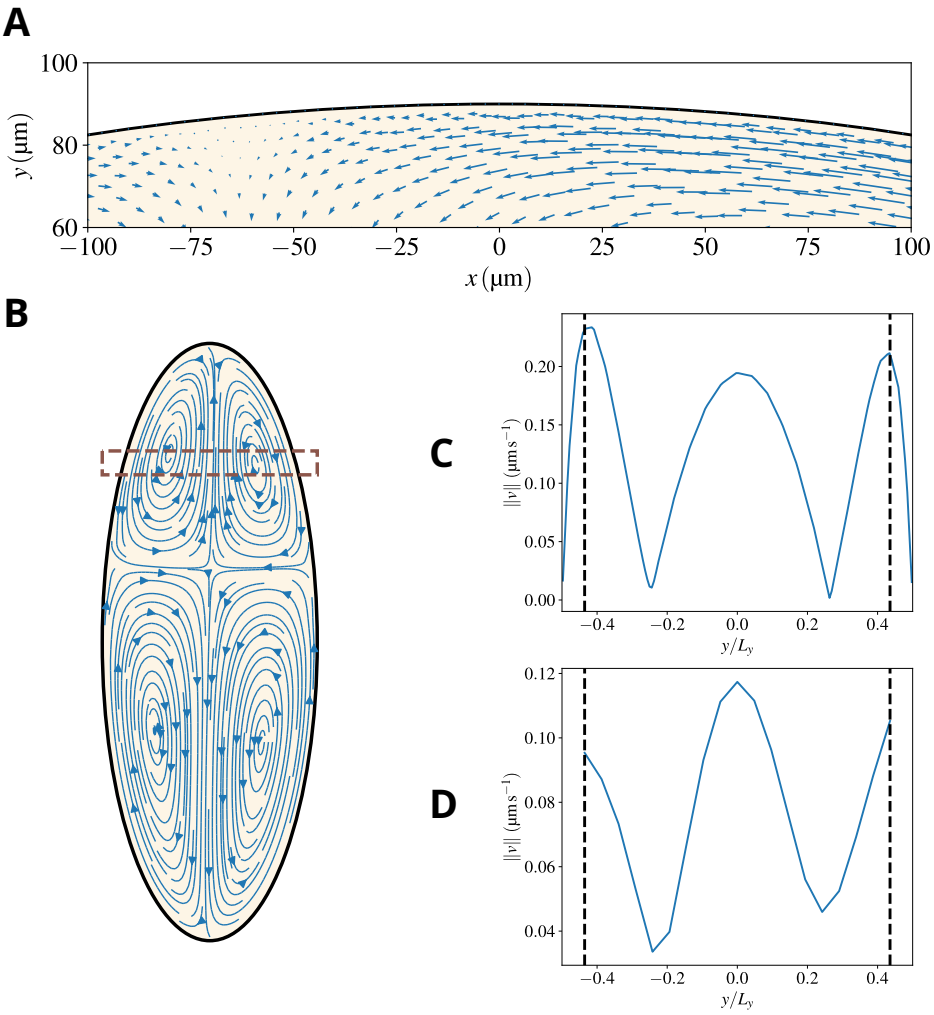

Fig. II.10 **Our model predicts a thin boundary layer close to the cortex.** *A) A zoom of the region close to the cortex, meant to highlight that substantial cytoplasmic flows are observed relatively close to the cortex, as observed in experiments. In fact, the no-slip boundary condition forces the sol velocity to drop to zero at the cortex but the decrease is sharp and happens in a boundary layer that is micron-thick. This is visually demonstrated by taking the velocity in the box shown in panel (B) and plotting its amplitude vs the position (normalized by the width of the embryo at that AP position). Panel (C) shows results for our simulations, and panel (D) for an analogous region in the experiments. The segmented vertical lines represent the point from which no experimental velocities can be resolved, which reinforces the impossibility of resolving a boundary layer such as the one present in the simulations with the available experimental data.*

the sol velocity drops abruptly from its bulk value to zero. This would also be consistent with the fact that the typical size of the cortex is a few hundred nanometers.

To estimate the width of the boundary layer, we take the difference in Eq. II.32 :

$$\Delta(\omega_v - \omega_u) = \kappa^2(\omega_v - \omega_u)\,, \tag{II.33}$$

which identifies the reciprocal of a lengthscale $\kappa = \sqrt{\Gamma(\eta+\eta_s)/(\eta\eta_s)}$ that vanishes in the absence of friction. The parameters that allowed us to reproduce experimental observations yield $1/\kappa \simeq 7\mu m$, consistent with previous remarks on the width of the boundary layer. As noted above and shown in Fig. II.10D, this fine resolution was not accessible in the experiments in Ref. [54] and constitutes a prediction that awaits experimental validation. From a numerical standpoint, properly capturing the boundary layer required an adaptive mesh, sub-micrometer sized near the embryo boundary, which allowed us to resolve the flow within the boundary layer (see Methods for details). Comparison of the flow speed of the gel and the sol indicates that the gel moves faster than the sol. Despite this differential movement, no significant shear is expected between the two fluids, as the gel turns over very rapidly (over timescales of seconds).

Note finally that our model provides insights into the physical properties of the actomyosin gel and the sol. In particular, reproducing experimental speeds requires the viscosity of the gel to be a few orders of magnitude larger than the viscosity of the sol. This is consistent with independent experimental data reporting $\eta_{gel}/\eta_{sol} \approx 10^5$ [118].

II.2.8 Gel-mediated transport leads to non-trivial myosin dynamics

Experimental data [54] show the peculiar time profiles of Myosin II (see the Supplementary Fig. S3 of Ref. [54] for similar plots for F-actin) for cell cycles 5-6 at the embryo surface and varying distances from it. Peaks of myosin concentration are strongest at the cortex and decay over a few microns away from it, as shown in Fig. II.11. The other characteristic feature is that the peaks are delayed at various depths, with the earliest peak at the cortex and the deeper ones progressively delayed.

The above behavior is captured by our model, as shown in Fig. II.11A. The qualitative reason underlying these trends is intuited from the interplay between gel flow and diffusion of unbound components. In a nutshell, the dynamics has two phases. During early interphase, gel flows drive the rapid recruitment of myosin to the cortex where it accumulates in the bound state. The width of its peak close to the cortex reflects the rapid decay of the ρ_g field defined in Eq. II.26. In the subsequent second phase, at mitotic entry, the PP1 activity decreases, and gel flows dampen. Then, the dynamics is dominated by diffusion of the unbounded components which tend to move from the cortex (zone of high concentration) toward the interior of the embryo. The delays as a function of the depth are caused by the time taken by the excess myosin that unbinds at the cortex to progressively diffuse back. Fig. II.11C highlights the role played by the active nature of the gel fluid : if we suppress activity by putting $\sigma_a = 0$ in Eq. II.17, variations in myosin levels are much reduced and the order of the delays among the peaks at different depths is lost.

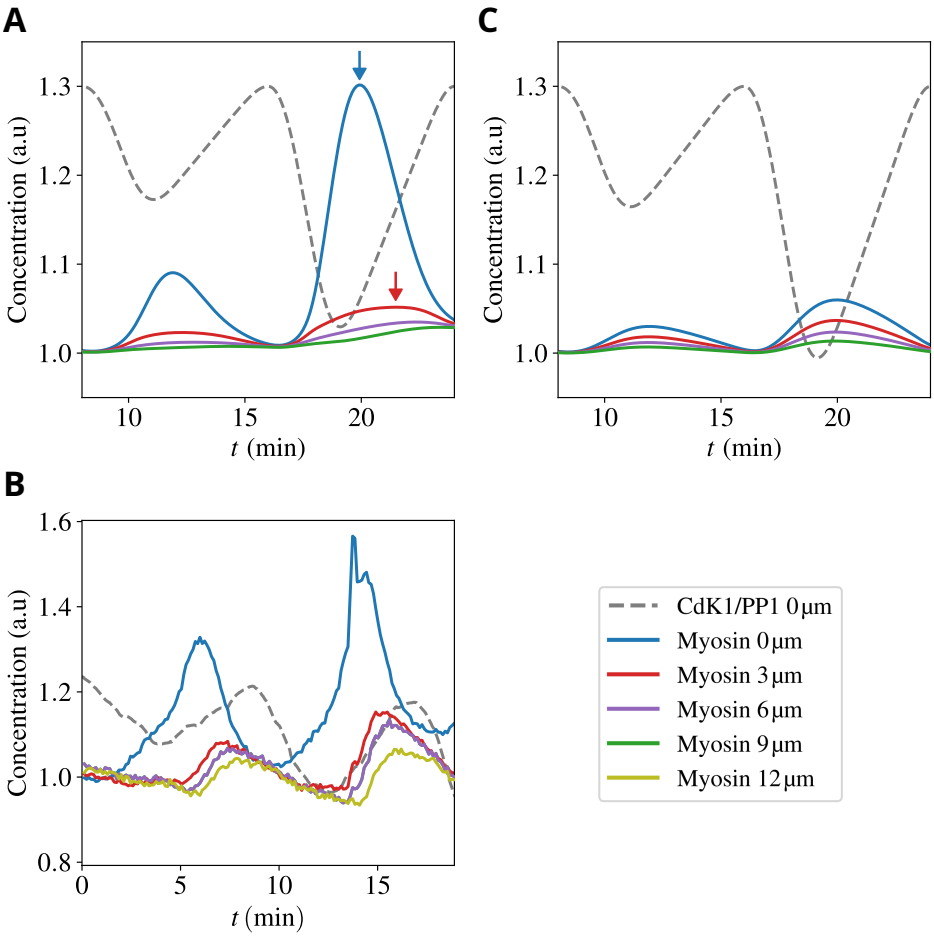

Fig. II.11 **Myosin dynamics in the early embryo**. *Upper and middle panels : Total concentration of myosin for cell cycles 5-6 at embryo surface (blue line) and varying distances from the surface (see legend) in our model (A) and experiments (B). Colored arrows locate the maxima of the curves. Dotted black line : The Cdk1 to PP1 ratio, which constitutes a proxy for the phase of the cell cycle. Lower panel : Total concentration of myosin for the same conditions as in panel (A) but for a passive gel, i.e., suppressing the active component* σ_a *of the stress in Eq. II.17.*

II.2.9 Nuclear positioning is a self-correcting process

The position of the nuclear cloud at the beginning of cycle 4, when flows start, reflects the position of the initial nucleus in the embryo, which is subject to fluctuations [54]. What is the influence of that position on the flow structure and will the final distribution of nuclei, at the end of cycle 7, be affected ? In other words, are the flows able to buffer shifts and distortions of the nuclear cloud at the beginning of cycle 4 and still achieve a uniform spreading of the nuclei ?

The answer to this question is summarized by Fig. II.12, where we have simulated various initial positions and reported the difference of the nuclear positions with respect to the reference configuration where the initial nucleus is placed at 40% of the total AP length of the embryo. Several remarkable features can be noted. First, irrespective of the initial position, the cloud of nuclei converges to very similar final configurations. Second, the role of forward and backward flows is apparent from the figure : the distance to the reference configuration decreases during the forward phases and flattens or even increases during the phases of backflow. Third, the final differences between the actual and the reference positions are only a few microns, defining the degree of robustness of the process.

The reasons underlying this striking property of the cytoplasmic flow reside in what was stressed in previous sections : myosin accumulation and contractions are localized at the position of the nuclear cloud. That defines the location where the sol will flow in the bulk and extend. If the initial location is sufficiently central, as it typically is, then four vortices are created and an extension both on the anterior and posterior sides is produced. Conversely, if the initial position is very anterior (or posterior), then the flow points in the opposite direction toward the posterior (or anterior). The net effect is that the modified dynamics compensates for the displacement of the initial nucleus and readjusts the final position of the nuclei as demonstrated by Fig. II.12.

We also tested the ability of the flows to center nuclei in response to displacements in directions perpendicular to the AP axis (see Fig. A.3). We found that the flows are able to center the nuclei and ensure that the nuclear cloud sits in the middle of the embryo. The reason for this is intuitive. If nuclei are closer to one side of the cortex than the other, PP1 activity and myosin recruitment are higher on that side and, as a consequence, that side will experience a stronger contraction and flow, which will help to center the nuclei.

II.2.10 Cytoplasmic flows weakly affect the formation of the Bicoid gradient

Cytoplasmic flows at cycles 4-6 are concomitant with the initial stage of the establishment of the Bicoid gradient [119]. Bicoid is a morphogen that generates an exponential gradient essential to pattern the embryo AP axis [120], [121]. The formation of the gradient is controlled by the localization of *bcd* mRNA to the anterior of the embryo [122]. The mRNA is translationally silent until fertilization when the localized production coupled with protein motion starts the process that eventually establishes the gradient [119], [122]. The movement of the protein has been hypothesized to be dominated by diffusion [123]. However, the formation of the Bicoid gradient is not fully understood and it has been suggested that flows might play a role in ensuring that the Bicoid gradient achieves the appropriate length [124]. However,

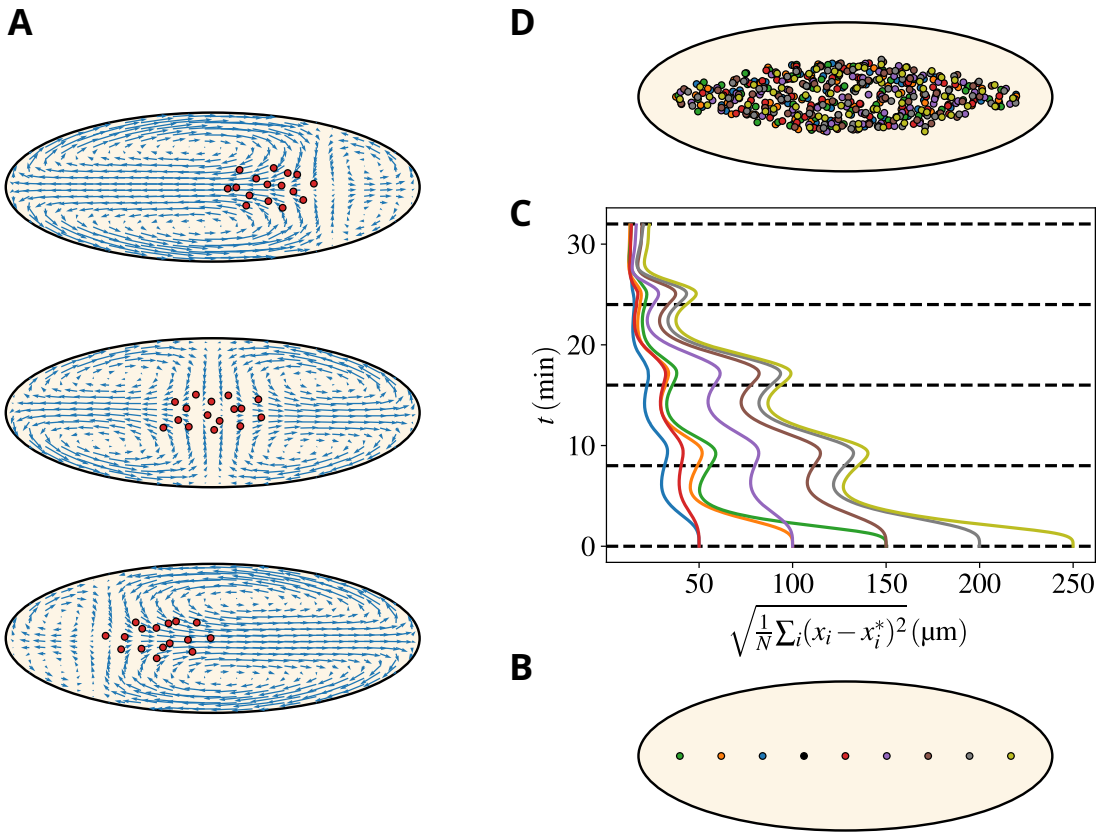

Fig. II.12 **Flows ensure a uniform distribution of nuclei along the AP embryonic axis irrespective of the initial nucleus' location.** *A) Three different flow geometries controlled by the location of the nuclear cloud, illustrating the self-centering effect. B) A series of positions (coded by different colors) for the first nucleus that starts the division cycles. The nine different locations go from 10% to 90% of the embryo AP length. The reference configuration has the nucleus placed at 40% of the embryo AP length. C) The evolution in time (flowing upwards) of the distance with respect to the reference configuration. The distance is defined as* $\frac{1}{N}\sum_{i=1}^{N}(\mathbf{x}_i - \mathbf{x}_i^*)^2$*, where* N *is the total number of nuclei (at that time),* $\mathbf{x}_i^*$ *and* $\mathbf{x}_i$ *are the positions of nuclei in the reference or the displaced configurations. The best matching that minimizes the total distance between the two sets of nuclei is obtained by using the Belief Propagation algorithm described in the Methods. Colors of the curves correspond to the initial positions in the bottom panel. Three pairs correspond to the two sides of the reference positions and the last two curves refer to the initial positions at 80% and 90% of the AP length. D) The final configurations of nuclei (for the whole ensemble of colors). Note that all colors are mixed up, witnessing the self-correcting nature of the AP spreading process. That is shown more quantitatively by the middle curves, which all reduce to values corresponding to distances of a few microns distance between pairs of nuclei of the various configurations.*

this hypothesis has remained largely untested due to a lack of quantitative information on the structure of cytoplasmic flows.

To test the influence of cytoplasmic flows on Bicoid gradients, we used the flow generated by our model above and simulated the dynamics of Bicoid transport by using measured mRNA distributions and assuming that protein production begins at fertilization. Bicoid molecules are dispersed by the joint effect of molecular diffusion and cytoplasmic flows. The minimal assumption is that Bicoid initially does not preferentially localize to the cortex or the bulk. Results for the evolution of the Bicoid concentration are reported in Fig. II.13. Color-coded Bicoid profiles at various times are shown in panel A. The profiles at cycles 4-7 in panel B agree with the experimental curves reported in [125]. In our model, we can easily turn off the flows and ascertain their effect on the gradients' formation. The corresponding curves illustrate that the differences with and without flows are minor. More specifically, in the anterior part of the embryo, the flow at the cortex tends to push Bicoid toward the mid-embryo and the curves with the flows on are therefore slightly higher than without. The effect is reversed beyond mid-embryo but remains minor. Moreover, effects on Bicoid spreading are predicted to be temporary : by cell cycles 7-8, Bicoid distribution is essentially indistinguishable with and without flows. Additional evidence is provided in Fig. A.4. We conclude that flows have a minor influence on the formation of the Bicoid gradient.

To test this prediction experimentally, we compared the Bicoid gradient in wild-type embryos and mutant embryos, featuring severely reduced cytoplasmic flows. To this end, we used *cullin-5* (*shackleton*) mutant embryos, which we have previously shown to display strongly reduced cortical contractions and cytoplasmic flows [65]. Consistent with a minor and transient role for flows in controlling the Bicoid gradient, we found that the gradient at

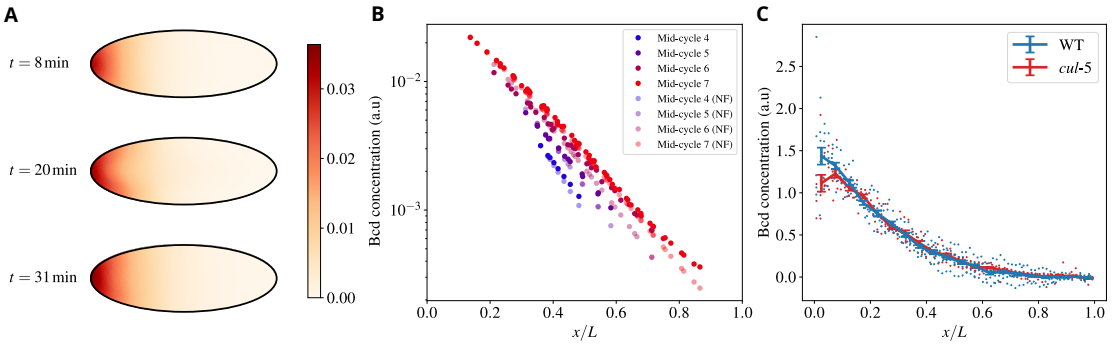

FIG. II.13 **Embryonic cytoplasmic flows weakly affect the establishment of the Bicoid morphogenetic gradient.** *A) Heatmap showing the Bicoid concentration profile in the embryo, and the characteristic half-moon shape with the concentration higher at the cortex than in the bulk. B) The concentration of Bicoid vs the (normalized) position along the AP axis for various cycles, as indicated in the color legend. NF stands for "No Flow", i.e., situations where cytoplasmic flows were suppressed. Values are reported at the position of each nucleus. C) Experimental comparison of the Bicoid gradient at cell cycle 13 in wild-type and cullin-5 mutant embryos, where flows are strongly suppressed [65]. Datapoints were binned in each case, with the continuous line and error bars representing each bin's average and standard error respectively.*

cell cycle 13 is essentially indistinguishable in wild-type and *cullin-5* mutant embryos.

In sum, even though the presence of cytoplasmic flows might *a priori* influence the formation of the Bicoid gradient, in practice the structure of the flows actually observed in the embryo is such that their influence is minor and they weakly and transiently affect the formation of Bicoid gradients.

II.2.11 Embryo shape modulates the strength and asymmetry of the flows

As a further test of our model, we performed various simulations altering the geometry of the embryo. The resulting dynamics is well captured by the following intuitive considerations, which run similar to those explaining the self-correcting nature of the AP expansion demonstrated in Fig. II.12. The cortex points which are closest to the nuclear cloud define the regions where myosin-II accumulates and sets the locations of the strongest contraction. In the wild-type and the usual geometry, these points will determine where the gel flows are directed and define the corners of the vortices observed in the sol flows. An important role is played by the elliptic geometry of the embryo since the transversal distance between the AP axis and the cortex reduces as one moves toward the poles. A first expected effect is that, as the ratio between the major and minor axes of the ellipse reduces to unity, the dynamics becomes more isotropic, and therefore the ratio between longitudinal and transverse speeds should tend to unity. The second expected effect is a global reduction in the overall speed, which can be linked to two different causes. First, due to changes in embryo geometry on average nuclei will be further away from the cortex, and the PP1 cloud will not activate as much myosin as in the wild-type case. Furthermore, as the egg becomes more symmetric, the shape of the PP1 isolines becomes closer to the shape of the egg, thus reducing the myosin gradients and the strength of the flows.

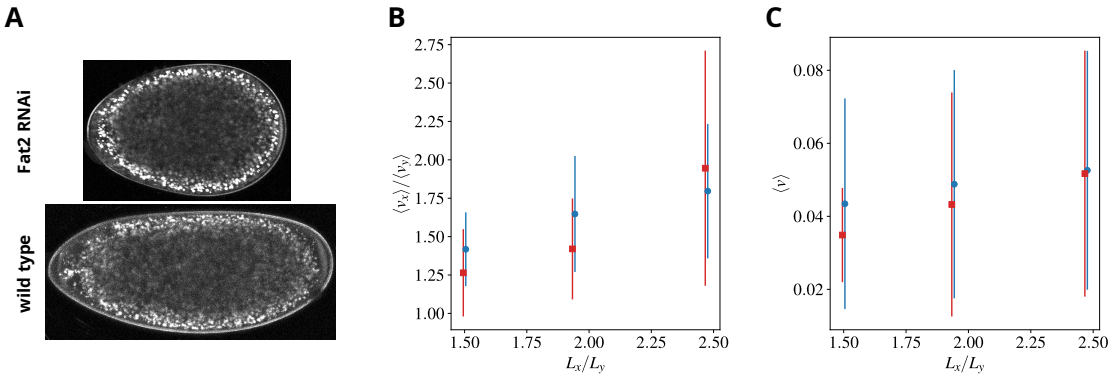

FIG. II.14 **Predictions and experimental verification of flows in rounded embryos** *A) A wild-type and a round embryo are shown in the lower/upper panels, respectively. Mutants are generated by using a knockdown of Fat2 (Fat2 RNAi), a major regulator of the elongation of the egg chamber. Panels B) and C) show the ratio between the embryo-averaged longitudinal and transverse sol speeds and the embryo-averaged sol speed, respectively, time-averaged over CC6. Simulation/experimental data are shown in blue circles/red squares, respectively. Error bars represent the standard deviation of the space averages during CC6.*

To test our predictions, we generated embryos of different geometry by using a knockdown of Fat2 (Fat2 RNAi), a major regulator of the elongation of the egg chamber, in somatic cells of the female ovary [126], [127]. Notably, these experiments are performed by directing the expression of the RNAi transgene to the somatic cells of the egg chamber, thus embryos of different geometry but genetically wild-type can be generated, see Fig. II.14A. These embryos show patterns of flow that differ significantly as compared to the wild-type. In particular, the ratio between longitudinal and transverse speeds, as well as the overall speed, reduce (see Fig. II.14B,C) in agreement with our theoretical predictions.

II.3 Discussion

We have presented a theoretical framework that quantitatively captures the main mechano-chemical couplings underlying the cytoplasmic flows in the early *Drosophila* embryo. As in most developmental and cellular conditions, Reynolds numbers are low, and fluids are well described by neglecting accelerations (Stokes' conditions). The behavior of a Stokes fluid is determined by its velocity at the boundary of the region of interest [112], a property that underlies most of previous works on cytoplasmic flow. There, the velocity at the boundary of the cell or the embryo was prescribed, e.g., by the measured velocity, and it was then shown that the cytoplasmic flow is well described by solving Stokes' equations with the prescribed boundary conditions [82], [84], [92]. The velocity at the boundary often involves active mechanisms, e.g., generated by active actomyosin contractions. In multicellular systems, active myosin at the cell-cell interfaces can drive tissue-wide cellular flow, as shown in *Drosophila* gastrulation [128]. Global morphogenetic flow is accurately predicted by the spatial distribution of myosin motors. Similarly, a tensile ring in the quail embryo drives movement in the gastrulating amniote embryo [35], [47]. Here, we have coupled the mechanics of Stokes flows to the cell cycle via some of its major chemical components (Cdk1 and PP1). Nuclei in the fly syncytium regulate the balance between Cdk1 and PP1, which itself controls the activation of myosin via Rho. We have shown that fundamental and empirical reasons impose a multiphase model that features a mixture of a passive and an active fluid. The active gel can slide along the cortex and generates the cortical forces that propel the ensemble of the two fluids and the transport of nuclei in the bulk of the embryo. The passive phase satisfies no-slip boundary conditions and the sol fluid is thus at rest at the plasma membrane, which is adjacent to the immobile *Drosophila* vitelline membrane. A major result emerging from our work is that the two phases move differently, and a single-fluid description is insufficient to capture the complexity of cytoplasmic flows in fly embryos. Previous discrepancies from a Stokes' flow of the sol vorticity [54] can thus be understood as reflecting the transfer of momentum between the active and passive phases due to their mutual friction. The entrainment of the passive fluid by its active counterpart concentrates in a thin boundary layer close to the cortex, which constitutes another striking result emerging from our work. In the boundary layer, the velocities of the two phases change sharply to accommodate their respective boundary conditions. The corresponding thickness is predicted to be a few microns.

Our framework recapitulates previous observations and, most importantly, offers new predictions to inspire experiments. The results on round embryos that we presented here provide a notable example of theoretical predictions that we could already confirm expe-

rimentally. Numerical simulations of our model predict the extent to which the amplitude and geometry of cytoplasmic flows would change with embryo shape. These predictions were supported by experiments in which embryos of different geometry were generated via genetic engineering. In particular, by knocking down Fat2 expression (via RNAi) in the somatic cells of the egg chamber, we could obtain embryos having a round geometry [126], [127]. In these embryos, the observed cytoplasmic flows were found to be in agreement with our theoretical predictions. Another example of what theory can uniquely offer is provided by our predictions on the role of cytoplasmic flows in the establishment of Bicoid gradients. Specifically, we capitalized on the possibility of direct and unequivocal comparison of gradients with and without cytoplasmic flows to demonstrate their minor role in the establishment process of Bicoid gradients.

In the future, there are several new experiments suggested by our theoretical results. A first example is provided by the robustness of the spreading process with respect to the position of the initial nucleus that we highlighted here. The procedure that we have implemented in numerical simulations suggests set-ups to reproduce it experimentally. For example, one could use optogenetic control of myosin activity to displace the position of nuclei at early cycles [54] and observe whether or not flows compensate for the displacement and still drive uniform positioning in later cycles.

A crucial test of our theoretical framework will be the experimental verification of the gel flow and the presence of a sharp boundary layer. Experimental challenges will need to be overcome to obtain accurate measurements of the flow of the actomyosin gel. First, it is difficult with current fluorescent probes to distinguish whether myosin is in the active (bound) or inactive (unbound) state. Second, imaging of myosin deep in the embryo does not show significant features to infer possible flows. On a positive note, it is relatively straightforward to measure the total concentration of myosin and quantify myosin concentration at different distances from the cortex. Our simulations recapitulate the measured concentration data (see Fig. II.11), arguing that we captured the essential features of the gel flow. Our simulations predict that the gel flow drives cortical recruitment of active myosin, which is the main driving force of the nuclear spreading process. Approaches based on Fluorescence Recovery After Photobleaching (FRAP) could be used to infer average flows across large regions of the embryo [54], [129]. FRAP of fluorescently tagged myosin near the cortex could potentially confirm that the gel flow is directed mainly towards the cortex (as we predicted here for the gel) rather than sliding parallel to it (as we predicted for the sol). However, testing this prediction experimentally will be strongly influenced by the ratio of the concentration of active and inactive myosin and the results could be difficult to interpret. Thus, we propose that novel experimental approaches are needed to accurately measure the gel flow. Developing such methods will not only reveal fundamental insights into the mechanisms of cytoplasmic flows but will also allow testing the hypothesis that the viscosity of the two fluids is very different, a property that is essential in our model to generate the observed flows of cytosol. Similarly, it will be important to develop experimental approaches to resolve the thin (few μm) boundary layers predicted by our theory. Particle Image Velocimetry allows tracking flows near the cortex [54] but assaying the localization of the tracked features relative to the plasma membrane has not been analyzed carefully to date.

Future experimental observations of the gel flow will be important not only to confirm

the current theoretical framework but also to refine and advance it. The isotropic form of the active stress tensor taken here was dictated by the parsimony principle and the fact that no current experimental observation forced us to introduce more sophisticated hypotheses (and the resulting additional fields). It is however quite conceivable that nematic and/or polar effects are present and our description should be upgraded to take them into account. A detailed classification of the additional fields and couplings are found in Ref. [108]. An experimental observable that will be highly informative in that respect is the gel vorticity, which would allow us to construct the total vorticity. Isotropic forms of the active stress tensor cannot produce vorticity, as shown here. The total vorticity is then harmonic, which strongly constrains its spatial structure (its extrema are confined to the boundary of the embryonic domain). Polar and nematic effects break isotropy and generically lead to the production of vorticity and the breaking of harmonicity. It would then be important to measure the total vorticity and assess the consistency of its spatial structure with the harmonic property.

One big simplification that allowed us to extract some information from the equations, and to ease the numerical solving, is to ignore the evolution of the actin network density and to consider it as homogeneous and isotropic. Strictly speaking, as the network flows, the filaments come closer together, and they might re-align. This is particularly important because we have assumed that the friction force is uniform, whereas in reality, it might depend on density. A closer look at fluorescent images reveals that the network is less dense in the bulk, which has been incorporated effectively into our model because the active gel does not advect the nuclei. In our case, the simplified scheme works because the activation of myosin is confined due to the distribution of Rho-GEF and the entrainment region is small, yet it is possible that in other systems where actomyosin deformations drive the production of flows these subtleties become more relevant.

In sum, the combination of discriminating experimental tests, new predictions, and suggested novel experiments presented here constitute exemplary instances of the value of the interplay between theory, numerical simulations, and quantitative experiments that we see as an exciting way forward in the field of developmental biology and embryology.

II.4 Methods and Materials

II.4.1 Fly Stocks

To image and quantify the Bicoid gradient, we used an EGFP-Bcd line (Bloomington stock 29018). For the analysis of the gradient in *cullin-5* embryos, we used the following females : EGFP-Bcd/EGFP-Bcd ; His2Av-mRFP/His2Av-mRFP ; $shkl^{GM130}/shkl^{GM163}$. To obtain round embryos, we crossed flies carrying a *UAS :Fat2* RNAi transgene (VDRC 5098, kind gift of Sally Horne-Badovinac) to flies expressing Gal4 under the *trafficjam* promoter to restrict expression in the somatic cells of the egg chamber (kind gift of Sally Horne-Badovinac). We then selected female flies carrying both transgenes and set up cages to collect embryos where the activity of Fat2 was reduced specifically in the somatic cells of the female ovary. In some experiments, embryos also expressed PCNA-TagRFP to visualize nuclei.

II.4.2 Embryo Manipulations

Following collection, embryos were dechorionated with 50% bleach for 1 min, rinsed with water, mounted in halocarbon oil on a gas-permeable membrane, and covered with a glass coverslip. To visualize cytoplasmic flows, yolk granules were stained by permeabilizing embryos with a solution of 10% CitraSolv in water for 2 minutes and immersing them in Trypan Blue for 1 minute.

II.4.3 Microscopy

Imaging experiments were performed with an upright Leica SP8 confocal microscope, a 20 X /0.75 numerical aperture oil immersion objective, an argon ion laser, and a 561-nm diode laser, as described in Ref. [54]. For the analysis of the Bicoid gradient, images were acquired on the mid-sagittal plane with a time resolution $\simeq 12s$. For the analysis of cytoplasmic flow in wild-type embryos, we used data in Ref. [54], where we acquired stacks of raw confocal sections (800 x 400 pixels, pixel size : 0.727 μm) of yolk (Trypan Blue) and nuclei (PCNA-TagRFP) with an axial distance of 50-60 μm and sampling of 20 s. For the round embryos, we acquired images (1024x1024 pixels, pixel size : 0.568 μm) of yolk at about 40 μm from the cortex and sampling $\simeq 10 - 20s$.

II.4.4 Image and data analysis

Particle Image Velocimetry

Raw confocal images of yolk granules were Gaussian-filtered (width of 10 μm and standard deviation 6 μm) to increase the signal-to-noise ratio as a pre-processing image analysis step. Cytoplasmic velocity fields were measured by means of Particle-Image-Velocimetry. Briefly, stripes of 35 μm (Anterior-Posterior direction) by 15 μm (Dorsal-Ventral or lateral direction) were used as templates and probed within regions of 60 μm by 30 μm to find the best correlation spots, with a threshold correlation coefficient of 0.7. PIV was calculated for 10,000 unique points randomly distributed in the embryo at each time interval. A sampling of around 20 to 30 s was used to get reliable local displacements while maintaining high correlations. The obtained velocity fields were time-averaged over a range of 10 s and linearly interpolated on a square grid with 4 μm spacing.

Quantification of the Bicoid gradient

The nuclear segmentation masks of the *Drosophila* embryos were generated with Ilastik 1.3.3 software [130] by using the Pixel Classification pipeline. The segmented nuclear region was binned along the AP axis, with bin width 7.27 μm (10 pixels, pixel size = 0.727 μm). The average pixel intensity of the EGFP-Bicoid channel was calculated for each binned region of the nuclear mask. Next, 11 consecutive frames (frame rate = 12.56 s) were manually selected right before the mitosis of cell cycle 13 (cc13). The average of these 11 frames was taken for each bin to generate the Bicoid gradient profile. The gradients were normalized

as follows : first, the positions of the bins were normalized by the length of the embryo ; second, an offset was determined by the average intensity of the 10% posterior-most bins and subtracted from the profile ; third, the value at each bin was normalized by the average intensity (post-offsetting) of the 10-20% anterior-most bins. The final profiles of 6 wild-type embryos and 4 *cullin-5* mutant embryos were reported.

II.4.5 Numerical simulations

Space and time discretization

We performed numerical simulations by using a finite-element method, implemented in a custom FreeFem++ code. Different meshes were generated for each geometry with an adaptive edge size, such that the boundary layer could be well resolved. The target minimum edge size was chosen as $h_{min} = 0.75\,\mu\text{m}$, and we used a fixed timestep $\Delta t = 3 \times 10^{-2}\,\text{s}$. The element types were chosen as MINI elements (Linear element + order 3 bubble) for $\boldsymbol{u}$ and $\boldsymbol{v}$; discontinuous linear elements for ρ_b and ρ_u ; linear elements for the remaining fields. The mix of MINI elements for the velocity space and linear elements for the pressure space ensures the solution is unique, satisfying the discrete inf-sup condition [131]. Since the flow and myosin dynamical equations are coupled, we sequentially solved them. Specifically, at timestep n we first calculate $\boldsymbol{v}^n$ and $\boldsymbol{u}^n$ from ρ_b^n and Ξ^n ; then we obtain ρ_p^n from the nuclei positions $\boldsymbol{r}^n$, and determine the microtubule lengths ℓ^n ; ρ_b^{n+1}, ρ_u^{n+1} and ρ_p^{n+1} are calculated next, followed by $\boldsymbol{r}^{n+1}$ from $\boldsymbol{v}^n$ and ℓ^n ; finally, we determine $\langle s \rangle^{n+1}$ and Ξ^{n+1} from $\boldsymbol{u}^n$.

Myosin dynamics

Eqs. (II.26,II.27,II.28) are conveniently written in a compact form as

$$\frac{\partial \boldsymbol{\phi}}{\partial t} = \mathcal{L}\boldsymbol{\phi} + \boldsymbol{N}\,, \tag{II.34}$$

where $\boldsymbol{\phi} = \rho$ for Eq. II.26 and $\boldsymbol{\phi} = (\rho_b, \rho_u)$ for Eqs. (II.27,II.28). $\mathcal{L}$ represents linear parts of the equation, viz. $\mathcal{L} = -1/\tau$ and $\mathcal{L} = \begin{pmatrix} D_b\Delta - k_u & 0 \\ k_u & D_u\Delta \end{pmatrix}$, respectively. Conversely, $\boldsymbol{N} = k'\rho_g \frac{\rho_p(t)}{\rho_p(t)+K_p}$ and $\boldsymbol{N} = (k_b\rho\rho_u - \nabla\cdot(\boldsymbol{u}\rho_b)\,, -k_b\rho\rho_u - \nabla\cdot(\boldsymbol{v}\rho_u))$ for the two cases. Eq. II.34 is solved as

$$e^{-\mathcal{L}\Delta t}\boldsymbol{\rho}(t+\Delta t) = \boldsymbol{\rho}(t) + \int_t^{t+\Delta t} e^{-\mathcal{L}(t'-t)}\boldsymbol{N}(t')\,\mathrm{d}t'\,, \tag{II.35}$$

and the integral was approximated by using $N(t') \simeq N(t) + (N(t) - N(t-\Delta t))(t'-t)/\Delta t$ to finally obtain :

$$(1 - \mathcal{L}\Delta t)\,\boldsymbol{\rho}(t+\Delta t) = \rho(t) + \frac{3}{2}\boldsymbol{N}(t)\Delta t - \frac{1}{2}\boldsymbol{N}(t-\Delta t)\Delta t\,, \tag{II.36}$$

The initial conditions were $\rho_u = 1$ and $\rho_b = 0$ everywhere. At the boundary, the fields satisfy no-flux conditions, which ensure that the total amount of myosin in the embryo is constant.

Bicoid dynamics

We modeled the dynamics by the equation

$$\frac{\partial \rho_p}{\partial t} + \nabla \cdot (\boldsymbol{v}\rho_p) = D_p \Delta \rho_p - \frac{1}{\tau_p}\rho_p + k_m \rho_m \,, \tag{II.37}$$

The Bicoid mRNA distribution ρ_m decays exponentially from the anterior pole $\rho_m(\boldsymbol{r}) = e^{\|\boldsymbol{r}-\boldsymbol{r_A}\|/\mu_m}$, where $\boldsymbol{r_A}$ is the position of the anterior pole. By defining $\mathcal{L} = D_p\Delta - \frac{1}{\tau_p}$, and $N(t) = -\nabla \cdot (\boldsymbol{v}\rho_p) + k_m\rho_m$, we can solve this equation as explained above. Our initial conditions have $\rho_p = 0$ everywhere.

Cortical actomyosin dynamics

As mentioned in the main text, backflows are explained by the elastic recoil of actomyosin filaments, which attach and detach to the cortex. If i denotes a generic boundary node and $\langle s_i \rangle$ represents the mean displacement of filaments attached at i (positive for counter-clockwise displacements), evolution of the displacement is given by :

$$\langle \dot{s}_i \rangle = -\frac{1}{\tau_c}\langle s_i \rangle + \frac{k_c \tau_c}{1 + k_c \tau_c} u_t \tag{II.38}$$

where u_t is the component of the gel velocity tangent to the boundary at the displaced location. This equation was solved as described above with $\mathcal{L}$ accounting for the decay term with typical rate $\frac{1}{\tau_c}$, and $N(t)$ the non-homogeneous last term on the r.h.s of the equation. A value $\tau_c = 4\,\mathrm{min}$ reproduced the backflow delay and duration. Similar values for the cortical elasticity relaxation timescale have been reported in previous experimental works using ferrofluids at the beginning of cellularization [132]. We have used $k_c = 4\,\mathrm{min}^{-1}$.

Nuclear dynamics

Based on the ellipsoidal flow geometry observed in previous experiments [54], we exploited the cylindrical symmetry around the AP axis and performed simulations in a two-dimensional domain representing a mid-embryo slice. In order to take into account the third (z) dimension into account, we proceeded as follows. First, from the x and y positions of nuclei, we built Δ_x and Δ_y, the maximum nucleus-nucleus distance in x and y, and their center of mass. Second, a 3d ellipsoid is built at the center of mass and semimajor axes $\Delta_x/2$, $\Delta_y/2$, and $\Delta_y/2$. The last step enforces the cylindrical symmetry. Third, z-coordinates of nuclei are assigned so that each one of them lies at the boundary of said ellipsoid. For each nucleus there are two possible z-coordinates : if the previous z-coordinate is non-zero, its sign is preserved ; else, it is chosen at random. Finally, distances required for microtubule-mediated interactions (Eq. II.30), PP1 activity (Eq. II.22) and pair matching algorithm, all considered 3d distances.

Eqs. (II.29) for the nuclei were integrated using a 1-step Euler method. To obtain nuclear separations comparable to the experiments, we chose $\ell_{min} = 1\,\mu\mathrm{m}$, $\beta = 1\,\mu\mathrm{m}$. At mitotic exit, we duplicated each nucleus, choosing a random axis of division and placing two daughter nuclei at a distance $r_{mit} = 2\,\mu\mathrm{m}$ along the division axis. Initial conditions in the unperturbed embryo considered a single nucleus along the AP axis and $50\,\mu\mathrm{m}$ to the left of the center.

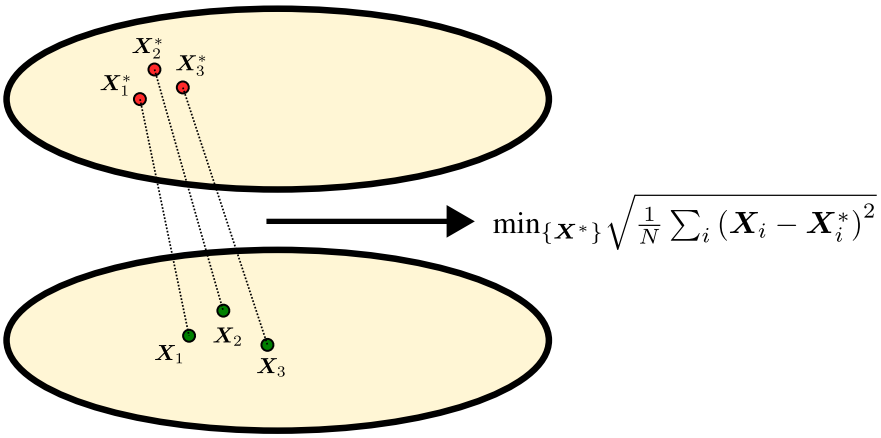

FIG. II.15 **Pair matching**. *Sketch showing the reference distribution* $\{\boldsymbol{X}_i^*\}_i$ *and the perturbed distribution* $\{\boldsymbol{X}_i\}_i$ *at a particular time. The lines indicate the matching that minimizes the mean squared displacement between the two different distributions.*

Pair matching

To produce Fig. II.12, we had to find the best matching between two sets of particles (Nuclei). Matching two sets of particles in two different image frames is conveniently formulated as the matching in a bipartite graph so that a certain edge-weight dependent quantity is minimized [133]. This problem is well-known in graph theory [134], and efficient algorithms are available [135]. In our case, for each timestep, the two sets $\{\boldsymbol{r_i}(t)\}$ and $\{\boldsymbol{r_i^*}(t)\}$ represent the set of nuclei positions in a reference simulation and another simulation where the initial nucleus has been displaced. To find the matching which minimizes the RMS particle-particle distance, we implemented the simplified min-sum algorithm described in [135], with a weight function $\omega_{i,j} = e^{-\beta(\boldsymbol{r_i}\cdot\boldsymbol{r_j^*})}$, and $\beta = 0.002$ (see II.15 for an example of a match between two sets and the objective function to minimize).

III – Analytical results on a simplified model

The principal function of form is to advance our understanding. It is the organization of a piece which helps the listener to keep the idea in mind, to follow its development, its growth, its elaboration, its fate.

Arnold Schönberg

(This chapter and corresponding appendix are adapted from a manuscript in preparation by Claudio Hernández-López and Arghyadip Mukherjee)

III.1 Motivation & Modelling

III.1.1 A simplified sol-gel setting

The previously explored model in Chapter II allowed us to reproduce a wide variety of experimental features of the flows and nuclear transport in wild-type and mutant eggs of *Drosophila Melanogaster*. We showed that due to the nature of the mechanochemical coupling between the nuclei and actomyosin, the geometry of the domain impacts the shape of the flows, revealing a centering effect that corrects for perturbations in the initial position of the nuclear distribution. It would be insightful to know what key physical parameters affect these processes, and thus we ask the question, how simple can this configuration be such that we recover these flows and the nuclear transport ? Moving beyond studying the particular geometry of *Drosophila* and the biochemical details of its regulatory network, we would like to understand what kind of flow structures can be produced by such actomyosin-driven deformations in a general setting. Furthermore, even if we know that once a uniform nuclear distribution is reached the PP1 gradients are negligible, it could be that this uniform bound myosin setting is unstable, triggering actomyosin pattern formation and flows in the bulk as a result.

Hence, we will simplify the model as much as possible such that we can bring forward some more general ideas about these flows in different geometries. The first simplification that we can make is to assume that the sol and gel are not mixed. From Chapter II, we know

that the sol velocity peaks before dropping to zero in a boundary layer of a width that scales as the hydrodynamical length, i.e. the region where the gel entrains the sol. We can model this effect by having an active layer of width h next to the cortex, where h matches the hydrodynamical length. The rest of the system, i.e. the bulk, will be filled by the cytosol. As mentioned in Chapter II, $h \sim 7\,\mu\text{m}$, and the typical lengthscale of the embryo is $L \sim 100\,\mu\text{m}$. In all the geometries that we will explore, as in the real system, we will restrict ourselves to $h \ll L$ such that our approximation is meaningful.

The first consequence of this simplification is that the strength and geometry of the gel flow do not depend on the sol flow. To model the fluid-fluid boundary between the sol and gel, we will consider a tangential stress continuity boundary condition :

$$\underline{\underline{\sigma}}^{\text{gel}}\hat{\boldsymbol{n}} \cdot \hat{\boldsymbol{t}} = \underline{\underline{\sigma}}^{\text{sol}}\hat{\boldsymbol{n}} \cdot \hat{\boldsymbol{t}} \tag{III.1}$$

As we shall see in our geometries of interest, this amounts to equating the velocity of the gel flows to a multiple of the vorticity of the sol at the interface. This proportionality factor will depend on the ratio between the gel and sol viscosities and the thickness of the gel layer. As there is no gel in the bulk, the cytosol vorticity is a harmonic function, and the values at the interface propagate in the bulk. Hence, under this approximation, the maxima and minima of the sol vorticity in the interior of the egg are present at a distance h from the boundary. This allows us to relate the parameters of the model to real-world data.

It is clear that this simplified setting ignores the transport of bound myosin towards the cortex, which resulted in strong peaks in its concentration and time delays as a function of the distance to the cortex. As a result, the model should underestimate the accumulation of myosin and the localization of the flows.

This model is further simplified by ignoring the non-linearities in the myosin binding and contraction strength, such that :

$$\frac{\rho_b}{\rho_b + K_b} \to \rho_b \ , \tag{III.2}$$

where ρ_b is the bound myosin distribution. This means that our results overestimate the flow effects at high concentrations. The other approximation that we can make is to assume that there is abundant unbound myosin, and that its diffusion is orders of magnitudes larger than the bound myosin diffusion, which was discussed in the previous chapter. If so, we can ignore its spacetime evolution and assume it as homogeneous. Then, full system of equations that we are interested in, for a 2d cortical surface and a 3d sol :

$$\eta_s \Delta \boldsymbol{u} + \eta_b \nabla(\nabla \cdot \boldsymbol{u}) - \gamma \boldsymbol{u} = -\alpha \nabla \rho_b \ , \tag{III.3}$$

$$\frac{\partial \rho_b}{\partial t} + \nabla \cdot (\boldsymbol{u}\rho_b) = D_b \Delta \rho_b - k_u \rho_b + k_b \rho_p \ , \tag{III.4}$$

and in the bulk :

$$\eta \Delta \boldsymbol{v} - \nabla p = 0 \ , \tag{III.5}$$

$$\nabla \cdot \boldsymbol{v} = 0 \ , \tag{III.6}$$

where $\boldsymbol{u}$ is the gel velocity, η_s is the gel shear viscosity, η_b is the gel bulk viscosity, γ is an effective friction coefficient which models the interaction between the gel and the sol in the

entrainment region, α is the gel contractility, D_b is the diffusion of bound myosin molecules, k_u is the unbinding rate of bound myosin, k_b is the binding rate of myosin, ρ_p is the PP1 concentration, $\boldsymbol{v}$ is the sol velocity, and p is the pressure.

III.1.2 The stream-vorticity formulation and boundary conditions

For simplicity, let us consider a d=2 situation, i.e. the gel is confined to an unidimensional geometry. This situation can approximate the midplane of an axially symmetric flow, and allows for relatively simple mathematical calculations to determine the flow structure by utilizing the so-called stream-vorticity formulation. As mentioned in Chapter II, by taking the curl of Eq. III.5 :

$$\Delta\omega = 0 \ . \tag{III.7}$$

On the other hand, if $\boldsymbol{v}$ is divergence-free, it must derive from a particular vector potential. In particular, we can choose :

$$\boldsymbol{v} = \nabla \times (\psi \hat{\boldsymbol{z}}) \ , \tag{III.8}$$

and then :

$$\nabla \times \boldsymbol{v} = \nabla \times \nabla \times (\psi \hat{\boldsymbol{z}}) = \omega \ . \tag{III.9}$$

From the identity $\nabla \times \nabla \times \boldsymbol{A} = \nabla (\nabla \cdot \boldsymbol{A}) - \nabla \cdot \nabla \boldsymbol{A}$:

$$\Delta\psi = -\omega \ . \tag{III.10}$$

These equations must be complemented with boundary conditions. The no penetration boundary condition is straightforward to write :

$$\boldsymbol{v} \cdot \hat{\boldsymbol{n}} = \nabla \times (\psi \hat{\boldsymbol{z}}) \cdot \hat{\boldsymbol{n}} = 0 \ . \tag{III.11}$$

Now, the continuous stress boundary conditions. In the sol, the stress tensor reads :

$$\underline{\underline{\sigma}}^{\text{sol}} = -p\mathcal{I} + \eta \left((\nabla \boldsymbol{v}) + (\nabla \boldsymbol{v})^T \right) \ . \tag{III.12}$$

Then :

$$\underline{\underline{\sigma}}^{\text{sol}} \hat{\boldsymbol{n}} \cdot \hat{\boldsymbol{t}} = \eta \left((\nabla \boldsymbol{v}) + (\nabla \boldsymbol{v})^T \right) \hat{\boldsymbol{n}} \cdot \hat{\boldsymbol{t}} \tag{III.13}$$

$$= \eta \sum_{ij} \left(\partial_i v_j + \partial_j v_i \right) \hat{n}_i \hat{n}_j^{\perp} \ , \tag{III.14}$$

where we have used that $\hat{\boldsymbol{t}} = \hat{\boldsymbol{n}}^{\perp}$.

For example, in the simple case where the boundary is aligned with the y axis, and the cytosol occupies the region $x > 0$:

$$\underline{\underline{\sigma}}^{\text{sol}} \hat{\boldsymbol{n}} \cdot \hat{\boldsymbol{t}} = \eta \left(\partial_x v_y \right) = \eta\omega \ , \tag{III.15}$$

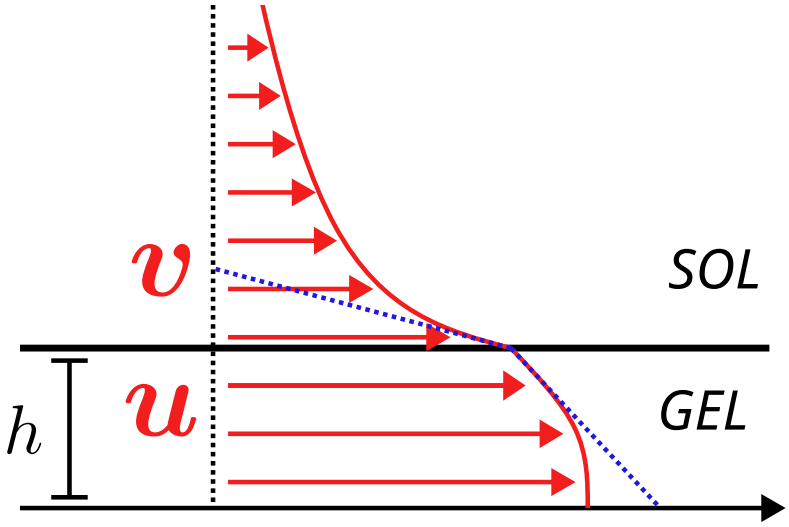

FIG. III.1 *Sketch showing the stress-matching boundary condition between the gel and the sol. The red profile and arrows represent the velocities at different distances away from the cortex, and the dotted blue lines show the discontinuity in the slope of the velocity profile when crossing the two media of differing viscosities.*

where we have used the no-penetration boundary condition to eliminate the $\partial_y v_x$ terms. If the boundary is curved this expression becomes more complicated, but it is still easy to treat in a circular domain. The elements of the stress tensor read :

$$\sigma_{rr} = -p + 2\eta \frac{\partial v_r}{\partial r} \ , \tag{III.16}$$

$$\sigma_{\theta\theta} = -p + 2\eta \left(\frac{1}{r} \frac{\partial v_\theta}{\partial \theta} + \frac{v_r}{r} \right) \ , \tag{III.17}$$

$$\sigma_{r\theta} = \sigma_{\theta r} = \eta \left(\frac{1}{r} \frac{\partial v_r}{\partial \theta} + \frac{\partial v_\theta}{\partial r} - \frac{v_\theta}{r} \right) \ , \tag{III.18}$$

$$\hat{\boldsymbol{n}} = \hat{\boldsymbol{r}} \ , \tag{III.19}$$

$$\hat{\boldsymbol{t}} = \hat{\boldsymbol{\theta}} \ . \tag{III.20}$$

And then, if we consider that the radius R is large such that we can ignore the v_θ/R term :

$$\underline{\underline{\sigma}}^{\text{sol}} \hat{\boldsymbol{r}} \cdot \hat{\boldsymbol{\theta}} = \eta \left(\frac{\partial v_\theta}{\partial r} \right) = \eta\omega \ . \tag{III.21}$$

We must include additional information to calculate the stress in the gel, as we are not explicitly modeling its velocity variation across the layer of width h. A phenomenological way, which recapitulates our previous observations at the boundary layer, is to consider that the gel velocity is maximum right at the cortex, and decreases linearly until reaching the cytosol (see Fig. III.1). In a scaling fashion, such a stress will be given by :

$$\underline{\underline{\sigma}}^{\text{gel}} \hat{\boldsymbol{n}} \cdot \hat{\boldsymbol{t}} = \pm \eta_c \frac{u}{h} \ , \tag{III.22}$$

where the sign is positive (negative) if $\hat{\boldsymbol{n}}$ points to (away from) the gel layer.

III.2 Uniformly bound myosin : mechanochemical instability

When myosin is bound uniformly in the cortex, for example when placing a single nucleus in the center of a ring, no myosin gradients along it exist, and as such, no flows are produced. Yet, this state could be linearly unstable, and flows could be produced in periodic patterns due to such instability. Two opposing forces drive this process. On the one hand, when a region of higher bound myosin concentration is produced, the gel flow will point towards this region, driving further accumulation of myosin, increasing the flow strength in a positive feedback loop. The non-linear terms we have neglected in the bound myosin activation and cortical compressibility should limit this process in the long run. On the other hand, concentrations drop more rapidly in more concentrated regions due to diffusion and myosin unbinding. The balance between these two opposing effects can be systematically studied in a 1d periodic system, with the instability depending on the characteristics of the actomyosin activation function [136]. Similar studies have been performed in active cortical networks, where different mechanochemical feedbacks bring these patterns to life [137], [138]. More broadly, previous work has considered hydrochemical pattern formation in both experimental and theoretical settings, finding the production of localized structures due to flow and matter patterning [139]. In this case, we will study how these actomyosin instabilities drive flows in the bulk, and the impact of the geometry in forming and selecting these patterns. We will treat this problem using the standard tools of linear stability analysis.

III.2.1 Infinite cortical strip

Consider an infinite cortical strip parallel to the x axis and located at $y = 0$. The region $y > 0$ is completely filled by cytosol. Let us start from a completely homogeneous situation, with $u = 0$ and $\rho_b = \rho_b^0 = k_b/k_u$. We may then introduce a perturbation such that :

$$u = \delta u e^{\sigma t + iqx} \ , \tag{III.23}$$

$$\rho_b = \rho_b^0 + \delta\rho_b e^{\sigma t + iqx} \ . \tag{III.24}$$

We may rescale time by the typical bound time of myosin, $t \to k_u^{-1} t$. We can also rescale distances by the hydrodynamical length, such that $x \to \sqrt{\frac{\eta_c}{\gamma}} x$. Then, the dispersion relation can be expressed as (see Appendix) :

$$\sigma(q) = \Pi_\alpha^2 \frac{q^2}{1+q^2} - \left(q^2 \Pi_D^2 + 1\right) \ , \tag{III.25}$$

where $\Pi_\alpha = \sqrt{\frac{\alpha \rho_b^0}{\eta_c k_u}}$ is the ratio between active and viscous forces, and $\Pi_D = \sqrt{\frac{\gamma}{\eta_c}}\sqrt{\frac{D_b}{k_u}}$ is the ratio between the diffusion length of bound myosin and the hydrodynamical length. The behavior of this function for different parameter values is illustrated in Fig. III.2a. We can see that this system cannot excite zero modes ($\sigma(q \to 0) < 0$), nor unphysical modes ($\sigma(q \to \infty) < 0$). By analyzing the extrema of σ, we can determine the stability phase diagram as a function of Π_α and Π_D (see Fig. III.2b). For $\Pi_\alpha > \Pi_D$, the maxima are located at a location $|q^*| > 0$, and if $(\Pi_\alpha - \Pi_D)^2 > 1$, $\sigma(q^*) > 0$, resulting in pattern formation. This

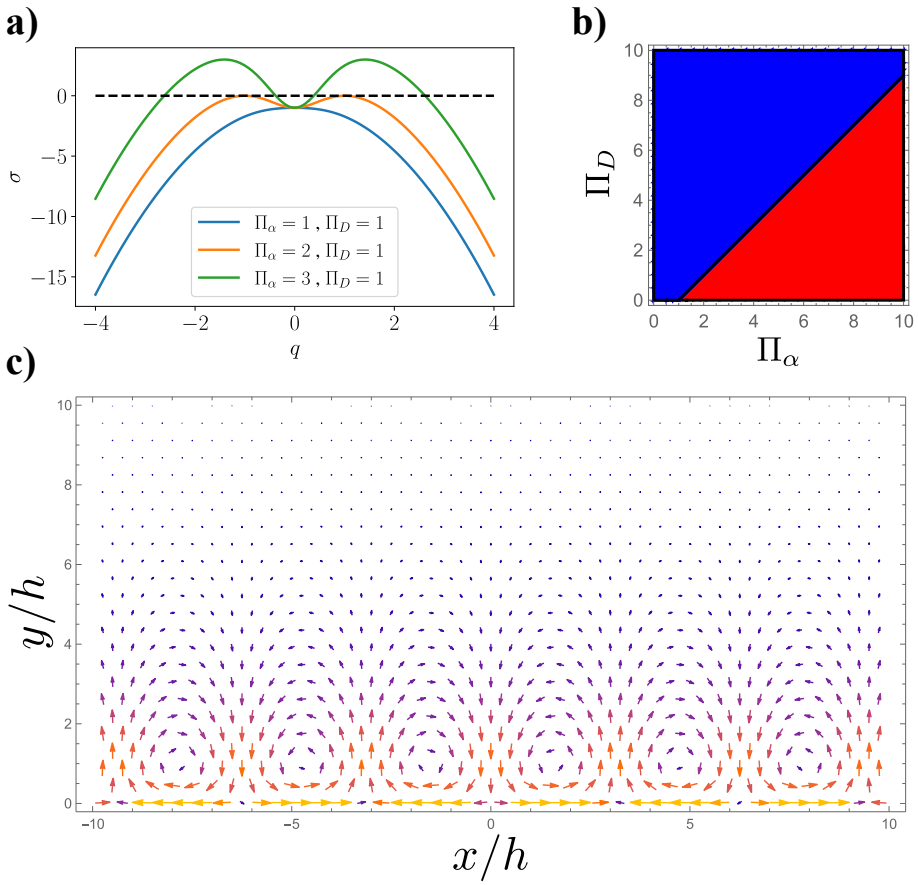

FIG. III.2 *a) Nondimensional dispersion relation of actomyosin pattern formation in a cortical strip as a function of the nondimensional wavenumber q for three different parameter combinations. b) Stability phase diagram for the cortical strip as a function of the two nondimensional parameters. Blue : Stable, Red : Unstable. c) Vector plot of the induced cytoplasmic flows in the half-space $y > 0$ due to the cortical instability with $q^* = h^{-1}$.*

has a very clear physical interpretation, the actomyosin contractility must be large enough such that it can overcome the viscosity and the tendency of myosin to homogenize due to diffusion.

We can determine an approximate flow profile in the cytosol by considering the contribution of the fastest-growing mode only. This would mean that we are at a timescale that is large in comparison to the evolution of the modes, yet small in comparison with the nonlinear effects, i.e. saturation, that could perturb growth. Calculating the stream function of the flows, recovering dimensional units yields (see Appendix) :

$$\psi = \frac{\eta_c}{\eta}\frac{u_0}{h}\cos(q^* x)\,\frac{y}{2q^*}e^{-q^* y}\ , \tag{III.26}$$

where u_0 is the amplitude of the cortical flows, and q^* is the fastest growing mode. Fig. III.2c shows the typical profile of the resulting flows. We can see that the instability produces regular domains separated by a distance $\frac{2\pi}{q^*}$, and there is an exponential decay of the flow

strength going away from the cortical strip.

III.2.2 Cortical ring

Next, consider a circular domain of cytosol of radius R, with an active gel ring at the boundary. Now, instead of a continuous wavenumber q, we have a set of integers n that produce patterns with different symmetries. By introducing the same time rescaling $t \to k_u^{-1} t$ as before, and defining the rescaled variable $q = \sqrt{\frac{\eta_c}{\eta_c + R^2\gamma}}\, n$, the nondimensional dispersion relation reads (see Appendix) :

$$\sigma(q) = \Pi_\alpha^2 \frac{q^2}{1+q^2} - \left(\left(\Pi_D^2 + \Pi_R^2\right) q^2 + \Pi_R^2 + 1\right) \ , \tag{III.27}$$

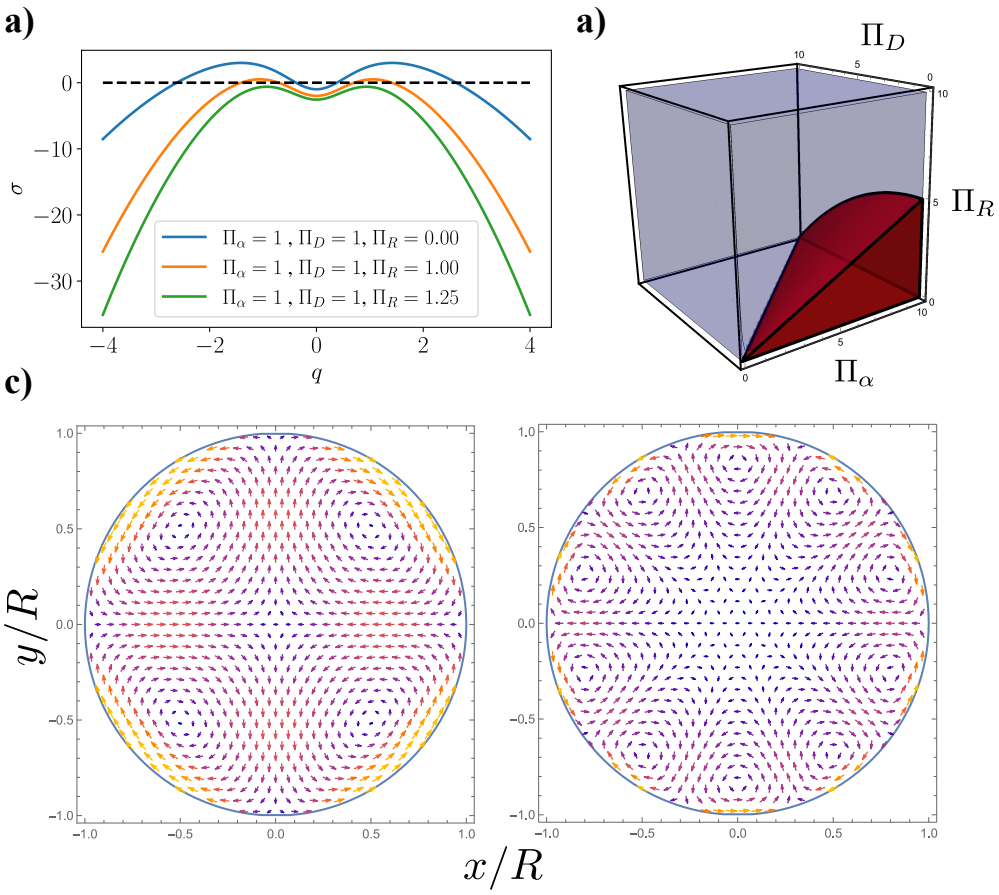

FIG. III.3 *a) Nondimensional dispersion relation of actomyosin pattern formation in a cortical ring as a function of the normalized wavenumber q for three different parameter combinations. b) Stability phase diagram for the cortical ring as a function of the three nondimensional parameters. Blue : Stable, Red : Unstable. c) Vector plot of the induced cytoplasmic flows in a circular arena due to the cortical instability. Left : $n^* = 2$, Right : $n^* = 5$.*

where $\Pi_R = \frac{1}{R}\sqrt{\frac{D_b}{ku}}$ is the ratio between the diffusion length of bound myosin to the radius of the ring. The behavior of this function is illustrated by Fig. III.3a. In this case, we can show that when $\Pi_\alpha^2 > \Pi_D^2 + \Pi_R^2$, the maxima are located at $|q^*| > 0$, and if $\Pi_\alpha^2 + \Pi_D^2 - 2\Pi_\alpha\sqrt{\Pi_D^2 + \Pi_R^2} > 1$, $\sigma(q^*) > 0$, resulting in pattern formation (see Fig. III.3b).

In this case, the curvature makes the system more stable. In a system where these cytoplasmic flows drive the transport of material through tubes, considering the active nature of the driving force, it could be beneficial to make tubes narrow enough such that they do not develop this instability.

We can determine the approximate shape of the flows by using the same saddle point approximation as in the strip case. Then, in dimensional units (see Appendix) :

$$\psi = \frac{1}{4(n^*+1)}\frac{\eta_c}{\eta}\frac{u_0}{h}\left(\frac{r}{R}\right)^{n^*}\left(r^2 - R^2\right)\cos(n^*\theta)\ , \tag{III.28}$$

where u_0 is the amplitude of the cortical flows, and n^* is the fastest growing mode. Fig. III.3c shows the typical profile of the resulting flows for $n^* = 2$ and $n^* = 5$, note that due to the harmonic vorticity, the velocity decay closer to the center is gets faster as n^* increases. As a final intuitive remark connecting this case to the previous one, we can see that the case $R \to \infty$, rescaling $n = qR$, reduces this situation to the case of the infinite cortical strip.

III.3 Nuclear-induced flows in different geometries

To get tractable analytical results, we will consider that the binding-unbinding rates are very fast in comparison to the variations in PP1 concentration due to the oscillations in the Cdk1 clock and the motion of the nuclei. Our chosen myosin binding/unbinding rates in the previous chapter support this assumption, with the cell cycle lasting eight minutes, and binding/unbinding timescales on the order of seconds (see Table A.1). We will ignore the intermediate field that introduces a delay between PP1 and myosin (see Eq II.26) as it is not substantial to reproduce the flows. We will also ignore the non-linear effects of myosin transport due to the cortical flows.

In this adiabatic setting, the concentration of bound myosin is proportional to the amount of PP1 at a given location in the cortex. This establishes a direct link between the location of the nuclei and the driving forces of the gel flows. Furthermore, the response of the system is linear in the concentration of bound myosin. Hence, its behavior for multiple nuclei can be easily found after having solved the single nucleus case.

Depending on the cortical geometry and the position of the nuclei, these flows are able to propel them in particular directions. A very simple example that illustrates this fact is the case of a nucleus inside of a V-shaped cortical aperture. As we can observe in Fig. III.4, the bound myosin maxima are displaced in the x coordinate with respect to the x position of the nucleus, which can be determined geometrically :

$$\epsilon = x\sin^2(\alpha/2)\ , \tag{III.29}$$

where x is the distance of the nucleus from the corner. hence the nucleus will be propelled away from the corner.

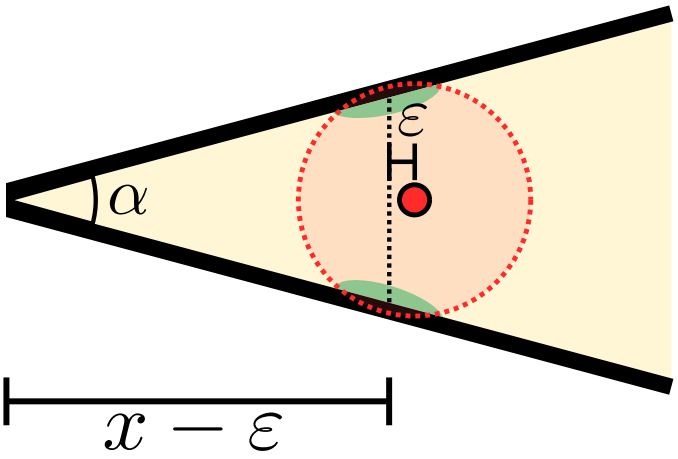

Fig. III.4 *Sketch showing an embryo (red) in a triangular-shaped cytoplasmic region (light yellow). Due to the geometry, the bound myosin distribution (green) is displaced with respect to the center of the PP1 distribution by a length ε, which leads to the propulsion of the nucleus.*

This general fact illustrates that nuclei tend to migrate from narrower regions to broader regions.

III.3.1 Infinite cortical strip

We will start by considering an infinite cortical strip parallel to the y axis, located at $x = 0$. The cytosol fills the $x > 0$ region, and we have a single nucleus at (x_i, y_i). A standard tool to solve this problem considers calculating the Fourier transform of our relevant functions in the y coordinate. However, even in this simple setting, expressing the inverse transforms in a closed form is extremely challenging. To go over this roadblock, we will perform two approximations. First, we will consider a Gaussian approximation for the bound myosin distribution at the cortex, assuming that the distance between the nucleus and the cortex is larger than the PP1 decay length λ. In such a case, and considering $y_i = 0$ for simplicity, we can approximate the PP1 cloud in space as :

$$\rho_p = g(t)e^{-\sqrt{x_i^2+y^2}/\lambda} \approx g(t)e^{-x_i/\lambda}e^{-\frac{y^2}{2x_i\lambda}} \ , \tag{III.30}$$

where $g(t)$ is the PP1 activation function. As a result, the Fourier transforms of the relevant variables will be some Gaussian function multiplied by another function. This will yield different functions that decay exponentially at infinity, and present a given number of symmetric or antisymmetric spikes close to $k = 0$. If our hydrodynamical lengths are such that these spikes decay rapidly over space, these resulting functions can be approximated by a sum of Gaussian functions with different standard deviations, which then can be readily brought back to x space (see Appendix for detailed calculations).

From Fig. III.5a, we can see that the flow profile partitions the space into two clear regions. In the central cone, the velocity points away from the strip. Outside this cone, the

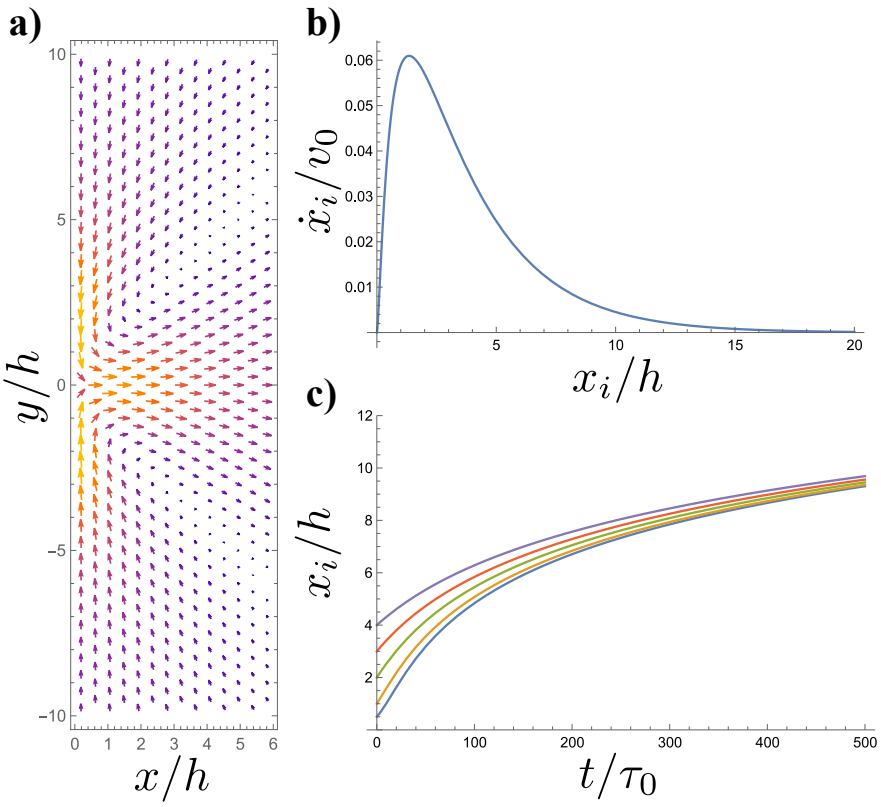

FIG. III.5 *a) Vector plot of the flows induced due to the presence of a single nucleus at $x_i/h = 2$ next to a cortical wall located at $x = 0$. b) Flow velocity at the position of a nucleus next to a cortical wall at $x = 0$. c) Evolution of the position of a single nucleus as a function of time resulting from the distance-dependent cytoplasmic flow strength shown in b). 5 different initial conditions are displayed. Timescale $\tau_0 = \eta/(h\alpha)$ and typical velocity $v_0 = h/\tau_0$.*

velocity profile has a strong horizontal component that will bring a tracer back to the central cone.

The dependence of the strength of the pushing as a function of the distance is clearly illustrated by Fig. III.5b. Moreover, there is a characteristic distance from the wall beyond which the velocity is negligible. Fig. III.5c illustrates that beyond this point, the distance of different nuclei to the wall with different initial conditions will collapse. This is a consequence of velocity control due to PP1. As another remark, the initial quasi-linear scaling hints at that it could be easy for a probe to measure its distance from the wall just by analyzing the strength of the flows.

Approximate solutions for more complicated geometries can be obtained by adding the contributions of multiple infinite strips, assuming that the distances between them are larger than the decay length of the sol flows that they induce, and that the strips may only intersect in regions beyond the decay length of the gel flows.

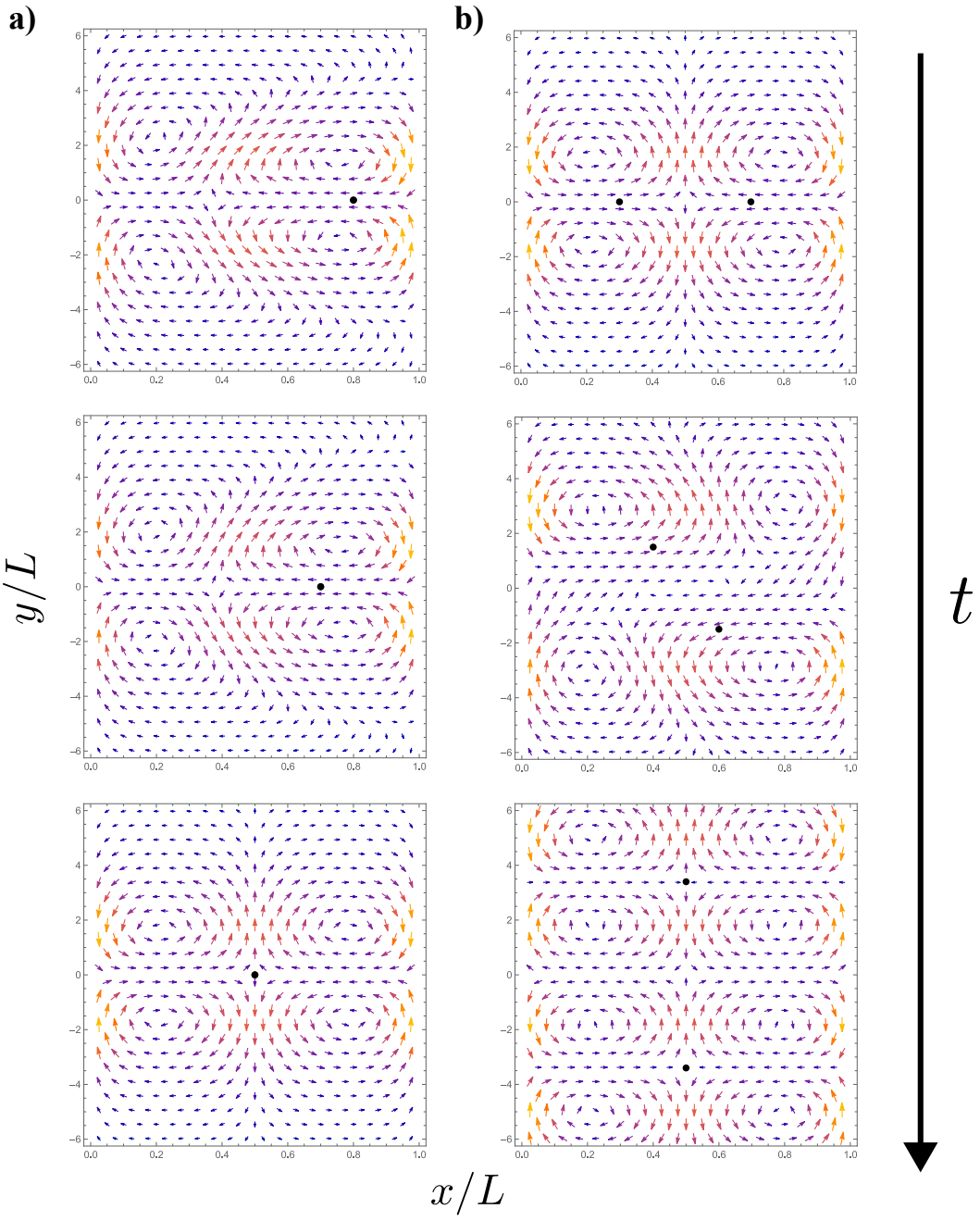

FIG. III.6 *a) Vector plots of the induced flow in a channel parallel to the y axis due to the presence of a single nucleus at varying distances from the right cortical strip. The pushing effect from the flows leads to centering. b) Vector plots of the induced flow in a channel parallel to the y axis due to the presence of two nuclei that start in a configuration perpendicular to the channel. Any small perturbation leads to hydrodynamical buckling, and in the end, nuclei get to a preferred separation distance. Channel width : L.*

III.3.2 Parallel infinite cortical strips

The case of two parallel strips can be approximated by using the solution obtained before and superposing the contributions of two strips next to each other. But if the distance between the two is smaller than the characteristic decay length of the sol flows induced by the gel entrainment, the approximation will become very poor. Hence, to study narrow geometries, it will be useful to consider a more accurate solution. This parallel cortical strips situation approximates the mid-section of a tube.

The relevant calculations reduce to using the same Gaussian approximation introduced in Eq. III.30 in both strips, and then calculating the flows inside using analogous Fourier transform techniques to the single strip case (see Appendix for details). As illustrated by Fig. III.6a, if the nucleus is not placed at the same distance from the two strips, the shape of the flow will move the nucleus closer to the center.

Because stream functions are additive, our calculations can already account for multiple nuclei. We can see that the induced flow tends to spread the nuclei in the bulk, such that they are separated by a characteristic distance. This is interesting because it shows that microtubules are not strictly necessary to spread the nuclei apart when under the influence of actomyosin-driven flows. A very clear representation of this is shown in Fig. III.6b. When the two nuclei are placed in a line that is perpendicular to the strips, the induced flows will bring them closer to the center. But this situation is actually unstable. Any small perturbation to this configuration will make the nuclei spread apart in the y axis as they move toward the center, resembling the process of mechanical buckling.

When multiple nuclei are placed together, we can see from Fig. III.7 that the strongest flows are produced at the edges of the distribution. This is completely natural, considering that the bound myosin distribution is less uniform at the edges. This means that the nuclear spreading is not completely uniform, it is driven by the external nuclei, which when displaced

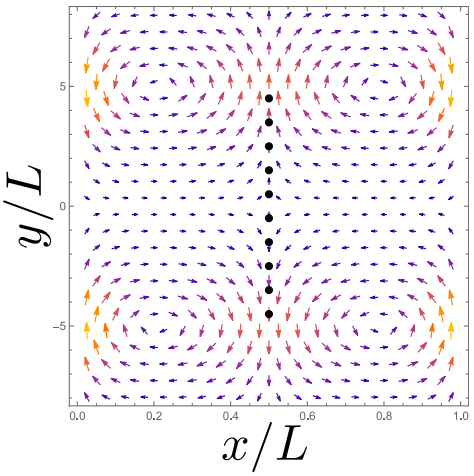

FIG. III.7 *Vector plot of the induced flows in a channel of width L parallel to the y axis due to the presence of a line of nuclei. PP1 gradients produce the strongest flows at the edges of the distribution.*

trigger the next shell to move and so on.

These results suggest that when having a nuclear distribution, the flows will tend to concentrate the distribution along the axis lying in between the two strips. If the strips are really infinite, then the distribution will become delta-distributed around this line. Otherwise, the size of the system will set the aspect ratio of the final distribution.

III.3.3 Circular arena : discrete nuclear distribution

Next, we consider the case of a nucleus in a circular cytosol domain of radius R, surrounded by an active gel ring. When the nucleus is exactly at the center of this structure, myosin binds uniformly around the cortex and no flows are produced. As we have shown in the previous section, this could induce the production of flow patterns due to the advection-driven instability, yet this effect is not captured when ignoring the gel-driven myosin transport.

As in the previous cases, we can expand the ρ_b function assuming that the nucleus is far from the cortex. When the nucleus is off-center, the PP1 cloud is displaced and flows arise from these gradients. Given that the vorticity is a harmonic function, it can be naturally expressed as a superposition of circular harmonics, i.e. vorticity multipoles. At the lowest order, our results allow us to find the contribution of the vorticity dipole and quadrupole

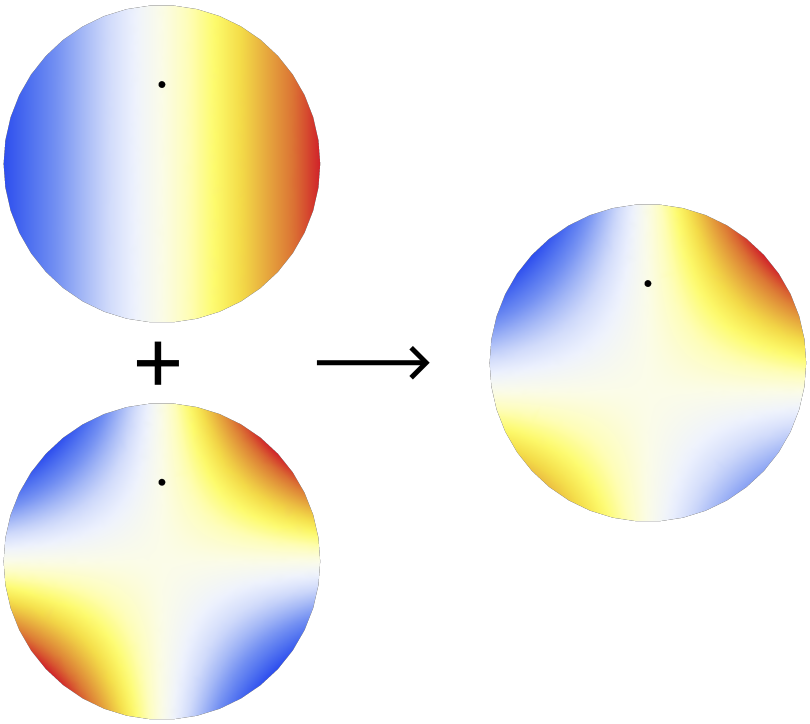

Fig. III.8 *Flow vorticity induced due to the PP1 activation of a single nucleus in a circular arena. The main components are a dipole and a quadrupole. Vorticity color-coded from blue (Negative) to red (Positive).*

(see Fig. III.8). They are oriented such that the nucleus is located in a line of zero vorticity, with the signs such that the flows redirect the nucleus to the center. Overall, the addition of the two vortices has the shape of a quadrupole that is displaced from the center, which is in qualitative agreement with experimental observations and our full model, even if the real embryo geometry is elongated.

Using an analogous procedure to the one explained for the other geometries, we can calculate the stream function for a single nucleus, and from there reconstruct the velocity profile everywhere in the domain, and in particular, at the position of the nucleus. At the lowest order, the evolution of the distance of the nucleus to the origin satisfies the following dynamical equation (see Appendix) :

$$\frac{\mathrm{d}r_i}{\mathrm{d}t} = -g(t)\frac{1}{\tau}r_i \ , \tag{III.31}$$

where $g(t)$ is the cell cycle oscillator and :

$$\frac{1}{\tau} = \frac{1}{8}\frac{1}{h}\frac{\alpha}{\eta}\frac{1}{10+7R^2\kappa_c^2+R^4\kappa_c^4}Re^{-\frac{R}{\lambda}}\left(5+R^2\kappa_c^2\right)\frac{R}{\lambda} \ , \tag{III.32}$$

where $\kappa_c^{-1} = \sqrt{\eta_c/\gamma}$ is the hydrodynamical length.

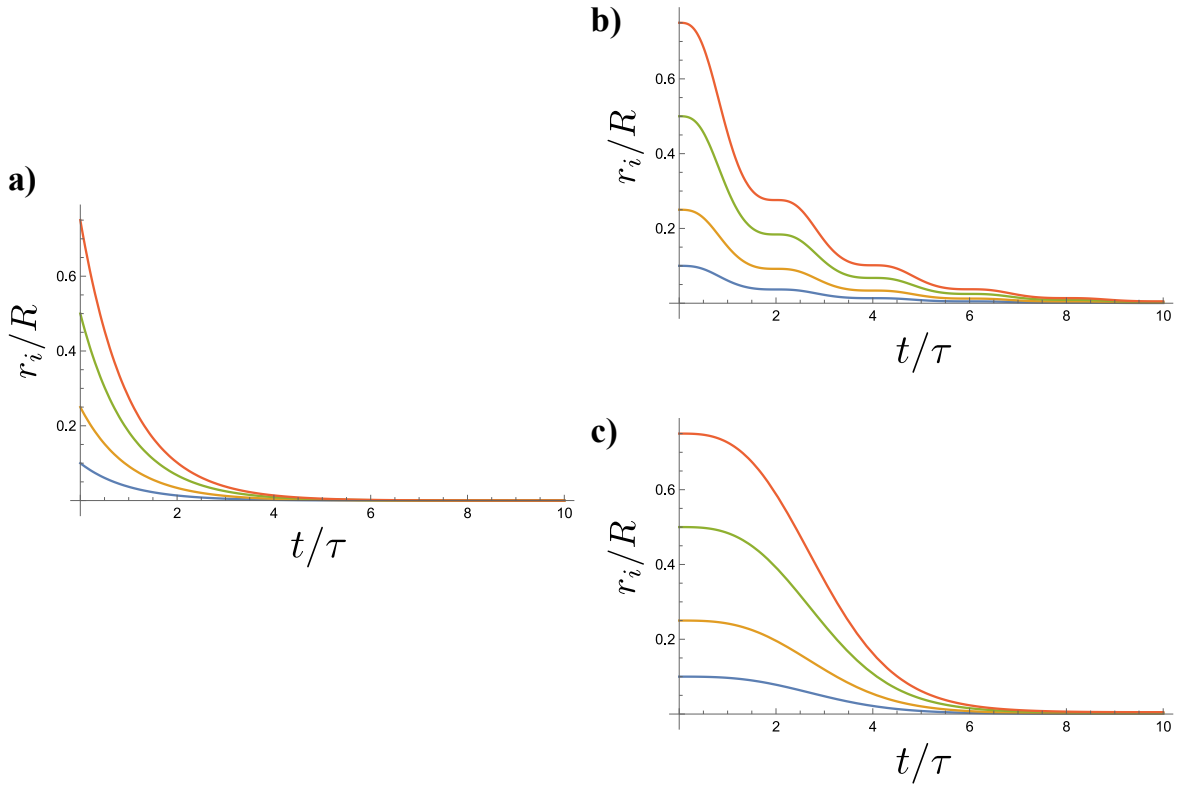

FIG. III.9 ***Centering in a circular arena follows exponential dynamics*** *a) Plot of solution III.33 for four different initial conditions. b,c) Plot of solution III.34 for four different initial conditions.* $T = 2\tau$ *and* $T = 10\tau$ *respectively.*

Assuming $g(t)$ to be equal to one, i.e max PP1 activity, we recover exponential decay :

$$r_i(t) = r_i(0)e^{-\frac{t}{\tau}} \ . \tag{III.33}$$

Solutions to this equation for different initial conditions are shown in Fig. III.9a. A more realistic result considers the periodic oscillations of the cell cycle. For instance, by considering $g(t) = \sin^2(\pi t/T)$:

$$r_i(t) = r_i(0)e^{-\frac{t}{2\tau}} e^{\frac{T\sin(2\pi t/T)}{4\pi\tau}} \ , \tag{III.34}$$

where notably, due to the non-constant PP1 activation, the characteristic centering time is doubled. This would depend, in general, on the time average of the function $g(t)$. Figs. III.9b,c show the behavior of this solution for different oscillatory periods of PP1.

Now, let us focus on nuclear positioning when more than one nucleus is present. In our approximation, the cytosol vorticity is the linear superposition of dipoles and quadruples. They are mathematically represented as $\sin(\theta - \theta_i)$ and $\sin(2(\theta - \theta_i))$ terms, where θ_i is the angular position of nucleus i in the domain (see Appendix). When two nuclei are present, we can see from Fig. III.10a and from our equations (see Appendix) that the flows will drive them to spread apart with a separation angle $\Delta\theta = \pi$, achieving a maximally symmetric state. If both particles are equidistant from the center, then we should only look at the $\sin(\theta - \theta_i)$ and $\sin(2(\theta - \theta_i))$ terms. It is not hard to see that for two particles with opposite angles, the first term annihilates, and hence the leading residual flows have a $\sin(2\theta)$ shape, i.e. 4 vortices. We must remember that we have started from an expansion of the exponential in the ρ_b function, hence higher orders of $\sin(n(\theta - \theta_i))$ are ought to exist in the full problem.

If we consider a triangular distribution where one of the vertices is closer to the cortex, we can see that the flows will bring this nucleus closer to the center, while the other ones will be pushed apart (see Fig. III.10b). In the end, they will reach an equilateral triangle distribution. In this case, the $\Delta\theta = 2\pi/3$ angular separation between particles implies that the $\sin(\theta)$ and $\sin(2\theta)$ terms vanish, hence the leading residual flows have a higher symmetry. A rectangular distribution with unequal width and length will converge to a square distribution, as shown in Fig. III.10c, and the $\Delta\theta = \pi/4$ angular separation between particles will annihilate the $\sin(\theta)$ and $\sin(2\theta)$ terms again.

In general, for a centered N-gon nuclear distribution, the leading residual flows will have D_N symmetry, where D is the dihedral group. The argument is very simple ; as shown before a single nucleus will be pushed towards the center of the arena. If we have N nuclei arranged symmetrically around the center, each one of them will be pushed towards the center with the same strength. However, the fluid is incompressible, which means that between regions pushing inwards there should be regions that push outwards. Hence, there will be $2N$ vortices, N positive and N negative, and the whole flow field will have D_N symmetry. This has important implications. Because the vorticity is harmonic, the strength of the flow decreases and becomes more localized towards the boundary the more vortices there are. Hence, the residual flows become less relevant as more nuclei are put in. Finally, in the $N \to \infty$ limit, the distribution is circular and no gradients of ρ_b exist, hence the residual flows are exactly zero.

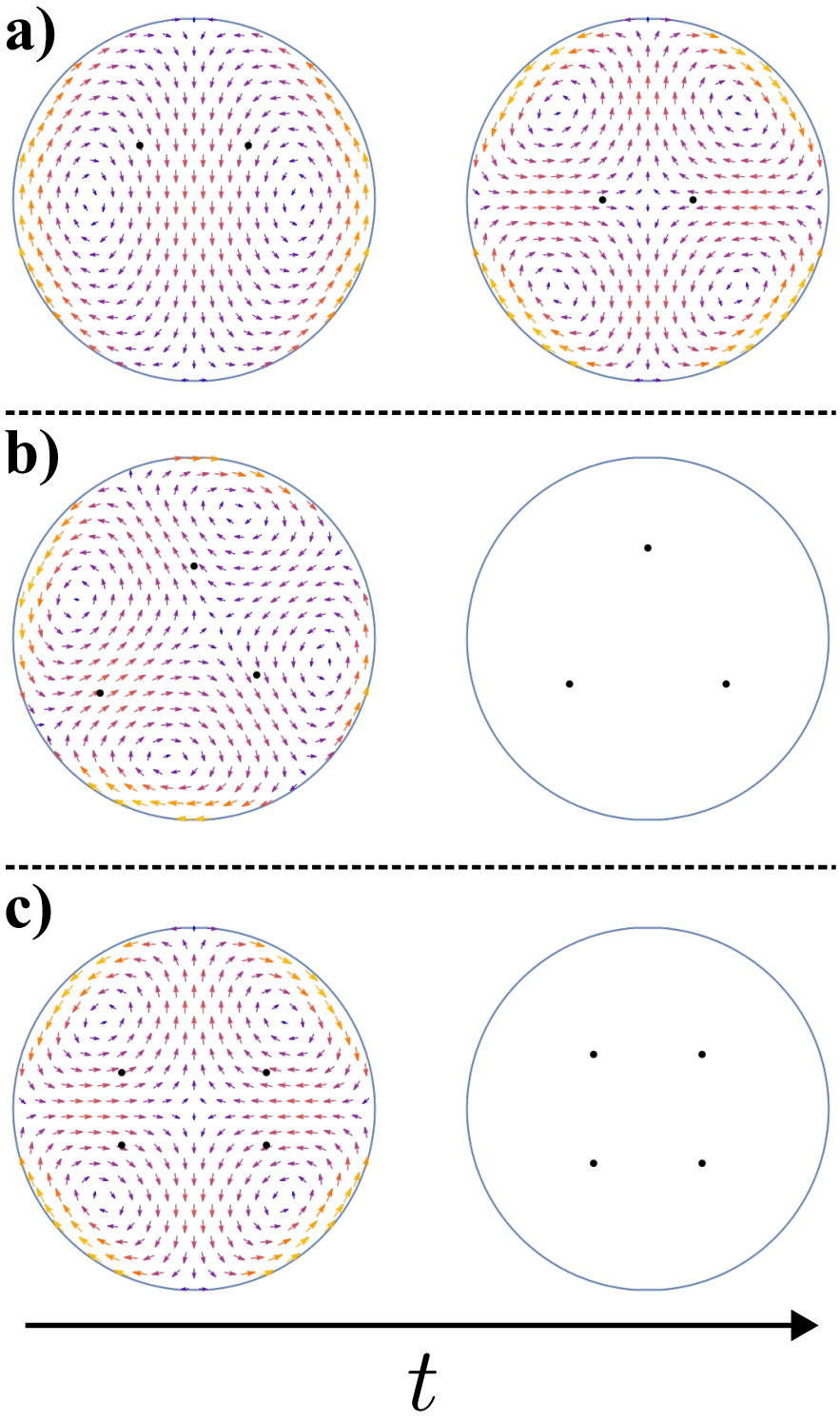

FIG. III.10 *a,b,c) Initial and final distribution of nuclei for a two,three, and four-particle distribution respectively. Residual flows in the three and four-particle cases cannot be calculated with our approximation.*

III.3.4 Circular arena : arbitrary continuous nuclear distribution

We have already determined that there exists a link between the geometry of the distribution of nuclei and the geometry of the flows in the circular arena. We have argued that distributions tend to become more symmetric over time, however, this timescale is not completely obvious, and dealing with generic angles and distances between particles quickly leads to equations that are intractable with simple analytical methods. Hence, it would be even more insightful to work with continuous distributions to see how the properties of the distribution relate to the properties of the flow and its temporal evolution. Let us define a nuclear distribution ρ_n by performing a coarse-grained procedure on the discrete positions of the nuclei :

$$\rho_n = \left\langle \sum_i \delta\left(\boldsymbol{r} - \boldsymbol{r}_i\right) \right\rangle_A \ , \tag{III.35}$$

where $\boldsymbol{r}_i$ denotes the position of the i-th nucleus and the average is performed in a neighborhood of size A around $\boldsymbol{r}$.

This nuclear distribution will, in general, evolve with the following equation :

$$\frac{\partial \rho_n}{\partial t} + \nabla \cdot \left(\boldsymbol{v}_n \rho_n - D_n \nabla \rho_n\right) = G_n \ , \tag{III.36}$$

where $\boldsymbol{v}_n$ is the advection velocity of the nuclei, D_n is the nuclei diffusion coefficient, and G_n is a production function that accounts for nuclear division or death.

We will make various simplifying assumptions to disentangle the effect of the flows from the rest of the nuclear biochemistry. Nuclei are large enough such that their diffusive motion can be ignored in the timescales that we are interested in. We will also ignore nuclear division, such that $G_n = 0$. Finally, we will ignore the microtubule-mediated interaction forces, such that the advection velocity is exactly the cytosol velocity. Formally, this could be a problem because depending on the shape of the flows, there could be an unphysical accumulation of nuclear density in localized positions in space. However, the cytosol is incompressible, and if the only thing moving the nuclei is the cytosol, this should not be an issue.

To close this equation, we need to find the cytosol velocity as a function of the nuclear distribution, $\boldsymbol{v}(\rho_n)$. As an intermediate step, we should determine the cortical gel velocity, for which we calculate the bound myosin distribution by integrating the activation kernel over the nuclear distribution :

$$\rho_b = \int g(\boldsymbol{x}', t) e^{-\|\boldsymbol{x}-\boldsymbol{x}'\|/\lambda} \rho_n(\boldsymbol{x}', t) \, \mathrm{d}^d x' \ . \tag{III.37}$$

We formally have everything to determine the evolution of an arbitrary nuclear density. However, it will be insightful to study the evolution of the moments of the distribution, as the two first moments will already give plenty of information about where the distribution is moving to, and how much is its spread. We can calculate the expected value of any observable by integrating over the nuclear distribution, and in particular, we can consider the moments of the distribution. We can show (see Appendix) that the evolution of the center of mass of the distribution satisfies :

$$\frac{\mathrm{d}}{\mathrm{d}t} \langle \boldsymbol{x} \rangle = -g(t) \chi_1 \langle \boldsymbol{x} \rangle \ , \tag{III.38}$$

where $\chi_1 = 1/\tau$ is the inverse timescale of decay in the discrete case that was previously defined in Eq. III.3.3. On the other hand, the difference between the spread in the x and y directions satisfies :

$$\frac{\mathrm{d}}{\mathrm{d}t}\left\langle x^2 - y^2 \right\rangle = -4g(t)\chi_2 \left\langle x^2 + y^2 \right\rangle \left\langle x^2 - y^2 \right\rangle \ , \tag{III.39}$$

where :

$$\chi_2 = \frac{1}{12}\frac{1}{h}\frac{\alpha}{\eta}\frac{1}{10 + 7R^2\kappa_c^2 + R^4\kappa_c^4} Re^{-\frac{R}{\lambda}} \left(2 + R^2\kappa_c^2\right) \frac{R}{\lambda}\left(\frac{R}{\lambda} + 1\right) \ . \tag{III.40}$$

From the evolution of the different moments of the distribution, we can see that the distribution will tend to center and homogenize its spread in the x and y directions, becoming rotationally symmetric. We can also see that the distribution homogenizes its spread faster than its relocation to the center. As a final remark, just like explained before, due to the incompressibility of the fluid, the flows stop when perfect symmetry is achieved.

III.4 Discussion

Many different organisms rely on cytoplasmic flows to grow and transport cargo. Hence, the flow strength and geometry are determinants to achieve these tasks correctly. Centering has been of particular research relevance, not only in the context of flows [80], [140], but also in actomyosin networks [141], [142]. Here, we propose that this mechanism is generic, with general physical principles allowing us to predict the centering of arbitrary nuclear distributions and their evolution timescales.

Our pattern formation setting was reduced to the linear case. It would be interesting to study the nonlinear effects perturbatively, hence getting a sense of how the patterns get sharper over time, and how does saturation affect each mode depending of their wavenumber.

The general principles uncovered by our simplified model will allow for a better analysis of structures that rely on actomyosin deformations, and could serve as a guiding tool to design new materials. In particular, we have not explored yet the possibility of modulating the actomyosin binding function in space and time. This function would satisfy its own continuity-like equation, and as such there could very well be a feedback between the nuclear positioning or the flow strengths on this function. In turn, this could allow for the propagation of mechanical or “activation” waves, and produce symmetry-breaking flows. In the same way that we have studied pattern formation in the cortical layer leading to bulk flows, there could be the same type of instabilities or even limit cycles if appropriate feedback terms are considered.

More generally, this kind of system can be put in the context of active matter models. The prototypical picture of the Vicsek model [143], later generalized in the continuum [144], considers the self-organized behavior of systems of aligning polar particles. Recently, it has been found that systems where forces are mediated by hydrodynamical interactions can display rotational [145] or translational [146] order. In this context, this mechanism of

boundary-driven flows could be of interest to study the collective properties of these particles in different geometries, and effective particle-particle interactions arising from this mechanochemical coupling could be determined.

A further question is the influence of temperature gradients in the flows. Myosin binding and actin contractions, being processes driven by chemical reactions, should depend on temperature, and we could write an Arrhenius-type dependency as we have done for the other chemical equations. The binding of myosin will no longer be centered around the nucleus, but rather skewed towards the region that is at a higher temperature. As a result, the nucleus will not be at the stagnation point of the flow field, and it will be pushed towards the cold region. Different living organisms have been shown to perform positive or negative thermotaxis [147]-[149]. In the same way, because the cell cycle biochemistry influences the cortical instabilities, tuning the temperature could be a way to transition from a homogeneous situation to triggering an instability and producing flows.

These results could be interesting in the context of flows in tube networks, arising in the context of *Physarum* [68], bacterial aggregates [150], and mycorrhizal fungi [151]. In the midsection of a tube, these gradients can drive the motion of the nuclei. At a bifurcation point, the proportion of nuclei going one way or the other could be determined and controlled by modulating the temperature gradient in each one of the two. This would allow for tunable material transport, beyond pure geometry, by dynamically adjusting the temperature in different regions of the network.

IV – Slowing down before gastrulation

Como en un acto de telepatía, H y yo miramos simultáneamente el gran reloj que estaba en medio de la plaza y la sorpresa que nos llevamos fue aterradora : el tiempo no avanzaba ni un segundo después de las 4 y 19 minutos de la tarde.

Amigo se escribe con H (María Fernanda Heredia)

(This chapter and corresponding appendix are adapted from a manuscript in preparation by Claudio Hernández-López, Stefano di Talia, and Massimo Vergassola)

IV.1 Motivation & Established facts

IV.1.1 Experimental findings on pre-gastrulating *Drosophila* embryos

Gastrulation in *Drosophila Melanogaster* involves a wide range of processes that break the symmetry of the egg and set the stage for tissue differentiation in its different regions. Some of these processes include the ventral furrow formation that will give rise to the mesoderm of the fly [128], [152], or the production of polarized tissue flows that drive the invagination of the endoderm [153]. Besides an adequate regulation of the mechanics of such processes, they require having finalized cellularization, which is dependent on transcription of the nuclear DNA [59], [60]. We must remember that up to the beginning of cycle 14, there is little transcriptional activity in the syncitium because a short S phase only allows for small transcripts to be produced [61]. Hence, it is fundamental that the nuclei start transcribing their DNA to activate new biochemical pathways that lead to development progression. And then, mechanical forces must be properly induced to deform the epithelium in an expected, reproducible way, and therefore synchrony is essential. This poses a critical challenge because chemical reactions are inherently noisy and the beginning of transcriptional activity may not necessarily be triggered at the same time in different regions of the egg. Diffusion can help to smooth out these inhomogeneities, however with the size of the embryo, 500 µm, in contrast with the diffusion coefficient of typical protein $5\,\mu m\,s^{-1}$ [154], whole-embryo synchrony is not a given. As we will discuss, the key lies in the clever use of regulatory biochemistry.

The nuclei in early Drosophila embryos switch between S and M phases, with the master regulator of the cell cycle, the Cyclin B-Cdk1 dimer, switching between phases of slow growth

(S phase) and fast growth followed by degradation (M phase). The chemical network that regulates this clock is set up in such a way that the reaction-diffusion system governing the Cdk1 concentration in the embryo allows for the propagation of waves [155]. Fig. IV.1a shows a wave of mitotic divisions for cycle 13, and Fig. IV.1b shows the same phenomenon by looking at the concentration of Cdk1. As the duration of the cell cycle increases while the embryo goes through successive cleavage divisions, the speed of these waves decreases (see Fig. IV.1c), and so does the embryo-wide synchrony.

A simplified model of the cell cycle biochemistry was proposed, extracting an effective bistable potential that governs the concentration of active Cdk1 (see Fig. IV.1d). However, in contrast with the embryonic waves in the early development of the frog *Xenopus* [156], the behavior and measured speeds of the mitotic waves in *Drosophila* are not consistent with bistable waves. In particular, the waves are too fast and are not impacted by physically decoupling different regions in the egg. The key to understanding this is to note that as more cyclins are produced over time, the shape of the effective potential governing the activation of Cdk1 changes, in particular losing bistability as the stable low-Cdk1 and unstable fixed points annihilate each other. In the wild-type embryo, this evolution of the effective potential landscape is faster than the relaxation timescale of active Cdk1 back to the fixed point, hence

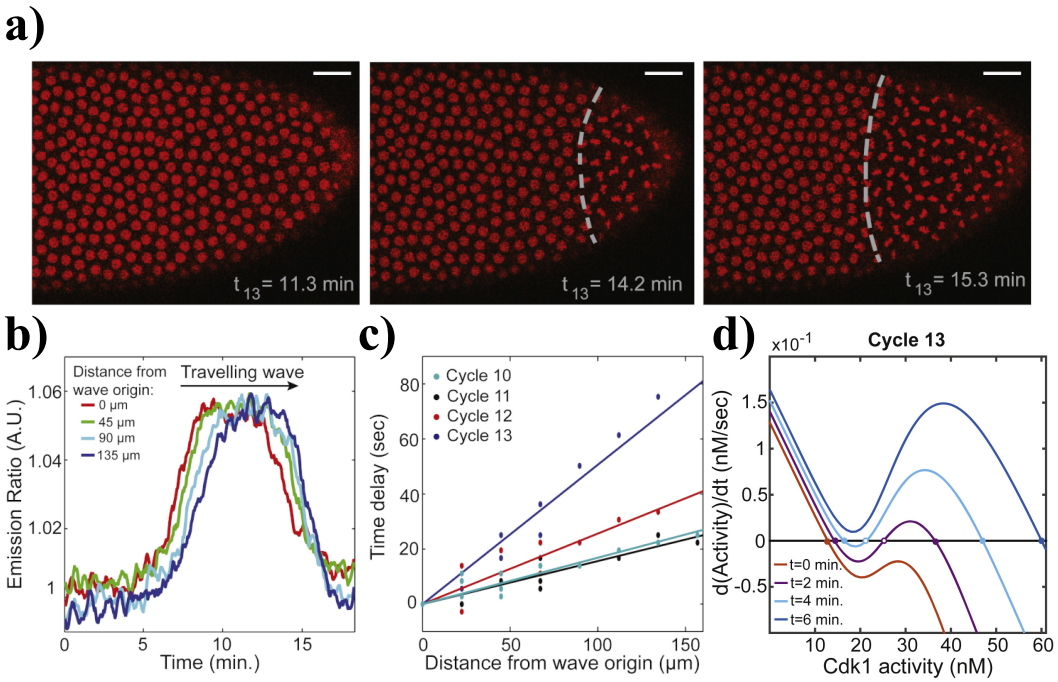

FIG. IV.1 *a) Fluorescent images depicting the spreading of mitotic waves in the embryo of Drosophila Melanogaster during cycle 13. Scale bar :* 10 µm. *b) Activity of the Cdk1 reporter at different positions in the egg during cell cycle 13 showing the propagation of a Cdk1 wave. c) Time delay of the spreading of the wave as a function of position for different cell cycles. d) Effective Cdk1 activation function as a function of its concentration during cycle 13 in a model of the cell cycle biochemistry. Trajectories color-coded from red to blue by increasing time. Panel adapted from [155].*

there is a clear separation between the S and M phase of the cell cycle. During the S phase, the Cdk1 activity stays close to the evolving low-Cdk1 stable fixed point, and diffusion smoothens concentration changes, producing concentration gradients. During the M phase, bistability is lost, and Cdk1 activity spikes as its concentration gets closer to the high Cdk1 fixed point. Activity increases so dramatically that diffusion becomes irrelevant in this phase, i.e. we have a kinematic wave that does not require coupling between different regions of the embryo. The main intuition to keep in mind is that the time delays between different regions are set during S phase, and then M phase merely drives the divisions that occur with these delays [155]. A detailed mathematical analysis of the model successfully reproduced the speed of the waves in wild-type conditions. Furthermore, this model accurately predicted that changes in the feedback mechanisms of the cell cycle can slow down the evolution of the effective potential and recover the slow, bistable mitotic waves [157].

If kinematic waves are responsible for synchronizing mitotic events in *Drosophila* embryos, what is the origin of cell cycle slowing ? One possible lead is noting that nuclear density in the embryo doubles as more divisions are completed. It is a well-established fact that the nuclear to cytoplasmic volume ratio (N/C) is one quantity of interest of cells to control, with departures from an optimal value clear signs of senescence or cancer [158]. In the syncytial stage of the embryo, we are in the presence of a single cell that is duplicating its nuclear volume at each stage. Hence, keeping track of the N/C ratio could be one way to signal cell cycle arrest to start transcription [64]. However, it is clear that nuclei do not have access to all the information in the egg due to the aforementioned slow diffusion of signaling chemical species. Hence, the N/C ratio measurement should be local up to a certain degree, which is perfectly illustrated by genetic experiments.

As explained in Chapter II, achieving a uniform nuclear distribution by cycle 7 requires the cell cycle chemistry to drive cytoplasmic flows. The *shkl* mutant displays an impaired activity of the ligase Cul-5, involved in the regulation of cytoskeletal activity, and more specifically actomyosin contractions. Hence, the cytoplasmic flows in these embryos are significantly reduced. As a consequence, once the nuclei reach the cortex, the nuclear distribution follows a gradient along the anterior-posterior axis, and synchrony is compromised following the production of an extra division patch in the diluted region [65], [91] (see Fig. IV.2a). These results are consistent with the idea that the cell cycle slows down as a function of the nuclear density. However, this sensing seems to be controlled by the density of DNA rather than nuclear density alone. In particular, the duration of nuclear cycle 13 has been shown to scale with the DNA content [64], [159], with detailed experiments showing a quasi-linear behavior [63] (see Fig. IV.2b). Experiments have shown that this scaling is not uniform, the removal/duplication of particular chromosomes amount to different effects, and it has been suggested that this is due to the transcriptional activity of different chromosomes [63]. We will ignore this subtetly for the time being.

Beyond altering the cell cycle length, this mechanism has profound consequences. If the DNA fraction in the embryo is 50% of the WT embryo, then nuclei effectively measure that they are one cell cycle behind what they really are and then one extra division should be triggered. Analogously, if the DNA fraction is 200% of the WT embryo, the nuclei should arrest their cell cycle one division before the WT embryo. This means that somewhere in between 50% and 100% (100% and 200%), there should be some values for which random

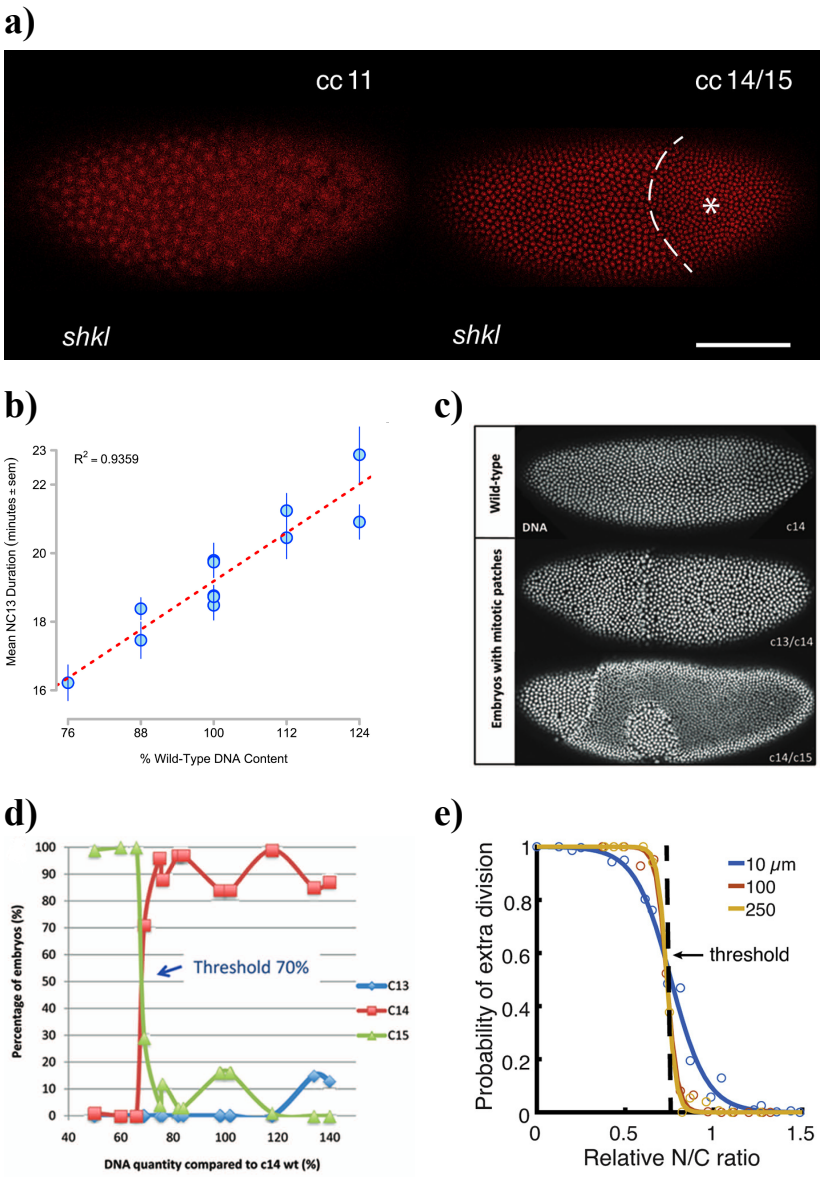

FIG. IV.2 *a) Fluorescent images depicting the shkl embryo mutant. At cell cycle 11, the anterior has a higher density than the posterior side. Later on, the less dense side divides an extra time, producing a patch that has been outlined in white. Scale bar :* 100 µm. *Adapted from [65]. b) Duration of cycle 13 as a function of the DNA content of the embryo. Adapted from [63]. c) Patchy embryo arrested between cycles 13 and 14 for increased DNA quantity mutants, and between cycles 14 and 15 for reduced DNA quantity mutants, compared to a reference wild-type embryo arrested at cycle 14. Adapted from [62]. d) Percentage of embryos that arrest at cell cycle 13 (blue), 14 (red), and 15 (green) for different DNA quantities. Adapted from [62]. e) Measured probability of extra division at different locations in the embryo as a function of the local N/C ratio, averaging over different neighborhood sizes depicted in different colors. Curves collapse at a relative N/C ratio close to 0.7. Adapted from [65].*

fluctuations drive the embryos to either trigger an extra division (arrest a cycle early) or not. Not only is this true, but also the spatial extent of these decisions is not necessarily the whole embryo, with patchy embryos being produced for some fractions of the WT DNA content (see Fig. IV.2c). Fig. IV.2d shows a sharp transition between embryos that arrest at cycle 14 and cycle 15 for a DNA content of $\sim 70\%$, where patchy embryos are observed around this number. These results go hand in hand with careful measurements of the size of the extra division patches in *shkl* embryos. In particular, the probability of undergoing an extra division before arrest at cycle 14 is linked to a local nuclear density in space close to $\sim 70\%$ of the WT cycle 14 density (see Fig. IV.2e).

It has been shown that the N/C ratio controls the slowdown of the cell cycle by inhibiting Chk1 [155]. Yet, the biochemical mechanism that yields this effect has yet to be agreed upon. One possible mechanism is the titration of a given molecular species. Fig. IV.3 sketches such a mechanism, where nuclei compete for importing a particular molecular species that has a regulatory effect. Increasing the nuclear density reduces the available number of molecules that each nucleus can import. Experimental evidence supports that histone H3, which is imported into the nuclei, could be a candidate. In particular, as illustrated in Fig. IV.4a, its concentration modulates the duration of the cell cycle, even triggering an extra division event when it is abundant. Furthermore, as shown in Figs. IV.4b and c, increasing H3 concentrations downregulates Chk1 activity, and the concentration of H3 per-nucleus decreases as the

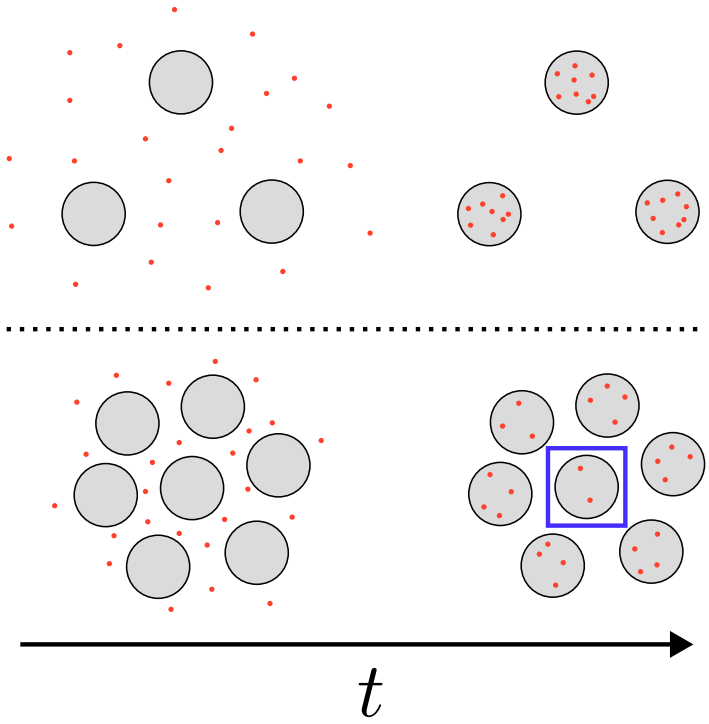

Fig. IV.3 *Sketch depicting how a titration mechanism allows for regulation of biochemical pathways. Top : low nuclear density setting, all the nuclei can import enough titration molecules. Bottom : high nuclear density setting, the central nuclei cannot import enough titration molecules.*

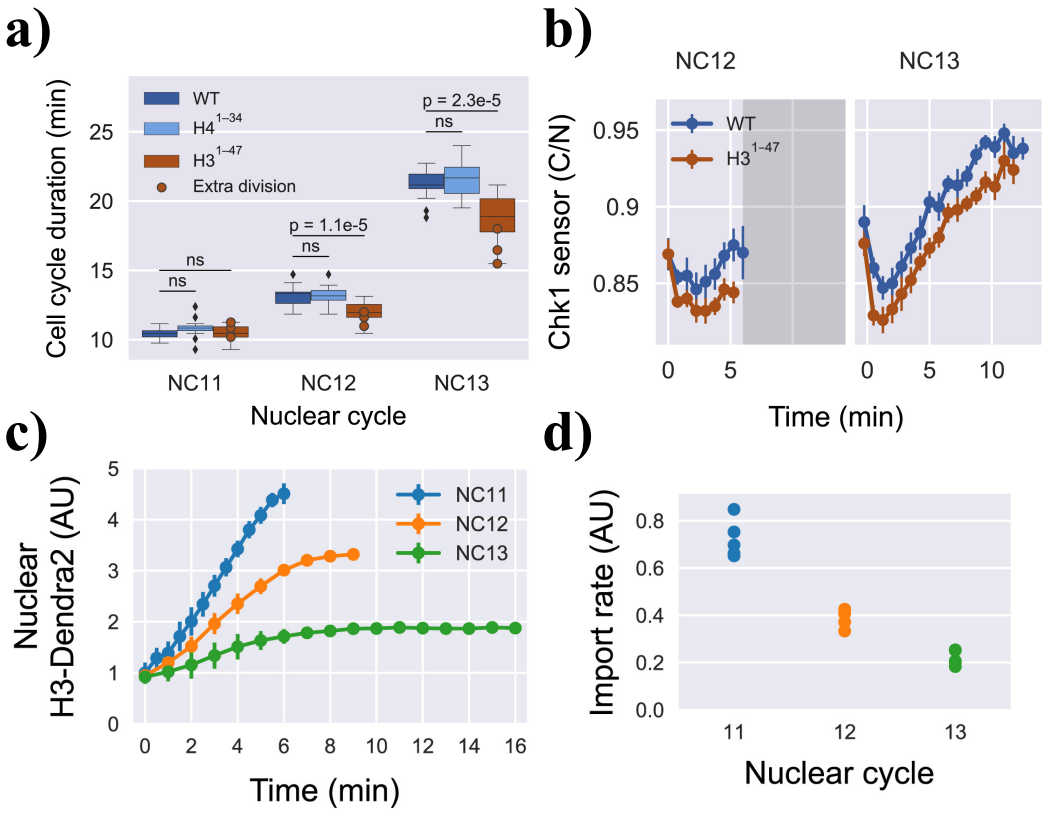

FIG. IV.4 *a) Box plot of duration of cell cycles 11-13 for wild-type embryos, embryos expressing excess of histone H4, and embryos expressing excess of histone H3. The later ones present extra divisions beyond cycle 13. Adapted from [161]. b) Measured Chk1 activity during cell cycles 12 and 13 in a wild-type embryo and an embryo expressing excess of histone H3. Metaphase is greyed out due to the reporter depending on the presence of the nuclear membrane. Adapted from [161]. c) Measured fluorescence level of photoactivated histone H3 in the nuclei as a function of time for cell cycles 11-13. Adapted from [160]. d) Measured single-nucleus import rate of histone H3 for cell cycles 11-13. Adapted from [160].*

cell cycle progresses. The total import rate of this histone in the embryo is constant (see Fig. IV.4d), which means that nuclei do not compete directly to import this histone, rather, they compete to utilize the import machinery [160].

One more element that adds complexity to the challenge at hand is temperature. Beyond the metabolic activity, no internal temperature regulation is present in the egg. The null assumption that we can make is that the reaction rates of the chemical reactions will, as a first approximation, depend on temperature following Arrhenius' equation. These reactions involve a different number of steps and reactants, such that their activation energies are not necessarily the same. To keep a reference of the relevant energy scales, the chemical potential of ATP hydrolysis is $\mu_{\mathrm{ATP}} \approx 30.5\,\mathrm{kJ/mol}$, and at 25°C, $RT \approx 2.5\,\mathrm{kJ/mol}$.

When chemical reactions occur sequentially, their progression is slaved to the slowest reaction, and an effective Arrhenius activation energy can be then obtained [162]. When

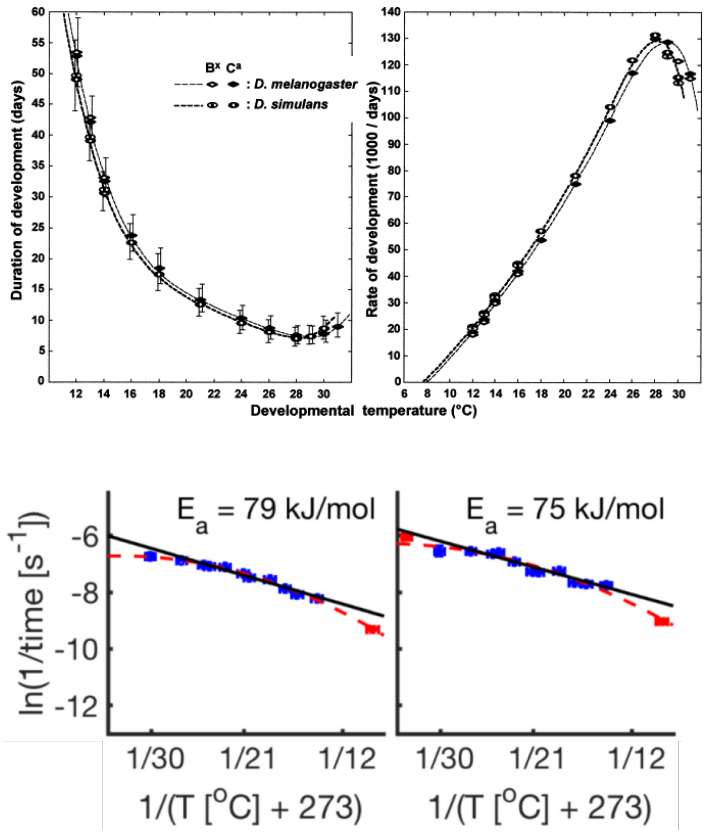

Fig. IV.5 *Top : Total time of development and rate of development, from egg-laying to adult hatching, of Drosophila Melanogaster and Drosophila Simulans as a function of temperature. Adapted from [163]. Bottom : Fit of an effective Arrhenius coefficient by measuring the rate of progression through different steps of development of Drosophila Melanogaster, in particular, cell cycle 13 (left) and cell cycle 14 until the beginning of cellularization (right). Adapted from [162].*

reactions occur in parallel, it would be necessary to have a checkpoint in place such that the system is slaved once again to the set of slowest reactions.

Experiments have shown that Drosophila can develop in a wide temperature window (see Fig. IV.5), with different developmental rates [163]-[165]. In a big portion of this window, the developmental rate follows Arrhenius law. More detailed experiments have shown that the effective Arrhenius activation energy changes as development goes beyond gastrulation [162] (see Fig. IV.5). This is not a big surprise, given the sharp increase of zygotic transcription driving the activation of new chemical pathways.

Finally, microfluidic experiments have challenged the ability of the embryo to synchronize the cell cycle by putting the two ends of the egg at different temperatures [166]-[168]. This effectively causes the two regions to go through the cell cycle at different speeds. The non-uniform forces produced by the microtubule-mediated nuclear interactions lead to the production of important cytoplasmic flows [168], [169], concomitant with a yo-yo-like motion of the nuclei that has been observed previously [170]. Even in the presence of this sharp

temperature gradient and cytoplasmic flows, the embryo is viable in a wide temperature step range.

In this work, we will consider all of these experimental observations and previous modeling schemes to construct a unifying model of the cell cycle biochemistry to study the speed and synchronization of the cell cycle in the pre-gastrulating embryo of *Drosophila Melanogaster*.

IV.1.2 Modeling chemical reactions : the Gillespie equation

Consider ρ_i as the concentration of chemical i in our compartment. At a mesoscopic level, its dynamics will follow the continuity equation :

$$\frac{\partial \rho_i}{\partial t} + \nabla \cdot \boldsymbol{J}_i = G_i \ , \tag{IV.1}$$

where $\boldsymbol{J}_i = \boldsymbol{v}\rho_i - D\nabla\rho_i$ considering advective and diffusive transport. Now we must treat the source term G_i.

At a fundamental level, chemical reactions are stochastic processes. For a reaction to take place, the two given species must be close enough such that they can interact, and their respective energies must be higher than the energy barrier that separates the bound from the free state. Provided that we find a timescale t large enough such that various random collision events are integrated, but small enough so that the variation in the binding affinities between chemical species remains relatively constant, we can write an approximate solution to the evolution of the number of molecules N_i that we are interested in. Assuming that all reactions produce a single molecule of this product, and considering a well-mixed compartment [171] :

$$\frac{\mathrm{d}N_i}{\mathrm{d}t} = \sum_j a_j\left(\boldsymbol{N}\right) + \sum_j \sqrt{a_j\left(\boldsymbol{N}\right)}\xi_j(t) \ , \tag{IV.2}$$

where ξ_j is a delta-correlated Gaussian white noise process satisfying :

$$\langle \xi_i(t) \rangle = 0 \ , \tag{IV.3}$$

$$\langle \xi_i(t)\xi_j(t') \rangle = \delta(t-t')\delta_{ij} \ . \tag{IV.4}$$

Finally, to obtain concentrations, we divide by the volume of the container :

$$\frac{\mathrm{d}\rho_i}{\mathrm{d}t} = \frac{1}{V}\sum_j a_j\left(V\boldsymbol{\rho}\right) + \frac{1}{V}\sum_j \sqrt{a_j\left(V\boldsymbol{\rho}\right)}\xi_j(t) \ . \tag{IV.5}$$

As a first-order description of reaction kinetics, we consider that $a_j(V\boldsymbol{\rho}) = Va_j\rho_j\rho_i$. Then :

$$\frac{\mathrm{d}\rho_i}{\mathrm{d}t} = \sum_j a_j\rho_j\rho_i + \frac{1}{\sqrt{V}}\sum_j \sqrt{a_j\rho_j\rho_i}\xi_j(t) \ . \tag{IV.6}$$

This equation reveals an intuitive fact. Due to the molecular origin of the noise term, if two systems have the same molecular concentrations but different numbers of particles,

i.e. the two systems have different volumes, the noise amplitude will be different in the two cases. In particular, as the number of particles increases, the amplitude of the noise in the concentration equation decreases. In such a regime, it is sometimes helpful to approximate the multiplicative noise as additive noise to perform analytical calculations. The general idea to keep in mind is that there is one "free" parameter in the equations that connects the molecular concentrations in our arbitrary units with the number of molecules in the system.

Another fact to keep in mind is that the sum of noise terms can be grouped owing to the ξ variables being identically distributed, independent Gaussian variables. Using the additive property of the variances, we have :

$$\frac{\mathrm{d}\rho_i}{\mathrm{d}t} = \sum_j a_j \rho_j \rho_i + \frac{1}{\sqrt{V}} \sqrt{\sum_j a_j \rho_j \rho_i} \xi(t) \ . \tag{IV.7}$$

The sum can also be split into different contributions if convenient, which will be performed in our case. This is the form of the term G_i which must be included in the continuity equation to account for chemical reactions.

IV.1.3 Temperature dependence at mesoscopic scales : Einstein's relation & Arrhenius equation

We will first explore the relationship between the diffusion coefficient and temperature. Consider a particle immersed in a temperature bath under the action of a spatially-dependent potential $E(\boldsymbol{x})$. The probability of finding said particle at a particular position $\boldsymbol{x}$ at a given time t evolves according to the Fokker-Planck equation :

$$\frac{\partial P}{\partial t} + \nabla \cdot (\boldsymbol{v} P - D \nabla P) = 0 \ , \tag{IV.8}$$

where the (deterministic) velocity of the particle v is given by :

$$\boldsymbol{v} = -\mu \nabla E \ , \tag{IV.9}$$

where μ is the mobility.

At steady state :

$$\nabla \log P = -\frac{\mu}{D} \nabla E \ , \tag{IV.10}$$

and hence :

$$P \propto e^{-\frac{\mu}{D} E} \ . \tag{IV.11}$$

However, we also know that in the canonical ensemble :

$$P \propto e^{-\frac{1}{k_B T} E} \ , \tag{IV.12}$$

so we finally arrive at Einstein's relation :

$$D = \frac{k_B T}{\mu} \ . \tag{IV.13}$$

This is a very powerful statement that connects the microscopic world, i.e. the interactions between the particle and the medium where it resides, to the macroscopic world. It is one example of the so-called fluctuation-dissipation relation. In this case, we can derive the mobility μ approximating the shape of the molecule to a sphere and using the Stokes drag coefficient, such that $\mu = 6\pi\eta a$, where η is the viscosity of the medium, and a is the typical radius of the molecule. Assuming that in the temperature range that we are working the changes in viscosity due to temperature are negligible, then the diffusion coefficient should scale linearly with T. Now, we will explore how the reaction rates depend on T.

Consider two chemical species, A and B, that can bond and form a product AB. The typical energy landscape between the two species as a function of their distance is depicted in Fig. IV.6. The reaction rate is inversely proportional to the time that it takes for the product to reach the unbound state. To simplify the discussion, we will place particle A in the origin of our reference frame. How long does it take for particle B to reach a given position in space ? In particular, we will be interested in how long does it take for it to escape the potential well of its interaction with A. What follows is a very handwavy calculation that gives some intuition, yet the reader must know it can be developed in a more formal way.

Let $\tau(x)$ be the time to reach a given target if currently at position x, and let us consider a 1d system for simplicity. As the particle can diffuse, during a time interval Δt the particle can move a typical distance $\pm\Delta x$ with the same probability. The diffusion coefficient relates the size of the random step to Δt, in a scaling fashion : $\Delta x^2 = 2D\Delta t$. The particle can also move due to advection, moving a distance $v\Delta t$. Then, $\tau(x)$ satisfies the following equation :

$$\tau(x) = \Delta t + \frac{1}{2}\left(\tau(x - \Delta x + v\Delta t) + \tau(x + \Delta x + v\Delta t)\right) \ , \tag{IV.14}$$

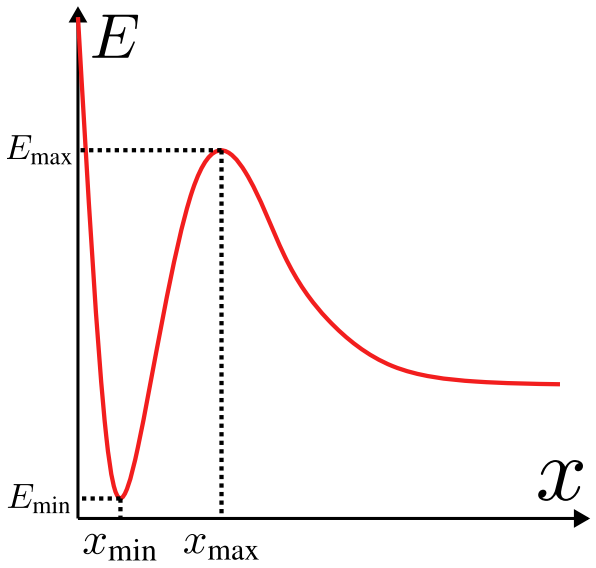

FIG. IV.6 *Sketch showing the typical potential energy landscape between two different chemical species that can form a bond as a function of space. The distance x_{min} represents the mean distance between the particles in the bound state, and x_{max} the distance at which the potential barrier is maximal.*

and expanding as a Taylor series up to order 2 in space derivatives :

$$\frac{1}{D} + \frac{\partial^2 \tau}{\partial x^2} - \frac{1}{k_B T} \frac{\partial E}{\partial x} \frac{\partial \tau}{\partial x} = 0 \ . \tag{IV.15}$$

Consider a solution of the form $\frac{\partial \tau}{\partial x} = A(x) e^{\frac{E(x)}{k_B T}}$. Then :

$$A(x) - A(x_0) = -\int_{x_0}^{x} \frac{1}{D} e^{-\frac{E(x')}{k_B T}} \, \mathrm{d}x' \ . \tag{IV.16}$$

The origin acts as an infinite potential wall. Hence, we can use reflective boundary conditions on τ, such that :

$$A(x) = -\int_{0}^{x} \frac{1}{D} e^{-\frac{E(x')}{k_B T}} \, \mathrm{d}x' \ . \tag{IV.17}$$

Now let's assume that x_0 is our end position, beyond the energy barrier. Then, $\tau(x_0) = 0$, such that :

$$-\tau(x_{\min}) = -\frac{1}{D} \int_{x_{\min}}^{x_0} e^{\frac{E(x')}{k_B T}} \, \mathrm{d}x' \int_{0}^{x'} e^{-\frac{E(x'')}{k_B T}} \, \mathrm{d}x'' \ . \tag{IV.18}$$

If $E \gg k_B T$, then the right (left) integral will be dominated by the minimum (maximum) of the potential energy. At the first order of the saddle point approximation :

$$\tau \propto e^{\frac{\Delta E}{k_B T}} \rightarrow k \propto e^{\frac{-\Delta E}{k_B T}} \ . \tag{IV.19}$$

This is known as Arrhenius equation. Even if we can make some sense out of its derivation, as sketched here, it remains fundamentally an empirical observation, where the prefactor can depend on temperature depending on the circumstances, although it is typically much weaker than exponential. For simplicity, we will consider it as constant.

We can see that the diffusion coefficient scales linearly with T, whereas the reaction rates scale exponentially. We must not forget that, using the international system of units, temperatures ought to be measured in Kelvin, hence a change from 20°C to 40°C represents a change of 7% in the diffusion coefficient. Hence, in the spirit of the simplest description that we can make, we will consider the diffusion coefficient as constant.

IV.2 Modelling

IV.2.1 Geometry of the domain

The embryo can be thought of, in principle, as an ellipsoid of semimajor axis $\sim 250\,\mu\mathrm{m}$ and semiminor axis $\sim 90\,\mu\mathrm{m}$. The nuclei are located at the cortex, where they also move and divide (see Fig. IV.7). A rigorous description of this system would consider a thin shell where the chemical reactions are taking place and the nuclei are moving. We will simplify this situation greatly by mapping the cortex to a plane. But even this is too much for what we

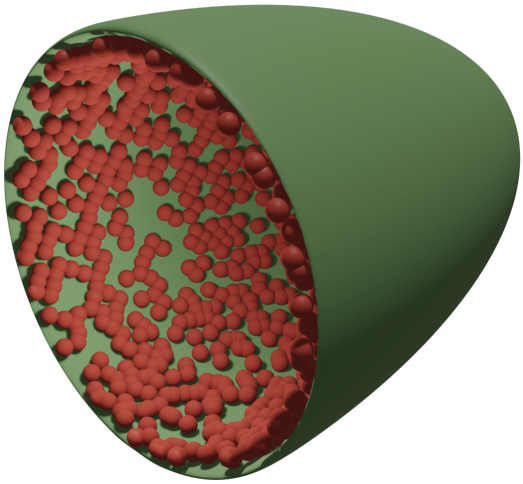

FIG. IV.7 *Artist's impression depicting the nuclei (red) at the cortex (green) of the embryo of Drosophila during the pre-gastrulation nuclear cycles.*

need at the moment. The experimental data that we possess indicates that the dynamics is axially symmetric along the anterior-posterior axis, i.e. both the nuclei and the mitotic waves move parallel to it. Hence, we will consider a 1D geometry, where our effective coordinate would map to a position along the cortex of the embryo. Our domain will have a wall on each side, such that no-flux boundary conditions will be utilized.

IV.2.2 The cell cycle clock

The master regulator of the cell cycle is the Cdk1-Cyclin B dimer. We assume that cyclins are constantly being produced in the egg from abundant maternally deposited transcripts, which then quickly bind to free Cdk1. This dimer can be activated and deactivated by different chemical species that dephosphorylate and phosphorylate it respectively. Of particular importance are the activator phosphatase Cdc25 [172] and the inhibitory kinase Wee1 [173]. The activities of these enzymes are, in turn, dependent on the concentration of active Cdk1 [174], [175], with an ultrasensitive, i.e. large Hill coefficient, regulation [176], [177]. The ubiquitin ligase APC/C is also activated in an ultrasensitive way by active Cdk1, and it tags cyclin-B for degradation [178], bringing down the activity of Cdk1, a requirement for mitotic exit [88]. Finally, Chk1 is a kinase that inhibits Cdc25 and activates Wee1, effectively lengthening the pre-mitotic phases of the cell cycle when active [179], [180], i.e. it is inhibited when the concentration of Cdk1 is large.

Previous numerical and analytical work on this biochemical network in the embryos of *Xenopus* [156], [181], [182] and *Drosophila* [65], [155], [157], [161] have shown that some of these regulatory elements produce oscillations, clearly defined S and M phases, and waves that can spread over space. However, no model has considered all of these elements together, in space, including the nuclear density and temperature effects.

In principle, we would have one equation for each chemical species. However, to simplify

this situation even more, we will consider that there is a separation of timescales between the activity of Cdk1 and the activity of the other regulatory enzymes, such that the activities of the latter ones can be considered as slaved to the concentration of active Cdk1. Then, the concentration of total cyclin c, i.e. active and inactive Cdk1-cyclin B dimer, and the concentration of active Cdk1 a satisfy the following equations (see appendix for parameter values) :

$$\frac{\partial c}{\partial t} = D\Delta c + k_{\text{synth}} - k_{\text{deg}}[a]c + \xi_c \ , \tag{IV.20}$$

$$\frac{\partial a}{\partial t} = D\Delta a + k_{\text{synth}} + k_{\text{Cdc25}}[a](c-a) - k_{\text{Wee1}}[a]a - k_{\text{deg}}[a]a + \xi_a \ , \tag{IV.21}$$

where D is the diffusion coefficient, k_{synth} is the production rate of cyclins and :

$$k_{\text{deg}}[a] = \left(\alpha_{\text{deg}} + \beta_{\text{deg}} \frac{a^{n_{\text{deg}}}}{K_{\text{deg}}^{n_{\text{deg}}} + a^{n_{\text{deg}}}}\right) \ , \tag{IV.22}$$

$$k_{\text{Cdc25}}[a] = \left(\alpha_{\text{Cdc25}} + \beta_{\text{Cdc25}} \frac{a^{n_{\text{Cdc25}}}}{K_{\text{Cdc25}}^{n_{\text{Cdc25}}} + a^{n_{\text{Cdc25}}}}\right)\left(1 - h\frac{K_{\text{Chk1}}^{n_{\text{Chk1}}}}{K_{\text{Chk1}}^{n_{\text{Chk1}}} + a^{n_{\text{Chk1}}}}\right) \ , \tag{IV.23}$$

$$k_{\text{Wee1}}[a] = \left(\alpha_{\text{Wee1}} + \beta_{\text{Wee1}} \frac{K_{\text{Wee1}}^{n_{\text{Wee1}}}}{K_{\text{Wee1}}^{n_{\text{Wee1}}} + a^{n_{\text{Wee1}}}}\right)\left(1 + h\frac{K_{\text{Chk1}}^{n_{\text{Chk1}}}}{K_{\text{Chk1}}^{n_{\text{Chk1}}} + a^{n_{\text{Chk1}}}}\right) \ , \tag{IV.24}$$

are the chemical rates, and h is the parameter that links the N/C ratio to the activation of Chk1 ; its dynamics will be described in the next section. The noise correlations satisfy [171] :

$$\langle \xi_c(x,t)\xi_c(x',t')\rangle = \sigma_c^2 \left(k_{\text{synth}} + k_{\text{deg}}[a]c\right)\delta(x-x')\delta(t-t') \ , \tag{IV.25}$$

$$\langle \xi_a(x,t)\xi_a(x',t')\rangle = \sigma_a^2 (k_{\text{synth}} + k_{\text{Cdc25}}[a](c-a) + k_{\text{Wee1}}[a]a + k_{\text{deg}}[a]a)\delta(x-x')\delta(t-t') \ . \tag{IV.26}$$

Note that the production rate could depend on the cell cycle through a yet unknown mechanism that slightly lengthens the cell cycle even in Chk1 mutants [161]. We will ignore this to build a simple description that could be expanded in future explorations.

IV.2.3 N/C ratio control

As a first approximation, we will consider that the only variable controlled by the N/C ratio is the activity of Chk1. In particular, we will extend a model of control via titration that has been proposed and modeled without taking into account space and the complete cell cycle dynamics [160], [161], [183].

Based on the observations of the competition to import histone H3 into the nuclei, we will model the dynamics by including a generic importin protein that will incorporate the titration molecule into the nuclei. These importins, and the titration molecule, will be produced with a fixed rate, and the binding between the two will satisfy simple mass-action kinetics. Let Y correspond to the concentration of a given titration molecule, and let I be the concentration of the molecular complex that transports said molecule into the nuclei. We will assume that

this transport is purely diffusive and that this complex cannot be reutilized after entering the nucleus. $[YI]$ will denote the concentration of the titration molecule-transport complex dimer. Then, the kinetics of this system satisfy :

$$\frac{\partial Y^{\mathrm{cyt}}}{\partial t} = D\Delta Y^{\mathrm{cyt}} + \alpha_Y - k_{YI} Y^{\mathrm{cyt}} I \ , \tag{IV.27}$$

$$\frac{\partial I}{\partial t} = D\Delta I + \alpha_I - k_{YI} Y^{\mathrm{cyt}} I - \delta_I I \ , \tag{IV.28}$$

$$\frac{\partial [YI]}{\partial t} = D\Delta [YI] + k_{YI} Y^{\mathrm{cyt}} I - k_{\mathrm{imp}} [YI] N \ , \tag{IV.29}$$

$$\frac{\mathrm{d}Y^{\mathrm{nuc}}}{\mathrm{d}t} = k_{\mathrm{imp}} [YI] \ . \tag{IV.30}$$

Let us consider a spatially uniform case to gain further intuition. If the dynamics of I and $[YI]$ are fast in comparison to other timescales, then :

$$\frac{\mathrm{d}Y^{\mathrm{nuc}}}{\mathrm{d}t} = \frac{\alpha_I}{N} \frac{Y^{\mathrm{cyt}}}{(\delta_I / k_{YI}) + Y^{\mathrm{cyt}}} \ , \tag{IV.31}$$

which has the same form as proposed in [183], with the maximum import rate given by the importing production rate, and the Michaelis constant is equal to the ratio of importin degradation to titration molecule-importin association rate.

A coarse-grained description of the system considers the activation of Chk1 to depend on the nuclear concentration of the titration molecule [161]. We will extend this by postulating that the activation threshold will depend linearly on the DNA fraction ϕ present in the nuclei, such that :

$$h = h^* \frac{1}{1 + \frac{Y^{\mathrm{nuc}}}{\phi K_Y}} \ . \tag{IV.32}$$

IV.2.4 Nuclear division and nuclear envelope breakdown

The objective of the cell cycle is to replicate the nuclei, and because the distribution of the nuclei is involved in the regulation of Chk1, it is necessary to model them. One of the hallmarks of the M phase is the rupture of the nuclear envelope, such that the genetic material of the nuclei is no longer separated from the egg cytoplasm. It does not make sense to talk about nuclear import during this phase, so we need to establish a protocol in our formalism to account for this phase. We define two Cdk1 thresholds, a^* and a^{**} respectively, with $a^* > a^{**}$. If a given nucleus is in S phase, and the active Cdk1 concentration around it hits $a > a^*$, the nuclear envelope breaks down, and it will be marked as a nucleus in M phase. Then, for a nucleus in M phase, if $a < a^{**}$, the nuclear envelope will reform, and two new nuclei in S phase will occupy its place. Cell division is a complex process, involving the positioning and orientation of the mitotic spindle and the integration of forces pulling on the chromosomes and aster-aster interactions between different spindles. As a first, effective description, we will ignore all of these elements and consider the number of nuclei in space $N(x)$ to evolve exclusively following the nuclear envelope reform mechanism just described.

During the M phase, the nucleus releases all the non-DNA-bound titration molecules into the cytoplasm, and no transport into the nucleus is possible, i.e $k_{\text{imp}} = 0$.

Without loss of generality, we can assume that the concentration of DNA-bound titration molecule in the nucleus can reach a maximum value of ϕ per DNA chain in wild-type embryos, where ϕ is the DNA fraction compared to WT. Then, if given enough supply, each daughter nuclei will start with a concentration of DNA-bound titration molecule equal to ϕ. We will assume that if the initial amount of relative DNA-bound titration molecule in a daughter nucleus falls below a certain value Y^*/ϕ, it will trigger transcriptional activity due to the activation of DNA damage response.

IV.2.5 Transcription-driven degradation of Twine protein

The model that we have described thus far does not result in cell cycle arrest. Even if the nuclear density goes beyond a threshold where the nuclei cannot import enough titration molecules in a typical time τ, our model considers a continuous production of titration molecules and import complexes, such that the cell cycle arrest is always momentary. Current experiments do not set a constraint on the import rate or the production of titration molecules at the onset of cell cycle slowing, so we will not make this assumption in the model. Rather, we will turn to observations about the dynamics of the Cdc25 homologs String and Twine.

Experiments have shown that beyond its modulation as the concentration of Cdk1 changes over time, Twine is degraded at the beginning of cycle 14 [184]. This is correlated with the start of transcriptional activity, with Tribbles one of the transcripts that has been shown to degrade Twine [185], [186]. The rule for a nucleus to activate transcription is mentioned in the previous section. Let θ be the concentration of a transcript that inhibits the activity of Twine protein, such as Tribbles. Then, we will explicitly model the concentration of Cdc25 in time and space, s, by taking into account the degradation induced by θ :

$$\frac{\partial s}{\partial t} = D\Delta s + \delta_s \left(\alpha_{\text{Cdc25}} + \beta_{\text{Cdc25}} \frac{a^{n_{\text{Cdc25}}}}{K_{\text{Cdc25}}^{n_{\text{Cdc25}}} + a^{n_{\text{Cdc25}}}}\right)\left(1 - h\frac{K_{\text{Chk1}}^{n_{\text{Chk1}}}}{K_{\text{Chk1}}^{n_{\text{Chk1}}} + a^{n_{\text{Chk1}}}}\right) - \delta_s s - \theta s \ , \tag{IV.33}$$

$$\frac{\partial \theta}{\partial t} = D\Delta\theta + \sum_i{}' \delta(x - x_i)\alpha_\theta \ , \tag{IV.34}$$

where the sum runs over all the positions where nuclei are actively transcribing θ. Using the same separation of timescale argument that was used to write the original equations of the model, i.e. assuming that the relaxation time of this equation is relatively fast, then we can approximate the effective concentration of Cdc25 as :

$$s = \frac{1}{1 + \frac{\theta}{\delta_s}} \left(\alpha_{\text{Cdc25}} + \beta_{\text{Cdc25}} \frac{a^{n_{\text{Cdc25}}}}{K_{\text{Cdc25}}^{n_{\text{Cdc25}}} + a^{n_{\text{Cdc25}}}}\right)\left(1 - h\frac{K_{\text{Chk1}}^{n_{\text{Chk1}}}}{K_{\text{Chk1}}^{n_{\text{Chk1}}} + a^{n_{\text{Chk1}}}}\right) \ , \tag{IV.35}$$

which is completely consistent with having θ as a regulatory molecule.

IV.3 Results

IV.3.1 Single oscillator dynamics in phase space

We started by considering the simplest situation : a single compartment where the chemical species are homogeneous in space, and the Chk1 activity threshold h is fixed, i.e. there is no nuclear envelope breakdown nor titration molecule import. In doing this, we can focus exclusively on the dynamics of the active Cdk1 concentration a and the total cyclin concentration c over time. The dynamical system governing the evolution of these two quantities possesses a single parameter, h. As it is well known, 2 dimensional dynamical systems can display a limited set of behaviors, and codimension-one bifurcations have been well characterized, so it is a good simplified system to study.

The dynamical system contains multiple nonlinearities that change with h, so we will resort to graphical methods to study the behavior of the system. First, we plotted the nullclines of both chemical species in Fig. IV.8a, revealing that the system possesses a single fixed point. The stability of such a fixed point can be determined from the intersection between the nullclines. In a particular window of values of h, the nullclines intersect in such a way that the fixed point is linearly unstable. As the degradation terms ensure that both a and c must decrease if they grow too large, the trajectories cannot go to infinity. Hence, theoretically, the only option is for the system to possess an attractor other than a fixed point. In 2d, the only such option is a limit cycle, and because of the constraint just mentioned this limit cycle must be stable.

We plotted the eigenvalues of the linear stability matrix around the fixed point in Fig. IV.9a,b, and c, and we can make the following remark. For our chosen parameter values, there exists a negative value of h such that the system undergoes a Hopf bifurcation. The reasoning behind having a parameter set such that this value is negative is as follows. As more titration molecules are imported into the nuclei, h decreases. In the limit where the concentration of nuclei is very small, each nucleus can import these molecules fast enough, and $h \to 0$. If the bifurcation happened for $h > 0$, then for a given nuclei concentration, the cell cycle would stop, which is not reasonable considering that divisions are happening from fertilization onwards. Mapping the microscopic parameters of the model to the normal form of this Hopf bifurcation is beyond the scope of this work, and is left for future explorations.

As shown in Fig. IV.8b, as h increases, the period of the oscillations increases as well, and they become "spikier" until reaching a homoclinic bifurcation, i.e. the limit cycle collides with a stable fixed point. This is also referred to as an infinite period bifurcation because the system remains excitable, and if driven far enough from the stable fixed point, it will be driven around the cycle back to the fixed point in a homoclinic orbit. This "spikyness" represents the lengthening of the S phase (slow growth) whereas the duration of the M phase (fast growth) remains relatively constant, which is an experimental fact. Different parameter choices lead to qualitatively similar phenomenologies, with the main differences in how big the h window where oscillations are happening is. For some parameter choices, no value of h allows for oscillations.

At first glance, the existence of this infinite period bifurcation in the dynamical system

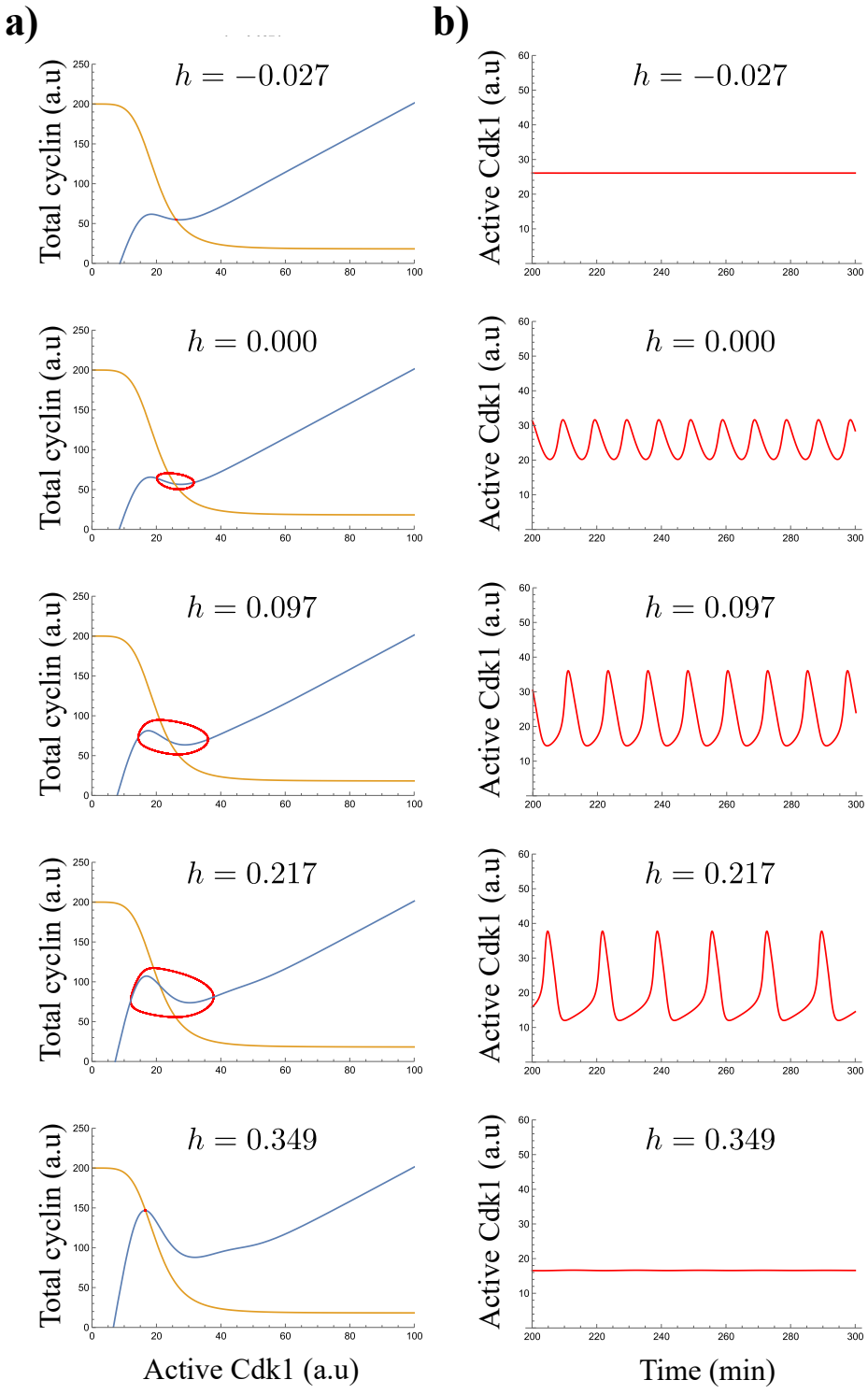

FIG. IV.8 *Dynamics of the cell cycle biochemistry in a single compartment for different values of Chk1 activity h. a) Active Cdk1 vs total cyclin phase portrait. Cdk1 growth nullcline in blue, cyclin growth nullcline in yellow, and temporal dynamics in red. b) Active Cdk1 vs time for the same values of h as on the left.*

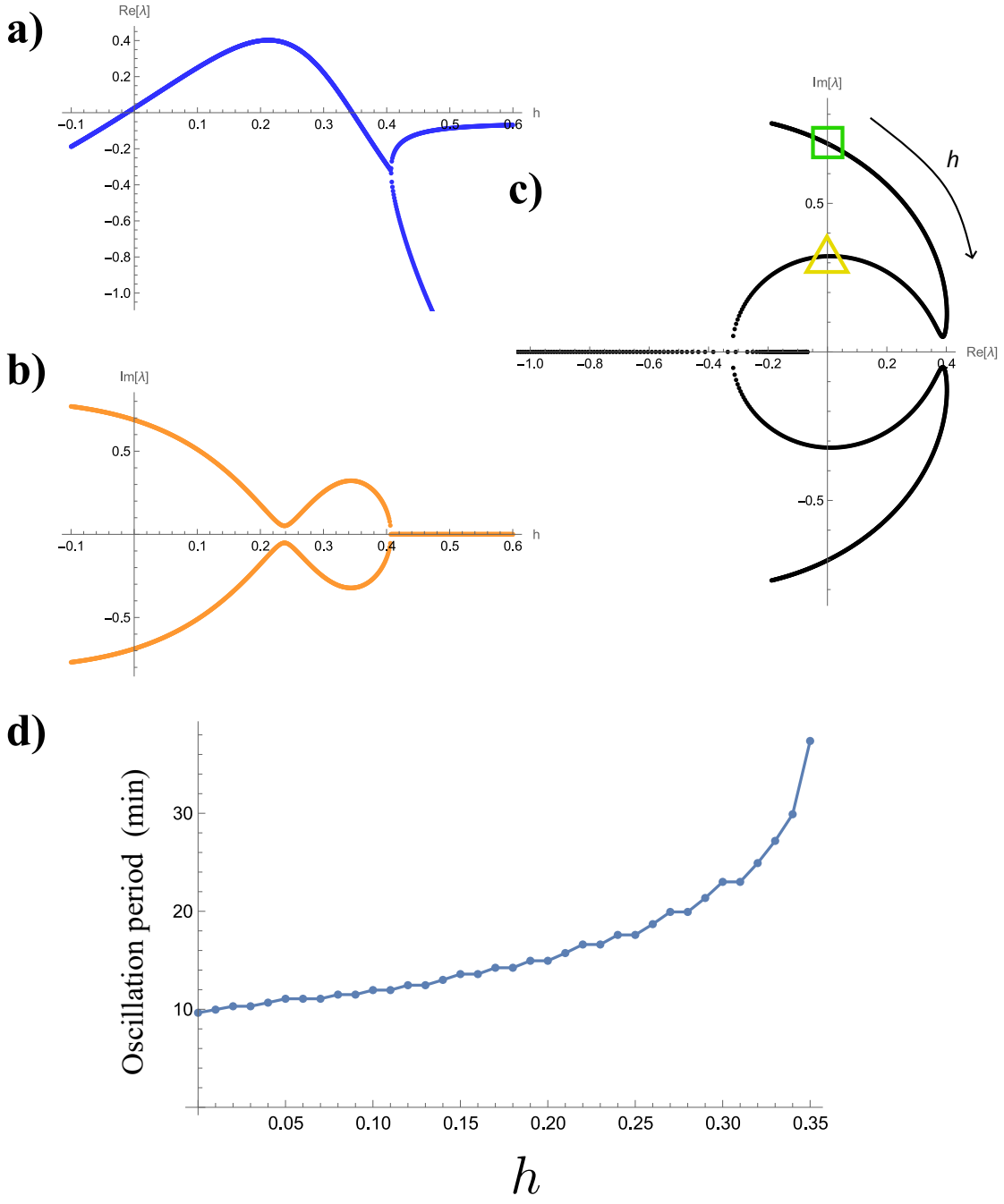

FIG. IV.9 *a) Real and b) imaginary part of the two eigenvalues of the linearized dynamics around the fixed point as a function of h. c) Dynamics of the two eigenvalues of the linearized dynamics around the fixed point in the complex plane as a function of h. Green square : Hopf bifurcation. Yellow triangle : Homoclinic (Infinite period) bifurcation. d) Oscillation period of the limit cycle as a function of h.*

hints at cell cycle arrest. In particular, our experimentally-motivated functional form of h decreases as the nuclei density increases because each one of them cannot import as much titration molecule as it would in isolation. However, as mentioned in the modeling section, this is not the full picture because the import of the titration molecule does not stop, even if very small. Hence, true arrest requires transcription of the Twine-degrading molecule. The link between this excitable state and the mitotic patches could be of theoretical interest when studying embryos where regions do not divide evenly. This is, however, left for future work.

Finally, we determined numerically the period of the cell cycle oscillations for different values of h (see Fig. IV.9d). We note an initial quasi-linear scaling, followed by a sharp increase in the slope of the curve when getting close to the infinite period bifurcation. We have chosen our parameters such that we have a range of periods that reproduce the duration of the different cell cycles in pre-gastrulating *Drosophila* embryos. The analytic form of this oscillation period as a function of the various microscopic parameters of the model is left for future work.

IV.3.2 Wave propagation and slowdown

We simulated the model starting from the beginning of the S phase of cycle 11. For the sake of simplicity, all the concentrations are chosen to be homogeneous at the start of the simulation. Space is discretized with $\Delta x/L = 0.01$, and $N = 8$ at every location. First, looking at the time series of the concentration of active Cdk1 at a particular location in the embryo in Fig. IV.10, we observe that our simulations reproduce the experimental observations of regions of slow increase of Cdk1 (S phase) followed by a spiking region (M phase). As observed experimentally, the duration of the S phase increases as divisions go forward, whereas the duration of the M phase remains constant between 4 and 5 minutes. We quantified the duration of each cell cycle, and our chosen parameters lead to values (see Fig. IV.11a) that match experimental observations [63], [155], [161].

We also performed simulations changing the global temperature in the embryo by scaling all the reaction rates by a common factor $e^{-\frac{\Delta E}{k_B}\left(\frac{1}{T}-\frac{1}{T_0}\right)}$, and we observed that the cell cycle sped up (slowed down) when increasing (decreasing) the temperature (see Fig. IV.11a). Going further, in Fig. IV.11b we plotted the duration of cell cycle 13 for a range of different temperatures, and we verified that their scaling follows the same Arrhenius scaling that was found experimentally [162] and that we introduced into our model via the chemical rates.

Next, we studied the dynamics of Cdk1 in the whole embryo. By looking at the kymograph of active Cdk1 at different positions in the embryo as a function of time in Fig. IV.11c, we can see that the time of entry into M phase (Yellow color) is not the same for every position. And cycle 13 is the one where this asynchrony is the most pronounced. To characterize the synchrony of mitosis, we measured the time of nuclear envelope breakdown for a given cell cycle at every position in space, and we extracted the maximum difference between these times. These results have been plotted in Fig. IV.11d. We observed that this embryo-wide asynchrony τ_L increases significantly from cell cycle 12 to 13, in comparison to the jump from cell cycle 11 to 12. This is in complete correspondence with experimental observations on the mitotic waves. Another feature of the model is the increase of τ_L as T decreases (see

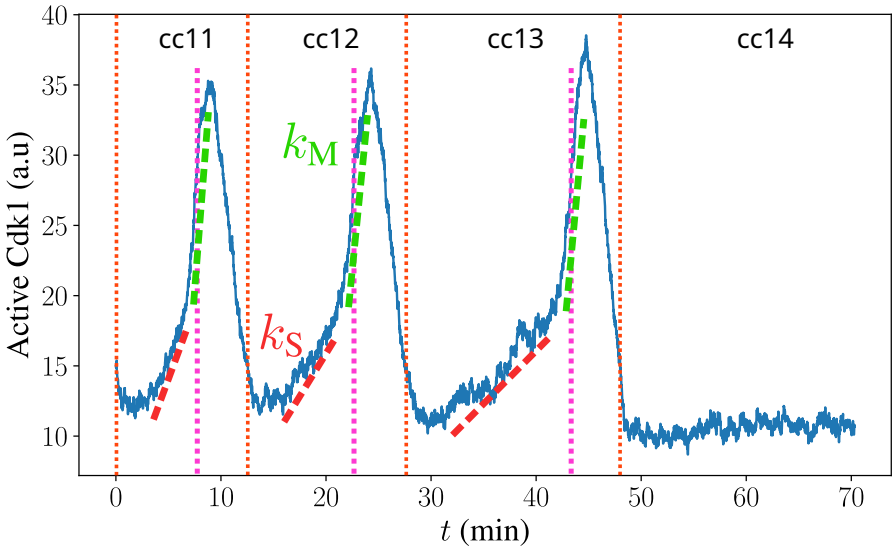

FIG. IV.10 *Representative dynamics of the concentration of active Cdk1 as a function of time in the embryo from cycle 11 to 14. Dotted orange lines mark the beginning of each cycle as the nuclear membrane reassembles. Dotted pink lines mark the nuclear envelope breakdown. Slanted segmented lines illustrate the characteristic activation rate of Cdk1 during S phase (Red) and M phase (Green) for each cycle.*

Fig. IV.11d), which is consistent with previous experimental measurements [91]

Next, we looked at the influence of the DNA fraction present in the nuclei on the cell cycle. In a wild-type embryo, the proposed titration mechanism allows the nuclei to sense "which" cell cycle are they in thanks to the concentration of their titration molecule. However, if this sensing depends on the DNA fraction in the embryo, alterations to it should lead to an "intermediate" cell cycle. Fig. IV.11e shows the duration of cell cycle 13 for different DNA fractions, and our results agree with the same linear scaling that has been observed in the literature. Note that the results consider a reduced range of DNA fractions, this is because further changes cause mitotic patches to appear, which will be left for the next section.

Finally, we looked at the effective activation rates of Cdk1 during the different S phases. By simulating embryos with different DNA fractions $\phi = 0.8$, 1, and 1.2, we plotted k_S as a function of the DNA fraction, compared to the WT embryo at cycle 13 (see Fig. IV.11f). The linear scaling for the effective cycles 12 and 13, and the significative jump going to the effective cycles 11 are characteristics that agree with experimental observations [155].

IV.3.3 Mitotic patches in embryos with altered N/C ratios

Our simulations reproduce the formation of patches in the case where the embryo has an altered DNA content. Fig. IV.12a,b show two kymographs for cycles 13 and partial cycle 14 with $\phi = 0.71$. Notably, the speed of the wave decreases at the edges of the patch. This is a

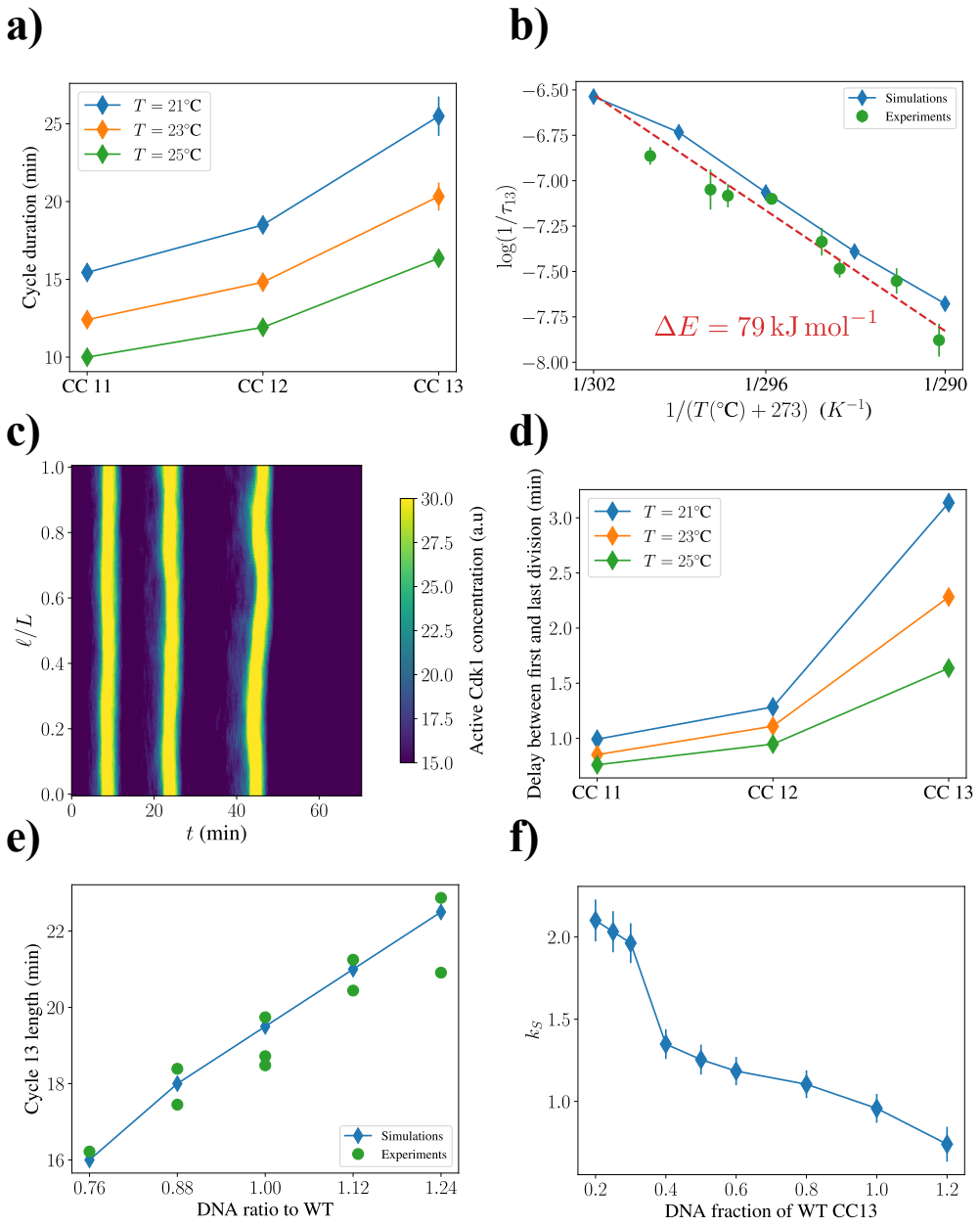

FIG. IV.11 *a) Cell cycle duration for cycles 11, 12, and 13 for three different temperatures. b) Reciprocal of the duration of cell cycle 13 vs reciprocal of temperature, in log-linear scale. Red dotted line represents the linear scaling that would follow from Arrhenius law. Experimental data retrieved from [162]. c) Kymograph of the active Cdk1 concentration over time in the whole embryo showing the completion of cycles 11, 12, and 13. d) Time delay between first and last completion of cell cycles 11, 12, and 13 in the whole embryo for three different temperatures. e) Duration of cell cycle 13 vs the DNA fraction in the nuclei. Experimental data retrieved from [63]. f) Effective Cdk1 activation rate during S phase k_S for different DNA contents compared to WT cycle 13.*

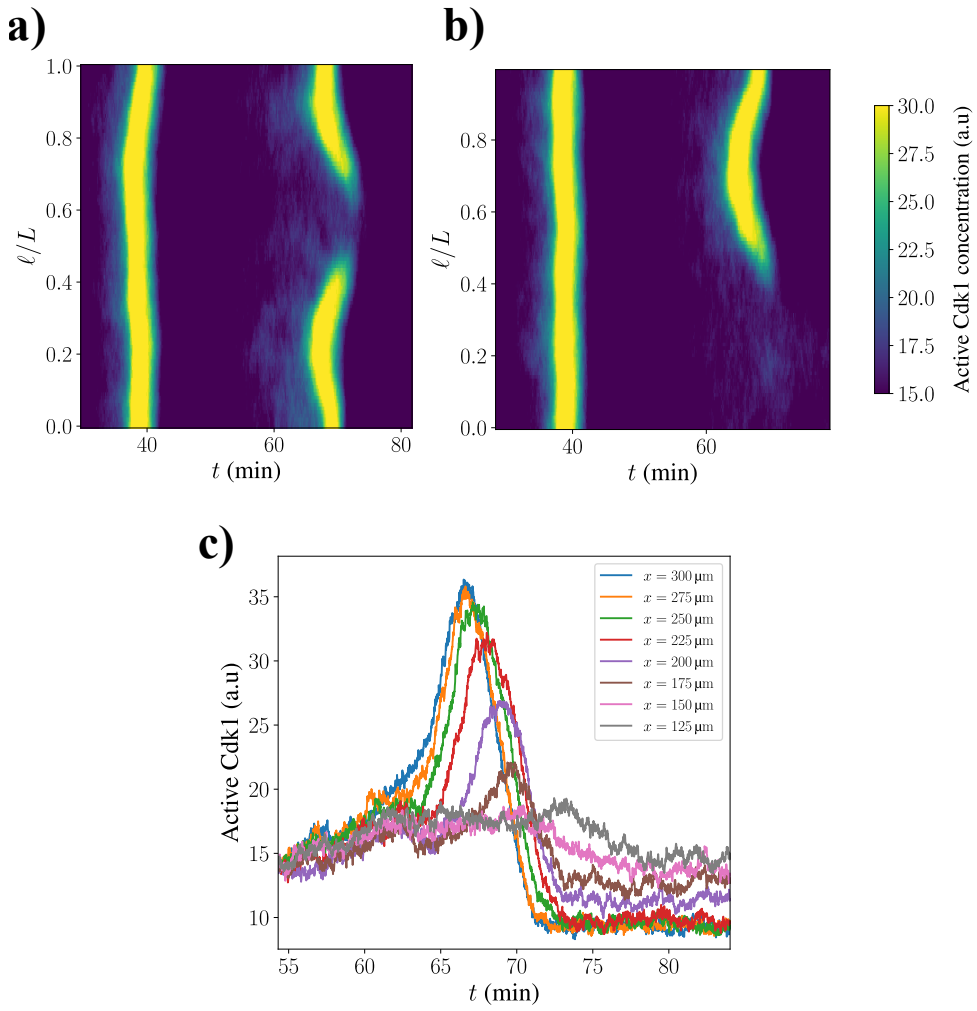

FIG. IV.12 *a,b) Two representative kymographs of the Cdk1 activity over time in an embryo with DNA fraction $\phi = 0.71$ showing full completion of cycle 13 and patchy completion of cycle 14. c) Temporal dynamics of active Cdk1, curves color-coded by positions in space separated by* 25 µm *at the edge of the mitotic patch shown for partial cell cycle 14 in b).*

direct consequence of our assumptions : Cdc25 is being degraded in the regions close to the arrested patches. As Cdc25 diminishes, the activation of Cdk1 slows down, until reaching a point where no oscillations are possible (see Fig. IV.12c). In an analogous way of a previously explored *Drosophila* mutant [155], [157], the reduction of Cdc25 makes the wave transition from a phase wave to a slow bistable wave. This feature has also been observed in *shkl* embryos, but has remained yet unexplored [65].

We can also see that the two simulations produced different patch sizes, not necessarily connected, even if having the same DNA content. We performed 800 simulations for different values of the DNA fraction ϕ and plotted the histogram of the fraction of the embryo that undergoes an extra division (see Fig. IV.13). By looking at the histograms, the transition from preferentially arresting after cycle 13 to preferentially arresting after cycle 14 is centered

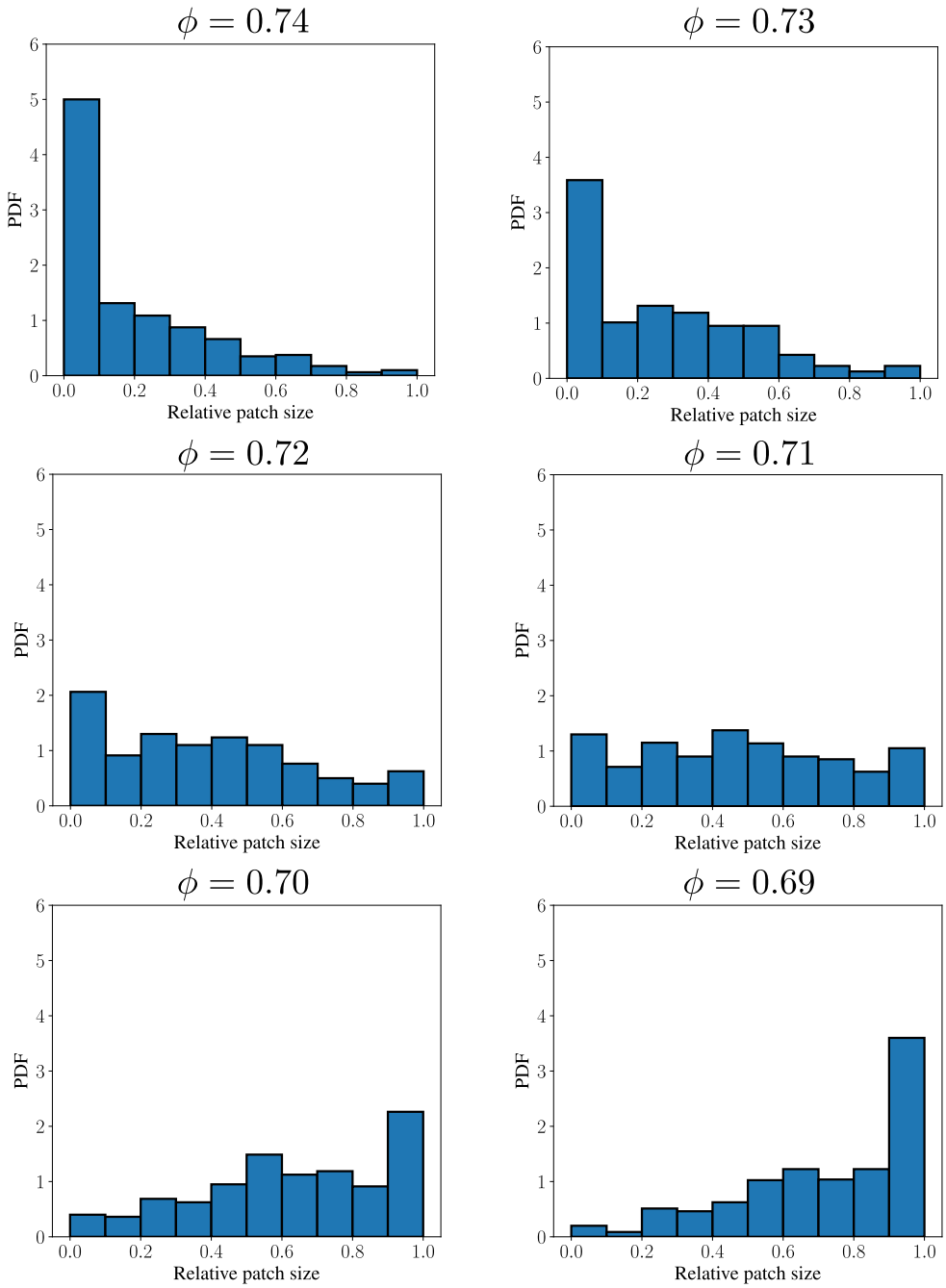

Fig. IV.13 *Size histograms of the extra cycle 14 division patch for different values of the DNA fraction ϕ. In each case, 800 simulations were considered.*

around $\phi^* \approx 0.71$. We make this point more clear in Fig. IV.14 by plotting the average fraction of the embryo undergoing an extra division as a function of ϕ. We can see that there is a sharp transition at a certain DNA concentration range, which for our chosen parameters occurs close to $\phi^* \approx 0.71$. This is in very good agreement with experimental observations [63]. Observing this transition point *in vivo* would be challenging due to the amount of precision and statistics necessary. However, it could be interesting to obtain the experimental distributions to compare with our predictions. It is likely that the sharpness of the transition is related to some of our model parameters, like the Twine-degrading molecule production or degrading strength, that could be better constrained with this kind of data.

There is a critical value of the titration molecule that must be present in the nucleus when the nuclear membrane reforms such that it does not trigger transcription, which has been assumed to scale linearly with DNA content. Beyond altering the duration of the cell cycle, the DNA fraction is not involved in the import dynamics of the titration molecule. Hence, when the membrane reforms, it is likely that some nuclei will be above and others below this threshold for a range of values of the DNA content. The Twine-degrading molecule will be produced in the regions below the threshold, diffusing to the other regions. This induces a natural integration length over which patches can form, rather than discrete extra divisions. Furthermore, its degrading activity is racing against the progression of the cell cycle. A scaling argument reveals that just like Cdk1 [155], $\ell = \sqrt{4D\tau}$ is a relevant integration lengthscale (see appendix), with τ the typical S-phase time, i.e. $\sim 10\,\text{min}$. Hence, $\ell \sim 100\,\mu\text{m}$. Future work can utilize these ideas to construct a model to predict the patch size distribution and relate it to controllable experimental parameters.

Finally, we performed numerical simulations where we introduced a gradient in the nuclear density, emulating the *shkl* embryo. These gradients have been set by considering the original homogeneous situation of $N = 8$ nuclei at every position in space, with $\Delta x = 0.01L$,

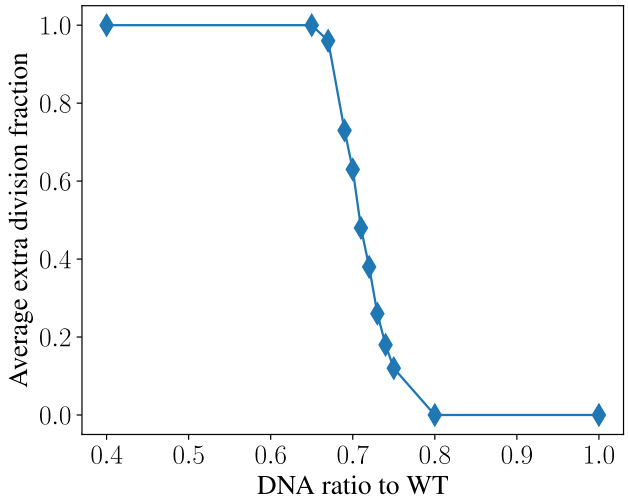

FIG. IV.14 *Average fraction of the embryo undergoing an extra cycle 14 division before cell cycle arrest as a function of the DNA Fraction.*

and then partitioning the embryo into chunks of a given size. When crossing from one chunk to the other, the amount of nuclei at the start of the simulation will be reduced by one compared to the previous chunk. As an example, if the chunk size is $\ell_{\text{chunk}}/L = 0.2$, positions $x \leq 0.2L$ will contain 8 nuclei, $0.2L < x \leq 0.4L$ 7 nuclei, and so on. As seen in Fig. IV.15 our model reproduces the mitotic patches in the less dense region. Patches were also produced for varying quantities of DNA ratio ϕ, and their size increased as ϕ diminished. This has a clear interpretation. Let N^* be the number of nuclei per chunk at CC14 in the WT embryo. Then, $\phi^* N^*$ is the threshold amount of DNA per chunk to trigger cell cycle arrest. Then, we predict an extra mitotic division in a chunk that satisfies $\phi N(x) < \phi^* N^*$, and a domain wall separating these chunks from the chunks satisfying $\phi N(x) > \phi^* N^*$. This corresponds very well with our simulations. As was shown in the histograms for embryos with a uniform distribution but altered DNA contents, there are some fluctuations. However, the extra division patch is always located past the predicted value. This can be easily interpreted in the light of our model. The high-density region will arrest the cell cycle and start to produce the Twine-degrading molecule, which then starts diffusing to the other region. Then, just like previously argued in the uniform density case, there is a competition between the cell cycle duration and the degradation of Twine due to the wavefront of the degrading species that is coming from the other side. Hence, the extra division wall will, on average, be beyond the expected threshold. How far in space does this shift our naive prediction should depend on the timing of the divisions, i.e. how steep the density gradient is, and will be left as future work.

IV.3.4 Non-uniform temperatures

As a simple setting, replicating previous experimental settings, we will split the embryo into two parts, one of them at $T = T_1$, and the other one at $T = T_2$. We will assume the simplest initial condition by having the same levels of active Cdk1 everywhere in the embryo. To gain some intuition, we will use the same simplified model that we have used before, with the sole difference being that the temperature in the Arrhenius coefficient will be space-dependent. We will then discuss what happens in a more realistic scenario.

First, our simulations indicate that deep in the bulk of each region, i.e. at the boundaries of the domain, the period of the oscillations is not influenced by the presence of the other region. This means that as time goes by, oscillations go more and more out of sync (see Fig. IV.16). This means that the largest time delay between the end of CC13 in the two different regions can be approximated by the following expression (see appendix) :

$$\tau_L \approx (\tau_{11} + \tau_{12} + \tau_{13}) \frac{\Delta E}{k_B} \frac{\Delta T}{T_0^2} \ , \tag{IV.36}$$

where τ_{11}, τ_{12} and τ_{13} are the durations of CC11, CC12 and CC13 respectively, at the reference temperature T_0. With our parameters, this expression simplifies to $\tau_L \approx \Delta T/10$, and its results correspond well with the simulation data.

We may note that at the boundary between the two temperatures, we get a matching region where a bistable front can propagate from the region that is dividing first to the other one. However, diffusion can only get the wave so far. The scaling of this matching region is left

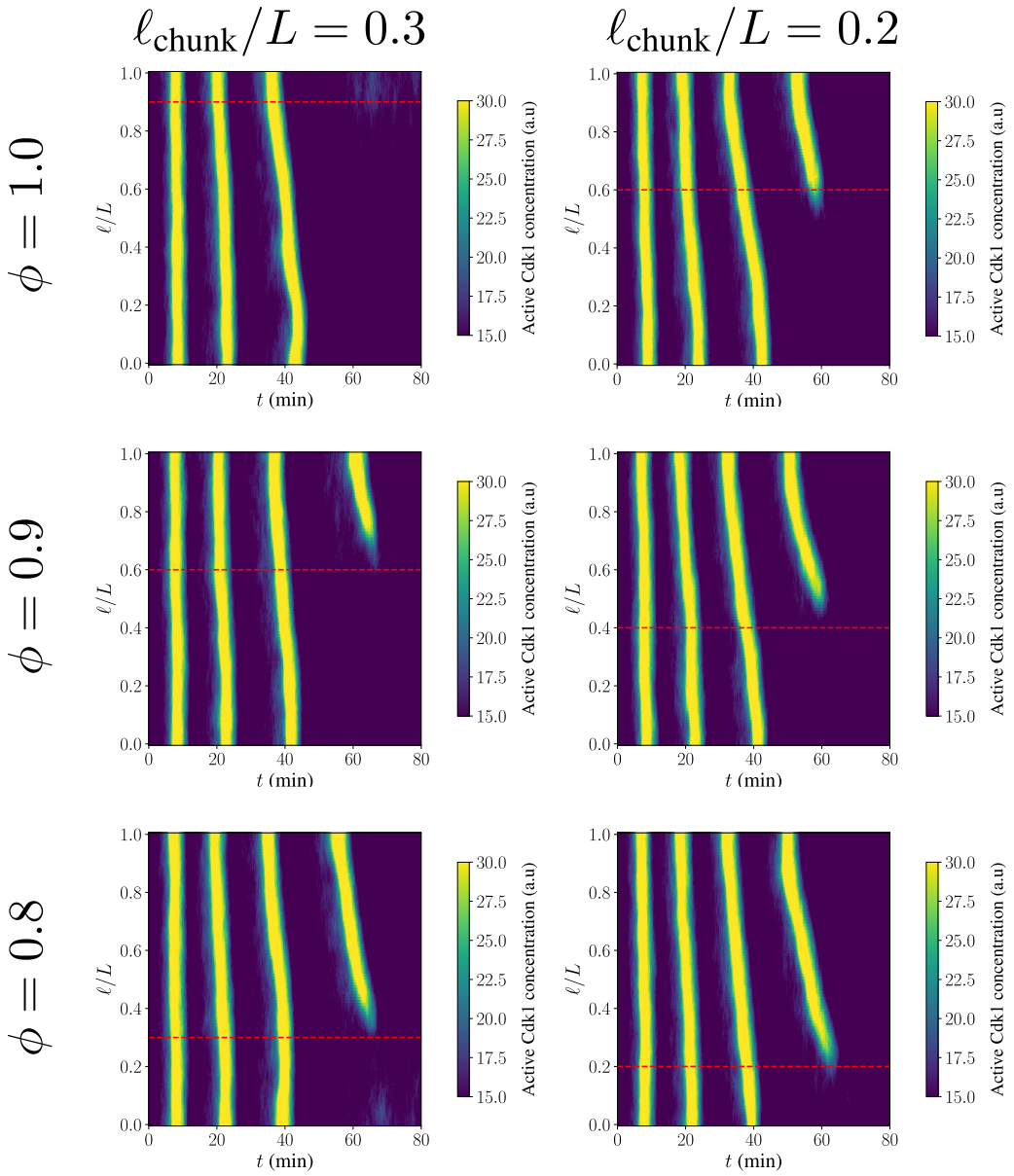

FIG. IV.15 *Kymographs showing the activity of active Cdk1 during cycles 11,12, 13, and (patchy) 14 in embryos presenting a decreasing gradient in their nuclear density in the direction $\ell/L = 0 \to 1$. The domain is separated into chunks of size ℓ_{chunk}, with each one of them having one additional nucleus removed compared to the previous one in their initial condition. Three different values of the DNA fraction in the embryo ϕ are shown. Red dashed lines : predicted position of the domain wall between extra division and arrested patch.*

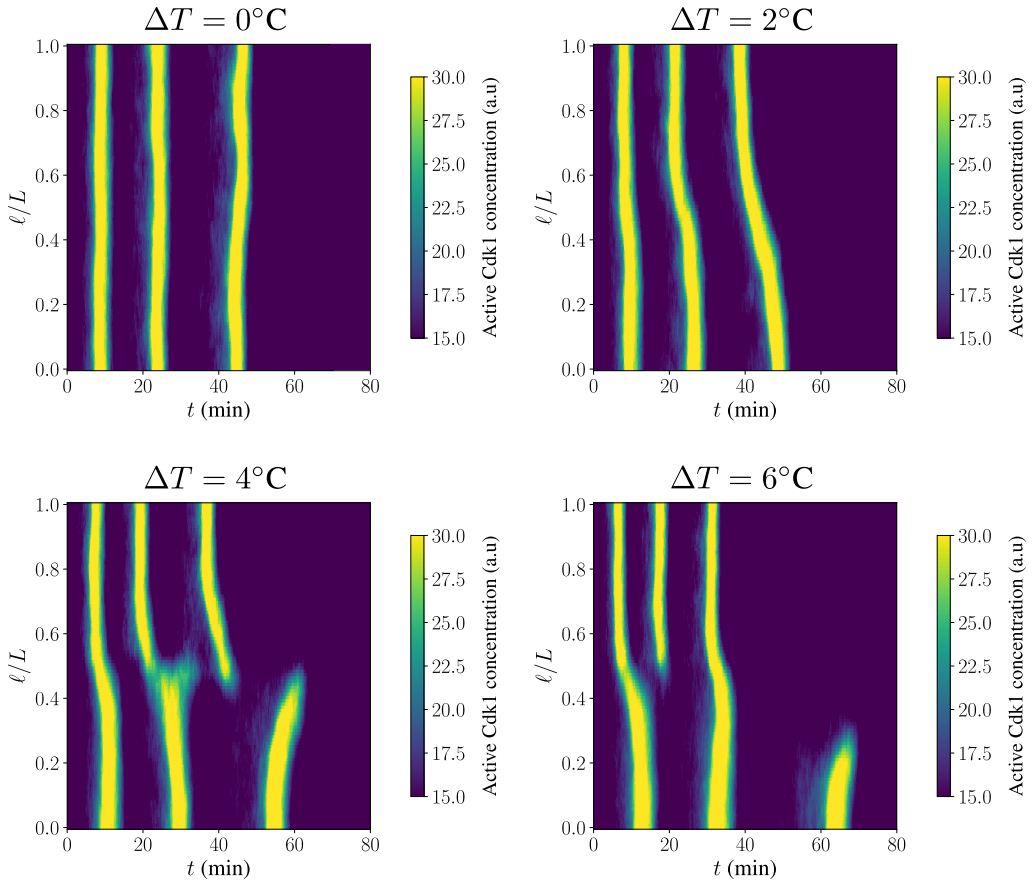

Fig. IV.16 *Kymographs showing the activity of active Cdk1 during cycles 11,12, and 13 in an embryo where the bottom half and top half are held at different temperatures. Top embryo half : $T = 23°C + \Delta T/2$. Bottom embryo half : $T = 23°C - \Delta T/2$.*

for future work. From a completely mathematical point of view, trying to match regions that are oscillating at different periods must introduce defects, i.e. regions where the mitotic wave is not able to traverse the whole embryo. The question is how large must ΔT be to observe these defects during the 3 divisions before CC14. For $\Delta T = 2°C$, no defect is observed. However, for $\Delta T = 4°C$, we can see in Fig. IV.16 that the wave vanishes mid-embryo during cycle 12, and a region that is stuck at a high Cdk1 value in the middle is observed. This would represent a region where mitosis spends a long time in an intermediate phase, for example right before the separation of the chromosomes. It would be interesting to observe this phenomenon in experiments.

For an even larger temperature difference, we can see a more dramatic effect. As shown in Fig. IV.16 for $\Delta T = 6°C$, the warm region starts its cycle 13 division approximately 30 minutes before the cold region does. This time delay is sufficiently large for the transcription of the Twine-degrading molecule in the warm side to diffuse to the cold side and have a noticeable effect. In particular, we can see that cycle 13 is completed in less than half of the cold region, which would have a dramatic consequence later on in development. In

contrast to this, it must be noted that previous microfluidic experiments have determined that the embryo is viable even with $\Delta T = 7°\mathrm{C}$. Our answer to this is twofold. First, further quantifications of the division patch sizes as a function of temperature could shed light on the spread of the Twine-degradation molecule and the values of certain parameters that for the moment we cannot constrain completely. Tuning these parameters will undoubtedly yield different patch sizes for the same time delay. Second, there is another factor that we have overlooked in simulations up to now and may play a major role in smoothening out these inhomogeneities : the mixing of material in the embryo due to cytoplasmic movements induced by nonsynchronous divisions.

Let us give some preliminary ideas about including hydrodynamics and the explicit modeling of the nuclei in the model. First, all the relevant biochemical reaction-diffusion equations are promoted to reaction-diffusion-advection equations. Moreover, strictly speaking, temperature is also being transported with the flows. A detailed description would consider writing the heat equation in the domain and using fixed T boundary conditions. Then, there is a competition between the equilibration timescale of the temperature in the egg, controlled by the thermal conductivity of the cortex and the cytoplasm, and the timescale of nuclear displacement. If the temperature is very slow in re-equilibrating, then each nucleus should feel the same temperature at all times. On the other hand, if this equilibration is fast, then each nucleus would sample different temperatures as it undergoes its yoyo motion. If this is the case, the resulting mixing of material can help to reduce the asynchrony of the mitotic divisions and could account for a viable embryo at a larger temperature range than what this simple model would predict. These explorations will be left as future work.

IV.4 Discussion

We have studied the spreading of mitotic waves in the pre-gastrulating *Drosophila* embryo. These “oscillators” are conceptually interesting due to their departure from a simple Kuramoto-style phase oscillator, owing to the different dynamics during the S and M phases, and the cycle duration being dependent on the N/C ratio. Beyond the homoclinic bifurcation in the single oscillator picture, the system remains excitable, which is an interesting fact given that embryos where oscillatory and arrested regions exist in the form of the *shkl* embryo. Observing an extra oscillation in the arrested region is hard due to the presence of transcription of the Twine degradation molecule. Further theoretical studies could tackle the behavior of a system with an arbitrary arrangement of regions with different oscillatory characteristics. How long can perturbations propagate in such a complex medium ? What happens at the interface between sections of different oscillatory characteristics ?

We must not forget that we have greatly simplified the geometry of the system, and in doing so we have ignored some effects such as the changes in curvature in different positions of the embryo. Even if considering axial symmetry is a reasonable assumption, experiments have found patches that are not axially symmetric in some situations [62], owing putatively to differences in nuclear density and chemical concentrations in the azimuthal direction. How these effects would play a role in an embryo with an altered geometry, such as the round embryo displaying altered flow structures, has been left unexplored. Further analysis can

consider the production of patches in curved or more complicated surfaces.

There is one aspect of the cell cycle control in the embryo that we have overlooked. Experiments have shown that the response of the nuclei to the N/C ratio is not uniform in the embryo, with a gradient along the anterior-posterior axis yielding better predictive results to the location of the extra division region in comparison to a fixed threshold [65]. This is probably connected to the fact that reversing the temperature step in embryos developing in a microfluidic chamber does not show the same asynchrony as embryos in the original temperature step [166], [168].

The spreading of these waves, and microtubule-mediated nuclear interactions, could be of interest in the context of recent experiments on reconstituted systems [187], [188]. It is possible that the observed microtubule dynamics and compartmentalization could be modified in the presence of temperature gradients, or activity gradients as a function of nuclear density. Furthermore, connecting to our results in Chapter III, a preferential distance of separation in nuclei hints at a different way of producing spatially segregated domains in narrow geometries which can be modulated by either biochemistry or the shape of the domain.

One last remark brings together the formalisms and findings of this chapter to the ones explored in previous chapters. Biological systems rely on mechanical forces and chemical networks to perform different tasks. Beyond the specificity of these tasks, reproducibility is fundamental, hence energy must be spent to amplify signals and drive active processes. In other words, life is intrinsically out of equilibrium, and metabolic pathways must evolve to distribute chemical energy in a "reasonable" way. However, this energy has to come from somewhere, and once the egg is laid, there is no further exchange of matter with its environment. One point that we have not explicitly discussed is the energy use and efficiency of the processes just discussed. Can we quantify how expensive is it to spread the nuclei in comparison with the transcriptional costs of keeping the cell cycle running ? Is the long-range mechanochemical coupling described in previous chapters the most efficient use of resources to produce nuclear transport in the egg of *Drosophila* ? These questions are undoubtedly coupled with the scaling of the size of the embryo and the maximal cell cycle speed.

IV.5 Methods

IV.5.1 Numerics

The single-compartment oscillations results were obtained by using a custom Mathematica code, through the pre-existing routines "FindRoot" (Position of the fixed point in phase space), "Eigenvalues" (Eigenvalues of the linear stability matrix around the fixed point), and "Fourier" (Oscillation period as a function of h).

We performed all of our space-dependent numerical simulations using the finite-difference method implemented in a custom C++ code. Space was partitioned in a regular grid of $n_x = 100$ points with spacing $\Delta x = 5\,\mu\text{m}$, and time was discretized uniformly with $\Delta t = 1\times10^{-4}\,\text{min}$. Equations with noise were integrated using the 1-step Euler-Mayurama method.

If the continuous equation reads :

$$\frac{\partial \rho}{\partial t} = D\frac{\partial^2 \rho}{\partial x^2} + G(\rho, t) + \sigma\sqrt{G(\rho, t)}\xi \tag{IV.37}$$

then the discretized form reads :

$$\rho(x, t + \Delta t) = \rho(x, t) + \frac{D}{\Delta x^2}\left(\rho(x - \Delta x, t) - 2\rho(x, t) + \rho(x + \Delta x, t)\right)\Delta t + G(\rho(x, t), t)\Delta t + \sigma\sqrt{G(\rho(x, t), t)}\xi(x, t)\sqrt{\Delta t} \tag{IV.38}$$

where every $\xi(x, t)$ was extracted independently from a normal distribution for every position and time. Pseudorandom number generation : mt19937 (Mersenne Twister).

No flux boundary conditions were implemented by assigning values at ghosts positions outside of our domain :

$$\rho(-\Delta x, t) = \rho(\Delta x, t) \tag{IV.39}$$

$$\rho(n_x \Delta x, t) = \rho((n_x - 2)\Delta x, t) \tag{IV.40}$$

$$\tag{IV.41}$$

where we must note that the last index in the grid is $(n_x - 1)$ due to zero-indexing.

All posterior data analysis and visualization was implemented in custom Python codes.

A – Chapter II Appendix

A.1 Notation

— Ω : embryo domain.
— $\partial\Omega$: embryo boundary.
— $\hat{\boldsymbol{n}}$ and $\hat{\boldsymbol{t}}$: normal and tangent vectors to the embryo boundary.
— $\boldsymbol{w}^v$, $\boldsymbol{w}^u$, $\boldsymbol{w}^p$, π^b, π^u and π^p : basis functions for the $\boldsymbol{v}$, $\boldsymbol{u}$,p, ρ_b, ρ_u and ρ_p spaces respectively.
— $\boldsymbol{A} : \boldsymbol{B} = \sum_{ij} A_{ij} B_{ij}$

When the corresponding finite element space is discontinuous, additional quantities must be defined. Let F be the shared edge between the adjacent triangles T_1 and T_2. Then :
— h_F : length of F.
— $\hat{\boldsymbol{n}}_F$: normal vector to F.
— $[[g]] = g(T_1) - g(T_2)$: jump discontinuity of g across F.
— $\{\{g\}\} = \frac{1}{2}\left(g(T_1) + g(T_2)\right)$: average of g across F.

A.2 Weak formulation of the flow equations

After multiplying Eqs. II.16 in the main text by their respective basis functions, and integrating over the whole embryo, we get the following equations to solve by our finite element scheme :

$$\eta \int_\Omega (\nabla \boldsymbol{v}) : (\nabla \boldsymbol{w}^v) - \int_\Omega p(\nabla \cdot \boldsymbol{w}^v) + \Gamma \int_\Omega (\boldsymbol{v} - \boldsymbol{u}) \cdot \boldsymbol{w}^v = 0 \ , \tag{A.1}$$

$$\eta_s \int_\Omega (\nabla \boldsymbol{u}) : (\nabla \boldsymbol{w}^u) + \mathcal{C}(\eta_s, \eta_b, \boldsymbol{u}, \boldsymbol{w}^u) + \mathcal{D}(\gamma_n, \boldsymbol{u}, \boldsymbol{w}^u) + \Gamma \int_\Omega (\boldsymbol{u} - \boldsymbol{v}) \cdot \boldsymbol{w}^u$$
$$= -\zeta \int_\Omega \frac{\rho_b}{K_a + \rho_b} (\nabla \cdot \boldsymbol{w}^u) + \int_{\partial\Omega} \Xi(\boldsymbol{w}^u \cdot \hat{\boldsymbol{t}}) \ , \tag{A.2}$$

$$\int_\Omega w^p (\nabla \cdot \boldsymbol{v}) - \gamma_p \int_\Omega p w^p = 0 \ , \tag{A.3}$$

where :

$$\mathcal{C}(\eta_s,\eta_b,\boldsymbol{u},\boldsymbol{w}^u)=\eta_b\int_\Omega(\nabla\cdot\boldsymbol{u})(\nabla\cdot\boldsymbol{w}^u) + \eta_s\int_\Omega\left(\frac{\partial u_y}{\partial x}\frac{\partial w_x^u}{\partial y}+\frac{\partial u_x}{\partial y}\frac{\partial w_y^u}{\partial x}-\frac{\partial u_y}{\partial y}\frac{\partial w_x^u}{\partial x}-\frac{\partial u_x}{\partial x}\frac{\partial w_y^u}{\partial y}\right) \quad (A.4)$$

arises from the gel compressibility, and :

$$\mathcal{D}(\gamma_n,\boldsymbol{u},\boldsymbol{w}^u)=\gamma_n\int_{\partial\Omega}(\boldsymbol{u}\cdot\hat{\boldsymbol{n}})(\boldsymbol{w}^u\cdot\hat{\boldsymbol{n}})-\int_{\partial\Omega}(\hat{\boldsymbol{n}}^T\boldsymbol{\sigma}^d[\boldsymbol{u}]\hat{\boldsymbol{n}})(\boldsymbol{w}^u\cdot\hat{\boldsymbol{n}})-\int_{\partial\Omega}(\hat{\boldsymbol{n}}^T\boldsymbol{\sigma}^d[\boldsymbol{w}^u]\hat{\boldsymbol{n}})(\boldsymbol{u}\cdot\hat{\boldsymbol{n}}) \quad (A.5)$$

is an extra term that enforces the no-penetration boundary condition via penalization (Symmetric Nitsche's method). We chose $\gamma_n = 10^7$. $\gamma_p = 10^{-10}$ is a small term that ensures the algorithm converges to a well-defined pressure.

A.3 Weak formulation of the myosin continuity equations

$$\left(\frac{1}{\Delta t}+k_u\right)\int_\Omega\rho_b^{n+1}\pi^b+\mathcal{A}(D_b,\gamma_g^b,\rho_b^{n+1},\pi^b) = \frac{1}{\Delta t}\int_\Omega\rho_b^n\pi^b+k_b\int_\Omega\rho^n\rho_u^n\pi^b+\frac{3}{2}\mathcal{B}(\rho_b^n,\boldsymbol{u}^n,\pi^b)-\frac{1}{2}\mathcal{B}(\rho_b^{n-1},\boldsymbol{u}^{n-1},\pi^b)\ , \quad (A.6)$$

$$\frac{1}{\Delta t}\int_\Omega\rho_u^{n+1}\pi^u-k_u\int_\Omega\rho_b^{n+1}\pi^u+\mathcal{A}(D_u,\gamma_g^u,\rho_u^{n+1},\pi^u) = \frac{1}{\Delta t}\int_\Omega\rho_u^n\pi^u-k_b\int_\Omega\rho^n\rho_u^n\pi^u+\frac{3}{2}\mathcal{B}(\rho_u^n,\boldsymbol{v}^n,\pi^u)-\frac{1}{2}\mathcal{B}(\rho_u^{n-1},\boldsymbol{v}^{n-1},\pi^u)\ , \quad (A.7)$$

where :

$$\mathcal{A}(D,\gamma,\rho,\pi)=D\int_\Omega(\nabla\rho)\cdot(\nabla\pi)+\gamma D\sum_F\frac{1}{h_F}\int_F[[\rho]][[\pi]] - D\sum_F\int_F(\{\{\nabla\rho\}\}\cdot\boldsymbol{n}_F)[[\pi]]-D\sum_F\int_F[[\rho]](\{\{\nabla\pi\}\}\cdot\boldsymbol{n}_F) \quad (A.8)$$

is the diffusion term, including discontinuity penalization, and :

$$\mathcal{B}(\rho,\boldsymbol{u},\pi)=-\int_\omega\nabla\cdot(\rho\boldsymbol{u})\pi+\sum_F\int_F(\boldsymbol{u}\cdot\hat{\boldsymbol{n}}_F)[[\rho]]\{\{\pi\}\}-\frac{1}{2}\sum_F\int_F|\boldsymbol{u}\cdot\hat{\boldsymbol{n}}_F|[[\rho]][[\pi]] \quad (A.9)$$

is the advection term, including penalization and upwinding.

We chose $\gamma_g^b = 5\times10^2$ and $\gamma_g^u = 5\times10^3$ as the discontinuous jump penalty coefficients for ρ_b and ρ_u respectively.

After calculating ρ_b^{n+1} and ρ_b^{n+1}, a 2-D limiter (modified *minmod*) is applied as described in [189]. The parameters chosen in our case were $M = 5\times10^{-1}$ for the limiter curvature cutoff, and $\theta = 1$ as its comparison parameter.

A.4 Weak formulation of the Bicoid continuity equation

$$\left(\frac{1}{\Delta t}+\frac{1}{\tau}\right)\int_\Omega \rho_p^{n+1}\pi^p + \mathcal{A}(D_p,\gamma_g^p,\rho_p^{n+1},\pi^p) = \frac{1}{\Delta t}\int_\Omega \rho_p^n\pi^p + \mathcal{B}(\rho_p^n,\boldsymbol{v}^n,\pi^p) + k_m\int_\Omega \rho_m^n\pi^p \ , \tag{A.10}$$

where we chose $\gamma_g^p = 5\times 10^3$.

A.5 PP1 time dependence

g(t) was chosen heuristically by analyzing the oscillations in the Cdk1/PP1 reporter. We decided to model it as a slanted sine wave, quickly increasing from 0 to 1 at the mitotic exit, and then slowly decreasing back to 0. The period of these oscillations has been fixed to $T =$ 8 min, in accordance with the duration of the cell cycle at the early stages of development. The slanted sine wave has been defined as a weighted sum of sine functions, with the explicit form defined as :

$$g(t) = g_0 + \frac{15}{32}\sin\left(\frac{2\pi(t-t_0)}{T}\right) + \frac{3}{32}\sin\left(\frac{4\pi(t-t_0)}{T}\right) + \frac{1}{96}\sin\left(\frac{6\pi(t-t_0)}{T}\right) \ , \tag{A.11}$$

where g_0 is such that $g(0) = 0$ and $t_0 = 0.192T$.

A.6 A simplified model for the actomyosin concentration dynamics

The same qualitative features as the myosin dynamics in Fig. 6 of the main text are obtained in the following simplified one-dimensional model. A constant unit concentration of scalar θ_u is present in the negative half-line in the unbound u form. Particles are reflected at the origin (meant to represent the cortex), i.e., reflecting boundary conditions are imposed there. At the origin, the scalar can interconvert between the u and the b forms at rates $k\theta_u(0)$ and θ_b/τ.

During an initial phase of accumulation at the cortex, a constant velocity V is present in the positive direction, which dominates diffusion and replenishes the amount that is converted into the b form at the origin. The solution in this first phase is calculated easily, unit for all the positions but the origin. The equations for the values at the origin (unbound and bound, respectively) are

$$\dot{\theta_0} = -k\theta_0 + V + \frac{\phi_0}{\tau}\,; \qquad \dot{\phi_0} = k\theta_0 - \frac{\phi_0}{\tau}\,, \tag{A.12}$$

where we have already used that $\theta_{-1} = 1$. With $V = 0$, the values settle to $\theta_0 = 1$ and $\phi_0 = k\tau$, which are approached exponentially with rate $(1+k\tau)/\tau$. In the presence of V, there is a pile-up and both values go up in time as $Vt/(1+k\tau)$ and $Vtk\tau/(1+k\tau)$.

The above process keeps going on until the cell cycle gets to its end when the flow V and the attachment rate k vanish. During this second phase of movement, the bound scalar at the

origin is released and diffuses back toward the bulk. The re-injection rate is $ke^{-t/\tau} = \phi_0(t)/\tau$, where t is counted from the beginning of this second phase. The time profile at a distance x from the cortex is then proportional to $e^{-t/\tau} \int_0^t G(x,s)e^{s/\tau}\, ds$ where $G(x,s)$ is the diffusive propagator at distance x and time s with reflecting boundary conditions at the origin. The latter is calculated by the method of images [190], and, since the source is located close to the reflecting boundary, $G(x,s)$ is essentially the diffusive propagator if x is not small. We can finally calculate the above time profile and check that it has a structure similar to Fig. 6 in the main text with peaks that are shifted later and later in time as the distance to the cortex increases.

TABLE A.1 *Model parameters*

Parameter	Notation	Value
Sol viscosity	η	$1.0 \times 10^{-3}\,\mathrm{Pa\,s}$
Gel shear viscosity	η_s	$1.0\,\mathrm{Pa\,s}$
Gel bulk viscosity	η_b	$1.0\,\mathrm{Pa\,s}$
Sol-gel friction	Γ	$2.2 \times 10^{-5}\,\mathrm{Pas/\mu m^2}$
Gel contraction strength	ζ	$1.42 \times 10^{1}\,\mathrm{Pa}$
Gel contraction bound myosin-II capacity	K_a	1
PP1 decay length	λ	$30\,\mu\mathrm{m}$
Rho-GEF decay length	μ	$8\,\mu\mathrm{m}$
PP1 oscillation period	T	$8\,\mathrm{min}$
Bound myosin-II diffusion constant	D_b	$1.67 \times 10^{-1}\,\mu\mathrm{m^2/s}$
Unbound myosin-II diffusion constant	D_u	$1.67 \times 10^{1}\,\mu\mathrm{m^2/s}$
Myosin-II binding constant	k_b	$6.67 \times 10^{-1}\,\mathrm{s^{-1}}$
Myosin-II unbinding rate	k_u	$8.33 \times 10^{-1}\,\mathrm{s^{-1}}$
Intermediate field delay	τ	$7.5 \times 10^{-1}\,\mathrm{min}$
Intermediate field activation PP1 capacity	K_p	5
Minimum microtubule length	$\ell_{\min}$	$1\,\mu\mathrm{m}$
Microtubule growth factor	β	10^{-2}
Cortex-bound actin elastic constant	k_e	$6.67 \times 10^{-6}\,\mathrm{Pa/\mu m}$
Actin-cortex binding rate	k_c	$4\,\mathrm{min}^{-}1$
Actin-cortex binding persistence time	τ_c	$4\,\mathrm{min}$
Bicoid decay time	τ_p	$60\,\mathrm{min}$
Bicoid production rate	k_m	$1.67 \times 10^{-4}\,\mathrm{s^{-1}}$
Bicoid production decay length	μ_m	$25\,\mu\mathrm{m}$
Bicoid diffusion constant	D_p	$5\,\mu\mathrm{m^2/s}$

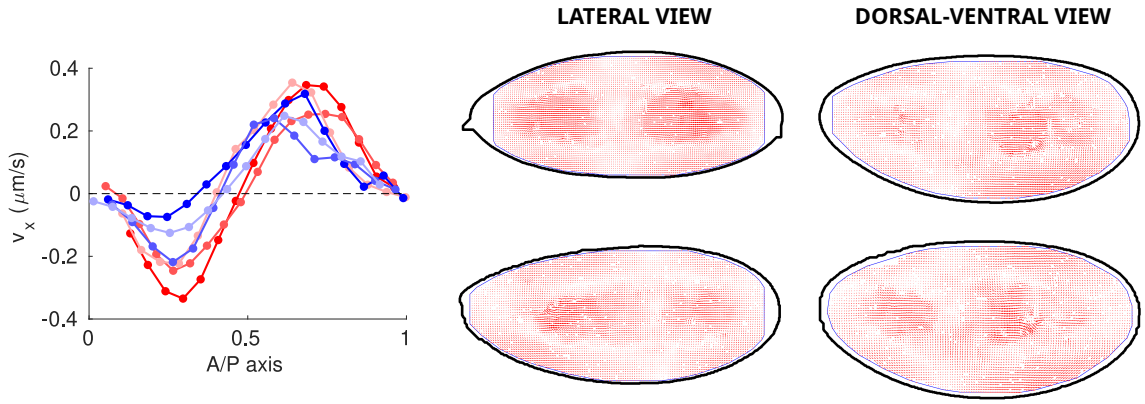

FIG. A.1 **Experiments reveal the axial symmetry of the flows.** *Left : x velocity component of the bulk flows at the cycle 6 contraction peak, averaged over a* 50 µm *strip at the egg center for 6 different embryos. Red/blue curves correspond to measurements on the lateral/DV side, corresponding to quasi-orthogonal planes. Variability can be attributed to differences in embryo sizes and nuclear positioning at cycle 6. Center/Right : Vector plots of the bulk flows at the cycle 6 contraction peak for eggs that have been imaged from the lateral/DV side.*

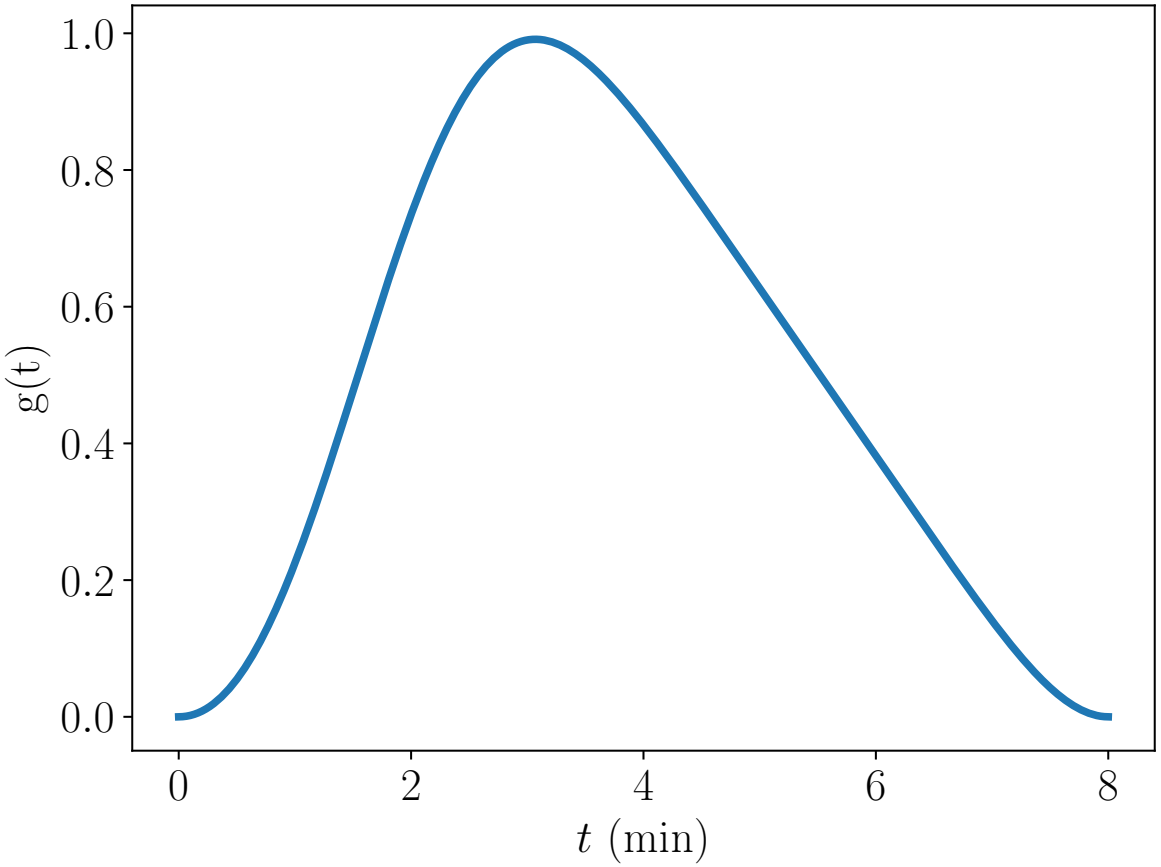

FIG. A.2 *Time dependence of PP1 concentration over time given by Eq. A.11 for a single cycle.*

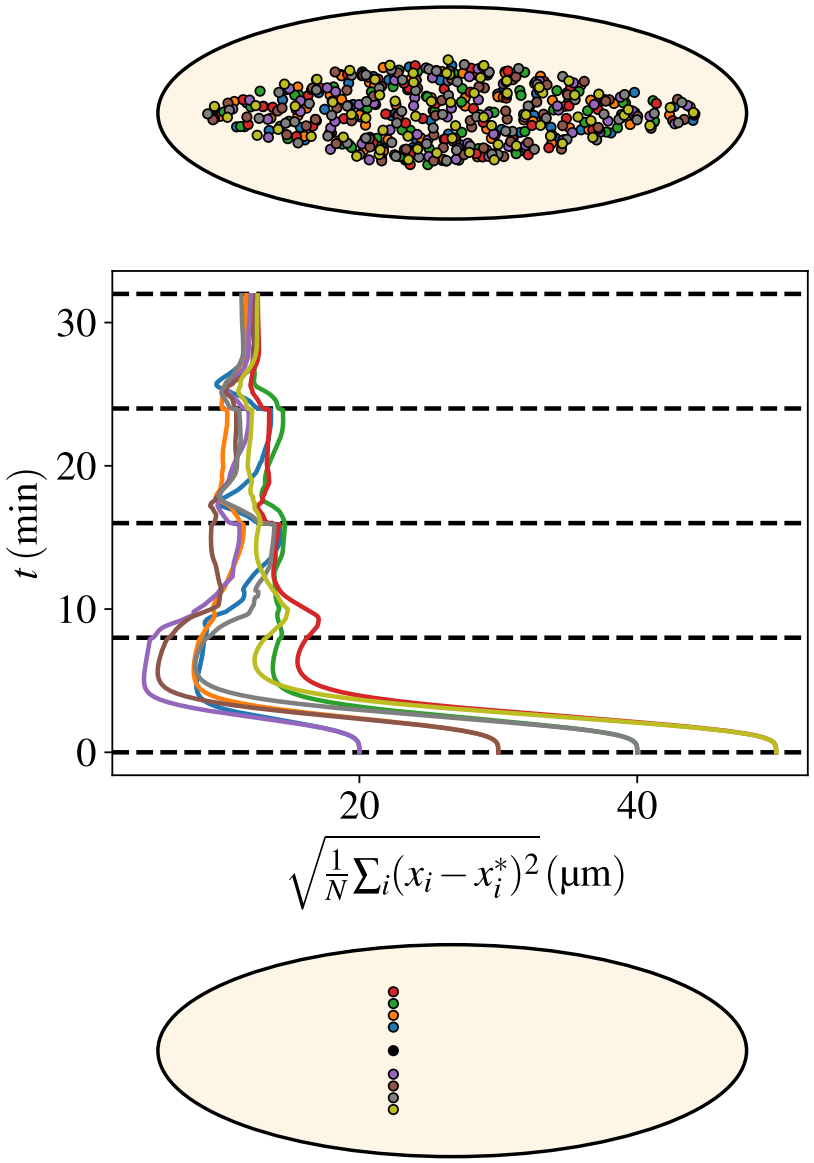

FIG. A.3 **Flows ensure a uniform distribution of nuclei along the AP embryonic axis irrespective of the initial nucleus' distance to it.** *Bottom : A series of positions (coded by different colors) for the first nucleus that starts the division cycles. The nine different locations consider the reference configuration at the embryo AP axis, and four pairs displaced* 20 µm *to* 50 µm *away from said axis. Middle : The evolution in time (flowing upwards) of the distance with respect to the reference configuration. Distance is defined and calculated as in Fig. 7 of the main text. The colors of the curves correspond to the initial positions in the bottom panel. Top : The final configurations of nuclei (for the whole ensemble of colors). Note that all colors are mixed up, witnessing the self-correcting nature of the AP spreading process. That is shown more quantitatively by the middle curves, which all reduce to values corresponding to distances of a few microns distance between pairs of nuclei of the various configurations.*

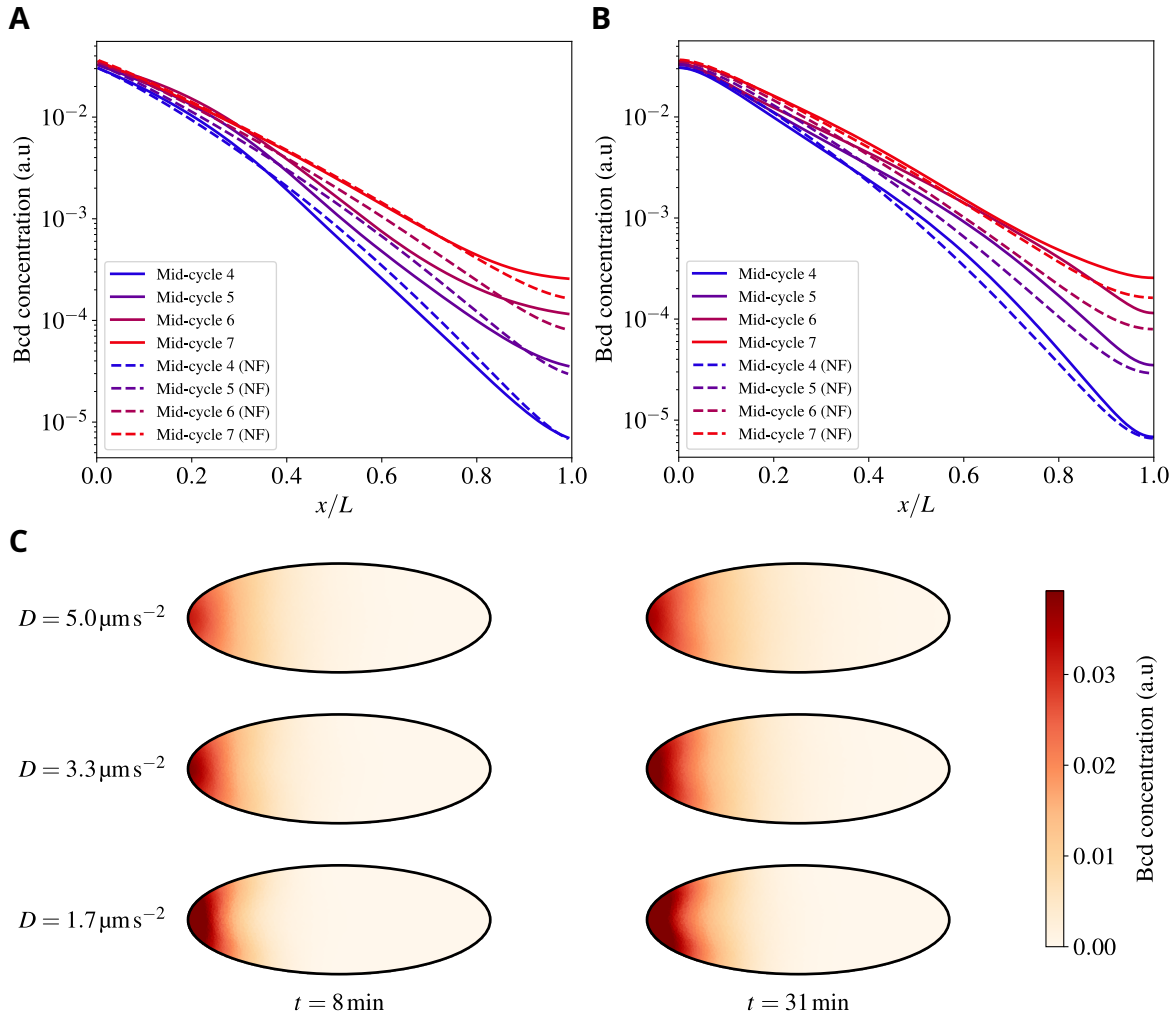

FIG. A.4 **Embryonic cytoplasmic flows weakly affect the establishment of the Bicoid morphogenetic gradient.** *A)-B) Mid-embryo (A) and cortical (B) Bicoid concentrations vs the (normalized) position along the AP axis for various cycles, as indicated in the color legend. NF stands for "No Flow", i.e., situations where cytoplasmic flows were suppressed. C) Heatmaps showing the Bicoid concentration field at two different times after fertilization and three different Bicoid diffusivities.*

B – Chapter III Appendix

B.1 Actomyosin instability-driven flow : Half-space

We have the following system of equations describing the gel velocity field u in a thin strip and the bound myosin concentration ρ_b along said strip :

$$\eta_c \frac{\partial^2 u}{\partial x^2} + \alpha \frac{\partial \rho_b}{\partial x} = \gamma u \ , \tag{B.1}$$

$$\frac{\partial \rho_b}{\partial t} + \frac{\partial}{\partial x}\left(u\rho_b\right) = D_b \frac{\partial^2 \rho_b}{\partial x^2} + k_\mathrm{b} - k_\mathrm{u}\rho_b \ , \tag{B.2}$$

where we have assumed that the unbound myosin concentration does not change significantly.

Let us start from a completely homogeneous situation, with $u = 0$ and $\rho_b = \rho_b^0 = k_b/k_u$. We may then introduce a perturbation such that :

$$u = \delta u e^{\sigma t + iqx} \ , \tag{B.3}$$

$$\rho_b = \rho_b^0 + \delta\rho_b e^{\sigma t + iqx} \ , \tag{B.4}$$

and replacing in Eqs. B.1,B.2 :

$$-q^2\eta_c\delta u + iq\alpha\delta\rho_b = \gamma\delta u \ , \tag{B.5}$$

$$\sigma\delta\rho_b + iq\rho_b^0\delta u = -q^2 D_b\delta\rho_b - k_u\delta\rho_b \ . \tag{B.6}$$

This is essentially a matrix-vector system of equations to find δu and $\delta\rho_b$. We may note that it is homogeneous, hence, if the matrix of coefficients is invertible, the only solution to this system is the zero vector. Hence, there must be a functional relationship between σ and q such that the matrix is not invertible, and that relationship is the dispersion relation. Finding it requires that the determinant of the matrix be zero :

$$\begin{vmatrix} -q^2\eta_c - \gamma & iq\alpha \\ iq\rho_b^0 & \sigma + k_u + q^2 D_b \end{vmatrix} = 0 \ , \tag{B.7}$$

and the dispersion relation :

$$(q^2\eta_c + \gamma)\sigma = q^2\alpha\rho_b^0 - (q^2\eta_c + \gamma)(q^2 D_b + k_u) \ , \tag{B.8}$$

or, written in a more suggestive way :

$$\frac{\sigma}{k_u} = \frac{\alpha\rho_b^0}{\eta_c k_u}\frac{q^2\frac{\eta_c}{\gamma}}{q^2\frac{\eta_c}{\gamma}+1} - \left(q^2\frac{D_b}{k_u}+1\right) \ . \tag{B.9}$$

We can see that the typical unbinding time k_u^{-1} is a relevant timescale, whereas the hydrodynamical length $\sqrt{\frac{\eta_c}{\gamma}}$ and the bound myosin diffusion length $\sqrt{\frac{D_b}{k_u}}$ are the relevant lengthscales in the problem. First, we will nondimensionalize time by taking $t \to k_u^{-1}t$. Given that the chemical kinetics are typically easier parameters to measure and control, we will nondimensionalize space by taking $x \to \sqrt{\frac{\eta_c}{\gamma}}x$. Then, in nondimensional units :

$$\sigma(q) = \Pi_\alpha^2\frac{q^2}{1+q^2} - \left(q^2\Pi_D^2+1\right) \ , \tag{B.10}$$

where $\Pi_\alpha^2 = \frac{\alpha\rho_b^0}{\eta_c k_u}$ is the ratio between active and viscous forces, and $\Pi_D = \sqrt{\frac{\gamma}{\eta_c}}\sqrt{\frac{D_b}{k_u}}$ is the ratio between the diffusion length of bound myosin and the hydrodynamical length. We can find the extrema of this function by taking the first derivative, and in particular, the maxima are located at :

$$(q^*)^2 = \begin{cases} \frac{\Pi_\alpha}{\Pi_D} - 1 & \text{if } \Pi_\alpha \geq \Pi_D \\ 0 & \text{if } \Pi_\alpha < \Pi_D \ , \end{cases} \tag{B.11}$$

with values :

$$\sigma^* = \begin{cases} (\Pi_\alpha - \Pi_D)^2 - 1 & \text{if } \Pi_\alpha \geq \Pi_D \\ -1 & \text{if } \Pi_\alpha < \Pi_D \ . \end{cases} \tag{B.12}$$

When the instability is triggered, we can calculate the flow profile. Let us recover dimensional units now. Assuming that enough time has passed, i.e $t \gg \frac{1}{\sigma[q]}$, then we can take the saddle point approximation and consider :

$$u = u_0\cos(q^*x) \tag{B.13}$$

for $q^* > 0$.

The sol satisfies :

$$\Delta\omega = 0 \ . \tag{B.14}$$

The continuous-stress boundary condition at the interface between the sol and the gel enforces :

$$\eta\omega\Big|_{y=0} = -\eta_c\frac{u}{h} \ , \tag{B.15}$$

such that :

$$\omega = -\frac{\eta_c}{\eta}\frac{u_0}{h}\cos(q^*x)e^{-q^*y} \ . \tag{B.16}$$

Now, to find the stream function we must solve :

$$\Delta\psi = -\omega \ , \tag{B.17}$$

subject to no-penetration boundary conditions at the sol-gel interface :

$$\left.\frac{\partial\psi}{\partial y}\right|_{y=0} = 0 \ . \tag{B.18}$$

Then :

$$\psi = \frac{\eta_c}{\eta}\frac{u_0}{h}\cos(q^*x)\frac{y}{2q^*}e^{-q^*y} \ . \tag{B.19}$$

B.2 Actomyosin instability-driven flow : Circular arena

Our equations are :

$$\eta_c\frac{1}{R^2}\frac{\partial^2 u}{\partial\theta^2} - \eta_c\frac{1}{R^2}u + \frac{\alpha}{R}\frac{\partial\rho_b}{\partial\theta} = \gamma u \ , \tag{B.20}$$

$$\frac{\partial\rho_b}{\partial t} + \frac{1}{R}\frac{\partial}{\partial\theta}(u\rho_b) = D_b\frac{1}{R^2}\frac{\partial^2\rho_b}{\partial\theta^2} - D_b\frac{1}{R^2}\rho_b + k_b - k_u\rho_b \ , \tag{B.21}$$

and our perturbed state is :

$$u = \delta u e^{\sigma t + in\theta} \ , \tag{B.22}$$

$$\rho_b = \rho_b^0 + \delta\rho_b e^{\sigma t + in\theta} \ , \tag{B.23}$$

where the 2π symmetry in θ forces n to be an integer. Then :

$$-\frac{1}{R^2}n^2\eta_c\delta u - \eta_c\frac{1}{R^2}\delta u + in\frac{\alpha}{R}\delta\rho_b = \gamma\delta u \ , \tag{B.24}$$

$$\sigma\delta\rho_b + in\frac{1}{R}\rho_b^0\delta u = -D_b\frac{1}{R^2}n^2\delta\rho_b - D_b\frac{1}{R^2}\delta\rho_b - k_u\rho_b \ . \tag{B.25}$$

To find the dispersion relation :

$$\begin{vmatrix} -n^2\eta_c - \eta_c - R^2\gamma & inR\alpha \\ inR\rho_b^0 & R^2\sigma + n^2D_b + D_b + R^2k_u \end{vmatrix} = 0 \ , \tag{B.26}$$

hence :

$$(\eta_c(n^2+1) + R^2\gamma)R^2\sigma = n^2R^2\alpha\rho_b^0 - (\eta_c(n^2+1) + R^2\gamma)(D_b(n^2+1) + R^2k_u) \ . \tag{B.27}$$

Written in a more suggestive way :

$$\frac{\sigma}{k_u} = \frac{\alpha\rho_b^0}{\eta_c k_u}\frac{\frac{\eta_c}{\eta_c+R^2\gamma}n^2}{\frac{\eta_c}{\eta_c+R^2\gamma}n^2+1} - \left(\frac{1}{R^2}\frac{D_b}{k_u}n^2 + \left(\frac{1}{R^2}\frac{D_b}{k_u}+1\right)\right) \ . \tag{B.28}$$

As in the previous case, we will rescale time as $t \to k_u^{-1}t$. We will also introduce a new variable $q = \sqrt{\frac{\eta_c}{\eta_c+R^2\gamma}}n$. In this way, we can compare the form of this function to the infinite strip case. Written in terms of q :

$$\sigma = \frac{\alpha\rho_b^0}{\eta_c k_u}\frac{q^2}{q^2+1} - \left(\left(\frac{1}{R^2}\frac{D_b}{k_u} + \frac{D_b}{k_u}\frac{\gamma}{\eta_c}\right)q^2 + \left(\frac{1}{R^2}\frac{D_b}{k_u}+1\right)\right) \ . \tag{B.29}$$

We can introduce the same nondimensional parameters as before, in addition to $\Pi_R = \frac{1}{R}\sqrt{\frac{D_b}{k_u}}$, which is the ratio between the diffusion length of bound myosin and the radius of the ring. Then :

$$\sigma(q) = \Pi_\alpha^2 \frac{q^2}{1+q^2} - \left(\left(\Pi_D^2 + \Pi_R^2\right) q^2 + \Pi_R^2 + 1\right) \ , \tag{B.30}$$

which peaks at :

$$(q^*)^2 = \begin{cases} \sqrt{\frac{\Pi_\alpha^2}{\Pi_D^2+\Pi_R^2}} - 1 & \text{if } \Pi_\alpha^2 \geq \Pi_D^2 + \Pi_R^2 \\ 0 & \text{if } \Pi_\alpha^2 < \Pi_D^2 + \Pi_R^2 \ , \end{cases} \tag{B.31}$$

with values :

$$\sigma^* = \begin{cases} \Pi_\alpha^2 + \Pi_D^2 - 2\Pi_\alpha\sqrt{\Pi_D^2 + \Pi_R^2} - 1 & \text{if } \Pi_\alpha^2 \geq \Pi_D^2 + \Pi_R^2 \\ -\left(\Pi_R^2 + 1\right) & \text{if } \Pi_\alpha^2 < \Pi_D^2 + \Pi_R^2 \ . \end{cases} \tag{B.32}$$

Now to calculate the flow, we make use of the same saddle point approximation. The sol-gel interface is located at $r = R$. Recovering dimensional units, the gel velocity in the ring is :

$$u = u_0 \cos(n^*\theta) \tag{B.33}$$

for $n^* > 0$, and the sol in the bulk satisfies :

$$\Delta\omega = 0 \ . \tag{B.34}$$

Stress-matching boundary conditions require :

$$\eta_c \frac{u}{h} = \eta\omega\Big|_{r=R} \ , \tag{B.35}$$

and as such :

$$\omega = -\frac{\eta_c}{\eta}\frac{u_0}{h}\left(\frac{r}{R}\right)^{n^*} \cos(n^*\theta) \ . \tag{B.36}$$

The stream function satisfies :

$$\Delta\psi = -\omega \ , \tag{B.37}$$

subject to no-penetration at the sol-gel interface :

$$\psi\Big|_{r=R} = 0 \ . \tag{B.38}$$

Then :

$$\psi = \frac{1}{4(n^*+1)}\frac{\eta_c}{\eta}\frac{u_0}{h}\left(\frac{r}{R}\right)^{n^*}\left(r^2 - R^2\right)\cos(n^*\theta) \ . \tag{B.39}$$

B.3 Nuclei-driven flow : Half-space

We consider a nucleus at position $(x_i, 0)$ next to an infinite gel strip parallel to the y axis. The sol-gel interface is located at $x = 0$. The gel equation reads :

$$\frac{\partial^2 u}{\partial y^2} - \kappa_c^2 u = -\frac{\alpha}{\eta_c}\frac{\partial \rho_b}{\partial y} \ , \tag{B.40}$$

where $\kappa_c^{-1} = \sqrt{\frac{\eta_c}{\gamma}}$ is the hydrodynamical length.

Taking the Fourier transform :

$$-k^2\hat{u}(k) - \kappa_c^2\hat{u}(k) = -i\frac{\alpha}{\eta_c}k\hat{\rho}_b(k) \ , \tag{B.41}$$

where, assuming that $x_i > \lambda$, we can make a Gaussian approximation of the bound myosin concentration : :

$$\rho_b = g(t)e^{-\sqrt{y^2+x_i^2}/\lambda} \approx g(t)e^{-x_i/\lambda}e^{-y^2/(2\lambda x_i)} \ , \tag{B.42}$$

where $g(t)$ is the PP1 activation function, such that :

$$\hat{\rho}_b = g(t)\sqrt{\lambda x_i}e^{-x_i/\lambda}e^{-\frac{1}{2}\left(\sqrt{\lambda x_i}k\right)^2} \ . \tag{B.43}$$

Then :

$$\hat{u} = i\frac{\alpha}{\eta_c}g(t)\sqrt{\lambda x_i}e^{-x_i/\lambda}\frac{k}{k^2+\kappa_c^2}e^{-\frac{1}{2}\left(\sqrt{\lambda x_i}k\right)^2} \ . \tag{B.44}$$

From the continuous stress boundary condition :

$$\hat{\omega}(0,k) = -\frac{\eta_c}{\eta}\frac{\hat{u}}{h} \ , \tag{B.45}$$

and :

$$\hat{\omega}(x,k) = -\frac{\eta_c}{\eta}\frac{\hat{u}}{h}e^{-|k|x} \ . \tag{B.46}$$

Also :

$$\hat{\psi}(x,k) = -\operatorname{sign}(k)\frac{x}{2k}\frac{\eta_c}{\eta}\frac{\hat{u}}{h}e^{-|k|x} \ . \tag{B.47}$$

It is also of interest to calculate the saddle point expansion of $\frac{\hat{u}(k)}{k}$. Let :

$$\mathcal{L}(k) = \frac{1}{2}\left(\sqrt{\lambda x_i}k\right)^2 + \log\left(k^2+\kappa_c^2\right) \ , \tag{B.48}$$

then :

$$\frac{\hat{u}(k)}{k} \approx i\frac{\alpha}{\eta_c}g(t)\sqrt{\lambda x_i}e^{-x_i/\lambda}e^{-\mathcal{L}(0)}e^{-\frac{1}{2}\mathcal{L}''(0)k^2} \ , \tag{B.49}$$

where $\mathcal{L}(0) = \log\left(\kappa_c^2\right)$ and $\mathcal{L}''(0) = \left(\lambda x_i + \frac{2}{\kappa_c^2}\right)$.

Then, we can calculate the rest of the quantities of interest. In particular, we can calculate the stream function :

$$\psi(x,y) = -\frac{\alpha}{\eta} g(t) \sqrt{\frac{\lambda x_i}{\lambda x_i + 2/\kappa_c^2}} e^{-x_i/\lambda} \frac{x}{2h\kappa_c^2} \Im\left(e^{\frac{(x+iy)^2}{2(\lambda x_i + 2/\kappa_c^2)}} \operatorname{erfc}\left(\frac{x+iy}{\sqrt{2\left(\lambda x_i + 2/\kappa_c^2\right)}} \right) \right) , \tag{B.50}$$

from which we can calculate the velocity profile in the cytosol. In particular, at the position of the nucleus :

$$\frac{\mathrm{d}x_i}{\mathrm{d}t} = \frac{\alpha}{\eta} g(t) \frac{\sqrt{\lambda x_i}}{\lambda x_i + 2/\kappa_c^2} e^{-x_i/\lambda} \frac{x_i}{2h\kappa_c^2} \left(\sqrt{\frac{2}{\pi}} - \frac{x_i}{\sqrt{\lambda x_i + 2/\kappa_c^2}} e^{\frac{x_i^2}{2(\lambda x_i + 2/\kappa_c^2)}} \operatorname{erfc}\left(\frac{x_i}{\sqrt{2\left(\lambda x_i + 2/\kappa_c^2\right)}} \right) \right) . \tag{B.51}$$

B.4 Nuclei-driven flow : Channel

Consider a nucleus at $(x_i, 0)$, between two cortical strips parallel to the y axis. The sol-gel interfaces are located at $x = 0$ and $x = L$. In the bulk, the vorticity satisfies :

$$\Delta\omega = 0 , \tag{B.52}$$

and considering the Fourier transform in y :

$$\frac{\partial^2 \hat{\omega}}{\partial^2 x} - k^2 \hat{\omega} = 0 , \tag{B.53}$$

subject to stress-matching boundary conditions at each interface :

$$\hat{\omega}\Big|_{x=0} = -\frac{\eta_c}{\eta} \frac{\hat{u}^0}{h} \tag{B.54}$$

$$\hat{\omega}\Big|_{x=L} = \frac{\eta_c}{\eta} \frac{\hat{u}^L}{h} , \tag{B.55}$$

where :

$$\hat{u}^0 = i \frac{\alpha}{\eta_c} g(t) \sqrt{\lambda x_i} e^{-x_i/\lambda} \frac{k}{k^2 + \kappa_c^2} e^{-\frac{1}{2}\left(\sqrt{\lambda x_i} k\right)^2} , \tag{B.56}$$

$$\hat{u}^L = i \frac{\alpha}{\eta_c} g(t) \sqrt{\lambda (L - x_i)} e^{-(L-x_i)/\lambda} \frac{k}{k^2 + \kappa_c^2} e^{-\frac{1}{2}\left(\sqrt{\lambda (L-x_i)} k\right)^2} . \tag{B.57}$$

The solution reads :

$$\hat{\omega} = \frac{\eta_c}{\eta} \operatorname{csch}(kL) \left(\frac{\hat{u}^L}{h} \sinh(kx) - \frac{\hat{u}^0}{h} \sinh(k(L-x)) \right) . \tag{B.58}$$

And the stream function, considering the no-penetration boundary condition at the sol-gel interfaces :

$$\begin{aligned} \hat{\psi} = \frac{1}{2k} \frac{\eta_c}{\eta} \operatorname{csch}(kL) \Bigg(& - \left(\frac{\hat{u}^L}{h} + \frac{\hat{u}^0}{h} \cosh(kL) \right) x \cosh(kx) \\ & + \left(\coth(kL) \left(\frac{\hat{u}^0}{h} + \frac{\hat{u}^L}{h} \cosh(kL) \right) L - \frac{\hat{u}^L}{h} (L-x) \sinh(kL) \right) \sinh(kx) \Bigg) . \end{aligned} \tag{B.59}$$

For a fixed value of x, this function of k has two pairs of antisymmetric peaks around zero that vary in strength as a function of x. Further analysis reveals that this function can be decomposed into the contribution from each parallel strip (i.e. separating the x and $L-x$ components), and these can be approximated as :

$$\hat{\psi} = ik\left(f_1(x)e^{-\frac{1}{2}\varphi_1(x)k^2} + f_2(x)e^{-\frac{1}{2}\varphi_2(x)k^2}\right) , \tag{B.60}$$

where :

$$f_1(x) = \frac{\frac{\alpha}{\eta_c}g(t)}{2h}\frac{\eta_c}{\eta}\sqrt{\lambda x_i}e^{-x_i/\lambda}x\frac{-2L^2+3Lx-x^2}{3L\kappa_c^2} , \tag{B.61}$$

$$f_2(x) = \frac{\frac{\alpha}{\eta_c}g(t)}{2h}\frac{\eta_c}{\eta}\sqrt{\lambda(L-x_i)}e^{-(L-x_i)/\lambda}x\frac{L^2-x^2}{3L\kappa_c^2} , \tag{B.62}$$

$$\varphi_1(x) = \frac{2}{\kappa_c^2} + \frac{14}{30}L^2 - \frac{1}{5}(L-x)^2 + x_i\lambda , \tag{B.63}$$

$$\varphi_2(x) = \frac{2}{\kappa_c^2} + \frac{14}{30}L^2 - \frac{1}{5}x^2 + (L-x_i)\lambda . \tag{B.64}$$

The inverse Fourier transform yields :

$$\psi = -\left(\frac{f_1(x)}{\varphi_1(x)^{3/2}}e^{-\frac{1}{2}\frac{y^2}{\varphi_1(x)}} + \frac{f_2(x)}{\varphi_2(x)^{3/2}}e^{-\frac{1}{2}\frac{y^2}{\varphi_2(x)}}\right)y , \tag{B.65}$$

which readily generalizes to the case of multiple nuclei :

$$\psi = -\sum_i\left(\frac{f_{1,i}(x)}{\varphi_{1,i}(x)^{3/2}}e^{-\frac{1}{2}\frac{(y-y_i)^2}{\varphi_{1,i}(x)}} + \frac{f_{2,i}(x)}{\varphi_{2,i}(x)^{3/2}}e^{-\frac{1}{2}\frac{(y-y_i)^2}{\varphi_{2,i}(x)}}\right)(y-y_i) . \tag{B.66}$$

B.5 Nuclei-driven flow : Circular arena

Consider a nucleus placed in a circular arena at (polar) coordinates (r_i, θ_i). The sol-gel interface is located at $r = R$. The sol vorticity can be found from the Laplace equation in a circular domain :

$$\omega = A_0 + \sum_{n=1} r^n\left(A_n\sin(n\theta) + B_n\cos(n\theta)\right) , \tag{B.67}$$

while the gel satisfies :

$$\frac{\partial^2 u}{\partial\theta^2} - \left(1 + R^2\frac{\gamma}{\eta_c}\right)u = -R\frac{\alpha}{\eta_c}\frac{\partial\rho_b}{\partial\theta} . \tag{B.68}$$

We can expand the bound myosin distribution assuming that $\frac{r_i}{R} \ll 1$

$$\rho_b = g(t)e^{-\sqrt{(y-y_i)^2+(x-x_i)^2}/\lambda} = e^{-\sqrt{R^2+r_i^2-2Rr_i\cos(\theta-\theta_i)}/\lambda} \tag{B.69}$$

$$\approx g(t)e^{-\frac{R}{\lambda}}\left(1 + \frac{R}{\lambda}\frac{r_i}{R}\cos(\theta-\theta_i) + \frac{1}{2}\frac{R}{\lambda}\left(\frac{r_i}{R}\right)^2\left(-1 + \left(\frac{R}{\lambda}+1\right)\cos^2(\theta-\theta_i)\right)\right) , \tag{B.70}$$

such that :

$$\frac{\partial \rho_b}{\partial \theta} \approx -g(t)e^{-\frac{R}{\lambda}} \left(\frac{R}{\lambda}\frac{r_i}{R}\sin(\theta-\theta_i) + \frac{R}{\lambda}\left(\frac{r_i}{R}\right)^2 \left(\frac{R}{\lambda}+1\right)\sin(2(\theta-\theta_i)) \right) , \tag{B.71}$$

and finally :

$$u = -\frac{1}{10+7R^2\kappa_c^2+R^4\kappa_c^4} R\frac{\alpha}{\eta_c} g(t)e^{-\frac{R}{\lambda}} \left(\left(5+R^2\kappa_c^2\right)\frac{R}{\lambda}\frac{r_i}{R}\sin(\theta-\theta_i) \right. \\ \left. + \left(2+R^2\kappa_c^2\right)\frac{R}{\lambda}\left(\frac{r_i}{R}\right)^2\left(\frac{R}{\lambda}+1\right)\sin(2(\theta-\theta_i)) \right) , \tag{B.72}$$

which can be rewritten compactly :

$$u = -u_1\left(\frac{r_i}{R}\right)\sin(\theta-\theta_0) - u_2\left(\frac{r_i}{R}\right)^2\sin(2(\theta-\theta_0)) . \tag{B.73}$$

Stress-matching boundary conditions require :

$$\eta_c\frac{u}{h} = \eta\omega(r=R,\theta) \tag{B.74}$$

and as such :

$$\omega = -\frac{1}{h}\frac{\eta_c}{\eta}\left(u_1\left(\frac{r_i}{R}\right)\sin(\theta-\theta_i)\frac{r}{R} + u_2\left(\frac{r_i}{R}\right)^2\sin(2(\theta-\theta_i))\frac{r^2}{R^2} \right) . \tag{B.75}$$

We can see that the resulting flow comes from the contribution of a dipole and a quadrupole vortex profiles.

We will calculate the stream function by dividing it into two parts. First :

$$\Delta\psi_1 = \frac{1}{Rh}\frac{\eta_c}{\eta}u_1\left(\frac{r_i}{R}\right)\sin(\theta-\theta_0)r . \tag{B.76}$$

Defining $\psi_1 = f_1(r)\varphi_1(\theta)$, it is clear that $\varphi_1(\theta) = \sin(\theta-\theta_0)$. Then :

$$f_1'' + \frac{1}{r}f_1' - \frac{1}{r^2}f_1 = \frac{1}{Rh}\frac{\eta_c}{\eta}u_1\left(\frac{r_i}{R}\right)r , \tag{B.77}$$

and :

$$f_1(r) = \frac{1}{8}\frac{1}{Rh}\frac{\eta_c}{\eta}u_1\left(\frac{r_i}{R}\right)r^3 + B_1 r . \tag{B.78}$$

From an analogous procedure, $\varphi_2 = \sin(2(\theta-\theta_0))$, and :

$$f_2(r) = \frac{1}{12}\frac{1}{R^2h}\frac{\eta_c}{\eta}u_2\left(\frac{r_i}{R}\right)^2 r^4 + B_2 r^2 . \tag{B.79}$$

Then :

$$\psi = \left(\frac{1}{8}\frac{1}{Rh}\frac{\eta_c}{\eta}u_1\left(\frac{r_i}{R}\right)r^3 + B_1 r\right)\sin(\theta-\theta_i) + \left(\frac{1}{12}\frac{1}{R^2h}\frac{\eta_c}{\eta}u_2\left(\frac{r_i}{R}\right)^2 r^4 + B_2 r^2\right)\sin(2(\theta-\theta_i)) . \tag{B.80}$$

B_1 and B_2 are fixed by the no-penetration condition :

$$v_r\Big|_{r=R} = \frac{1}{r}\frac{\partial\psi}{\partial\theta}\Big|_{r=R} = 0 \ . \tag{B.81}$$

Then :

$$\psi = \frac{1}{8}\frac{1}{Rh}\frac{\eta_c}{\eta}u_1\left(\frac{r_i}{R}\right)\left(r^3 - R^2 r\right)\sin(\theta-\theta_i) + \frac{1}{12}\frac{1}{R^2 h}\frac{\eta_c}{\eta}u_2\left(\frac{r_i}{R}\right)^2\left(r^4 - R^2 r^2\right)\sin(2(\theta-\theta_i)) \ . \tag{B.82}$$

To determine the centering dynamics of the nucleus, we first calculate the radial velocity :

$$v_r = \frac{1}{8}\frac{1}{Rh}\frac{\eta_c}{\eta}u_1\left(\frac{r_i}{R}\right)\left(r^2 - R^2\right)\cos(\theta-\theta_i) + \frac{1}{6}\frac{1}{R^2 h}\frac{\eta_c}{\eta}u_2\left(\frac{r_i}{R}\right)^2\left(r^3 - R^2 r\right)\cos(2(\theta-\theta_i)) \ . \tag{B.83}$$

Now we evaluate this at the position of the nucleus, i.e $r = r_i$, $\theta = \theta_i$. At the lowest order :

$$\frac{\mathrm{d}r_i}{\mathrm{d}t} = -\frac{1}{\tau}g(t)r_i \ , \tag{B.84}$$

where $\frac{1}{\tau} = \frac{1}{8}\frac{u_1}{h}\frac{\eta_c}{\eta}$.

B.6 Continuous nuclear distribution : Circular arena

We may consider now a distribution of nuclei ρ_n, with the cell cycle being represented in space and time by the function g. Then :

$$\rho_b(\boldsymbol{x},t) = g(t)\int g(\boldsymbol{x}',t)\rho_n(\boldsymbol{x}',t)e^{-\sqrt{(y-y')^2+(x-x')^2}/\lambda}\,\mathrm{d}^2x' \ , \tag{B.85}$$

such that :

$$\rho_b = \left\langle g(\boldsymbol{x}',t)e^{-\sqrt{(y-y')^2+(x-x')^2}/\lambda}\right\rangle \ . \tag{B.86}$$

To simplify our calculations, we will consider that there are no nuclear divisions. We will also ignore the microtubule-mediated nuclei-nuclei interactions. Then, the distribution of nuclei satisfies the continuity equation :

$$\frac{\partial\rho_n}{\partial t} + \nabla\cdot(\boldsymbol{v}\rho_n) = 0 \ , \tag{B.87}$$

where $\boldsymbol{v}$ is the cytosol velocity. We may note that from here on, the equations that we need to solve and their boundary conditions are exactly the same as in the case of the discrete nuclear distribution. The only difference is that instead of summing the contributions of each individual nucleus, we are now integrating over the whole distribution. As a result :

$$\omega = -\frac{1}{h}\frac{\eta_c}{\eta}\left(u_1\frac{r}{R}\left\langle\sin(\theta-\theta')\frac{r'}{R}\right\rangle + u_2\left(\frac{r}{R}\right)^2\left\langle\sin(2(\theta-\theta'))\left(\frac{r'}{R}\right)^2\right\rangle\right) \ , \tag{B.88}$$

and :

$$\psi = \frac{1}{8}\frac{1}{Rh}\frac{\eta_c}{\eta}u_1\left(r^3 - R^2 r\right)\left\langle g(r',\theta',t)\left(\frac{r'}{R}\right)\sin(\theta-\theta')\right\rangle + \frac{1}{12}\frac{1}{R^2 h}\frac{\eta_c}{\eta}u_2\left(r^4 - R^2 r^2\right)\left\langle g(r',\theta',t)\left(\frac{r'}{R}\right)^2\sin(2(\theta-\theta'))\right\rangle \ , \quad \text{(B.89)}$$

such that :

$$\psi = \frac{\chi_1}{R^2}(r^2-R^2)\left[\langle g(r,\theta,t)r\cos(\theta)\rangle\, r\sin(\theta) - \langle g(r,\theta,t)r\sin(\theta)\rangle\, r\cos(\theta)\right] + \frac{\chi_2}{R^2}(r^2-R^2)\left[\left\langle g(r,\theta,t)r^2\cos(2\theta)\right\rangle r^2\sin(2\theta) - \left\langle g(r,\theta,t)r^2\sin(2\theta)\right\rangle r^2\cos(2\theta)\right] \ . \quad \text{(B.90)}$$

In cartesian coordinates :

$$\psi = \frac{\chi_1}{R^2}(r^2-R^2)\left[\langle g(x,y,t)x\rangle\, y - \langle g(x,y,t)y\rangle\, x\right] + \frac{\chi_2}{R^2}(r^2-R^2)\left[\left\langle g(x,y,t)(x^2-y^2)\right\rangle 2xy - \langle g(x,y,t)2xy\rangle\,(x^2-y^2)\right] \ , \quad \text{(B.91)}$$

and at the lowest order of x and y :

$$\psi = -\chi_1\left[\langle g(x,y,t)x\rangle\, y - \langle g(x,y,t)y\rangle\, x\right] - \chi_2\left[\left\langle g(x,y,t)(x^2-y^2)\right\rangle 2xy - \langle g(x,y,t)2xy\rangle\,(x^2-y^2)\right] \ , \quad \text{(B.92)}$$

then :

$$v_x = -\chi_1\langle g(x,y,t)x\rangle - \chi_2\left[\left\langle g(x,y,t)(x^2-y^2)\right\rangle 2x + \langle g(x,y,t)2xy\rangle\, 2y\right] \ , \quad \text{(B.93)}$$

$$v_y = -\chi_1\langle g(x,y,t)y\rangle + \chi_2\left[\left\langle g(x,y,t)(x^2-y^2)\right\rangle 2y - \langle g(x,y,t)2xy\rangle\, 2x\right] \ . \quad \text{(B.94)}$$

Now we can follow the temporal evolution of any spatial dependent quantity as follows :

$$\frac{\mathrm{d}}{\mathrm{d}t}\langle\mathcal{M}\rangle = \int \mathcal{M}\frac{\partial\rho_n}{\partial t}\ \mathrm{d}^2x \quad \text{(B.95)}$$

$$= -\int \mathcal{M}\nabla\cdot(\boldsymbol{v}\rho_n)\ \mathrm{d}^2x \quad \text{(B.96)}$$

$$= \int \rho_n\boldsymbol{v}\cdot\nabla\mathcal{M}\ \mathrm{d}^2x \quad \text{(B.97)}$$

$$= \langle\boldsymbol{v}\cdot\nabla\mathcal{M}\rangle \ , \quad \text{(B.98)}$$

where we have used the divergence theorem, considering that $\boldsymbol{v}\cdot\hat{\boldsymbol{n}} = 0$ at the boundary. In

particular, for the moments of the distribution :

$$\frac{\mathrm{d}}{\mathrm{d}t}\langle x\rangle = -\chi_1 \langle g(x,y,t)x\rangle - 2\chi_2 \left[\left\langle g(x,y,t)(x^2-y^2)\right\rangle \langle x\rangle + \langle g(x,y,t)2xy\rangle \langle y\rangle\right] \ , \tag{B.99}$$

$$\frac{\mathrm{d}}{\mathrm{d}t}\langle y\rangle = -\chi_1 \langle g(x,y,t)y\rangle + 2\chi_2 \left[\left\langle g(x,y,t)(x^2-y^2)\right\rangle \langle y\rangle - \langle g(x,y,t)2xy\rangle \langle x\rangle\right] \ , \tag{B.100}$$

$$\frac{\mathrm{d}}{\mathrm{d}t}\left\langle x^2\right\rangle = -2\chi_1 \langle g(x,y,t)x\rangle \langle x\rangle - 4\chi_2 \left[\left\langle g(x,y,t)(x^2-y^2)\right\rangle \left\langle x^2\right\rangle + \langle g(x,y,t)2xy\rangle \langle xy\rangle\right] \ , \tag{B.101}$$

$$\frac{\mathrm{d}}{\mathrm{d}t}\left\langle y^2\right\rangle = -2\chi_1 \langle g(x,y,t)y\rangle \langle y\rangle + 4\chi_2 \left[\left\langle g(x,y,t)(x^2-y^2)\right\rangle \left\langle y^2\right\rangle - \langle g(x,y,t)2xy\rangle \langle xy\rangle\right] \ . \tag{B.102}$$

If the myosin activation function g is spatially uniform, two clear results emerge from this set of equations. First, when the nuclear distribution is symmetric around its mean, the evolution of the mean satisfies :

$$\frac{\mathrm{d}}{\mathrm{d}t}\langle \boldsymbol{x}\rangle = -g(t)\chi_1 \langle \boldsymbol{x}\rangle \ , \tag{B.103}$$

such that the distribution will become centered over time.

On the other hand, when the nuclear distribution is centered but not symmetric, its moments satisfy :

$$\frac{\mathrm{d}}{\mathrm{d}t}\left\langle x^2-y^2\right\rangle = -4g(t)\chi_2 \left\langle x^2+y^2\right\rangle \left\langle x^2-y^2\right\rangle \ , \tag{B.104}$$

$$\frac{\mathrm{d}}{\mathrm{d}t}\langle xy\rangle = -2g(t)\chi_1 \langle xy\rangle - 4g(t)\chi_2 \left\langle x^2+y^2\right\rangle \langle xy\rangle \ . \tag{B.105}$$

such that the distribution will become symmetric over time.

C – Chapter IV Appendix

C.1 Spatiotemporal dynamics of the twine-degrading protein

Consider the dynamical equation of the concentration of the twine-degrading molecule θ :

$$\frac{\partial \theta}{\partial t} = D\Delta\theta + \alpha_\theta \Theta\left(x + \frac{b}{2}\right)\Theta\left(\frac{b}{2} - x\right) \ , \tag{C.1}$$

where Θ is the Heaviside function. The size of the patch that is actively transcribing is b, and centered at $x = 0$. A formal solution to this equation can be found using the Green's function. To give a sense of the scaling, we will use a Fourier transform, i.e. approximating the bulk of the system. Calculating the Fourier transform in space :

$$\frac{\partial \hat{\theta}}{\partial t} + Dk^2\hat{\theta} = 2\frac{\alpha_\theta}{\sqrt{2\pi}}\frac{\sin\left(\frac{kb}{2}\right)}{k} \ . \tag{C.2}$$

The solution to this equation, considering an initial condition where $\theta = 0$ can be found by an integrating factor :

$$\hat{\theta} = \sqrt{\frac{2}{\pi}}\alpha_\theta t e^{-k^2 Dt}\frac{\sin\left(\frac{kb}{2}\right)}{k} \ , \tag{C.3}$$

which, when taking the inverse Fourier transform yields the simple solution :

$$\theta = \frac{1}{2}\alpha_\theta t\left(\mathrm{erf}\left(\frac{1}{\sqrt{4Dt}}\left(\frac{b}{2} - x\right)\right) + \mathrm{erf}\left(\frac{1}{\sqrt{4Dt}}\left(\frac{b}{2} + x\right)\right)\right) \ , \tag{C.4}$$

and, looking at distances larger than those set by diffusion, we can use the asymptotic form of the error functions, such that :

$$\theta \approx \frac{1}{\sqrt{\pi}}\alpha_\theta t\frac{1}{\sqrt{4Dt}}e^{-\frac{x^2}{4Dt}}b \ . \tag{C.5}$$

C.2 Time delay between regions at different temperatures

Assuming that the bulk of the two regions is oscillating at their characteristic period $\tau e^{\frac{\Delta E}{k_B}\left(\frac{1}{T} - \frac{1}{T_0}\right)}$, we can calculate the delay between the end of cycle 13 at one side and the

other as the difference of the total time that it takes for the cold region (longer period) and the total time that it takes for the warm region (smaller period) :

$$\tau_L = (\tau_{11} + \tau_{12} + \tau_{13}) \left(e^{\frac{\Delta E}{k_B}\left(\frac{1}{T_1} - \frac{1}{T_0}\right)} - e^{\frac{\Delta E}{k_B}\left(\frac{1}{T_2} - \frac{1}{T_0}\right)} \right) , \tag{C.6}$$

where we have assumed that both sides start in phase, and we have ignored the regular mitotic waves triggered by noise that may spread these values. Now, we assume that $T_1 = T_0 - \Delta T/2$ and $T_2 = T_0 + \Delta T/2$. The exponential factor $\Delta E/k_B \sim 9500$, and because temperatures are measured in Kelvin, their variations are not large. Hence, we can perform a Taylor expansion around T_0 in the exponential. At the first order :

$$\tau_L \approx (\tau_{11} + \tau_{12} + \tau_{13}) \frac{\Delta E}{k_B} \frac{\Delta T}{T_0^2} . \tag{C.7}$$

Table C.1 *Model parameters*

Parameter	Notation	Value
Diffusion coefficient	D	$5\,\mu m^2/s$
Cyclin production rate	k_{synth}	$12\,\text{nM}\,\text{min}^{-1}$
Basal cyclin degradation rate	α_{deg}	$0.06\,\text{min}^{-1}$
Cdk1-dependent cyclin degradation rate	β_{deg}	$0.57\,\text{min}^{-1}$
Cdk1 at cyclin degradation half activation	K_{deg}	32.0 nM
Cdk1 degradation Hill coefficient	n_{deg}	5
Basal Cdk1 activation due to Wee1	α_{Wee1}	$0.24\,\text{min}^{-1}$
Cdk1-dependent Cdk1 activation due to Wee1	βWee1	$1.00\,\text{min}^{-1}$
Cdk1 at Wee1 half activation	K_{Wee1}	26.4 nM
Wee1 regulation Hill coefficient	n_{Wee1}	5
Basal Cdk1 inactivation due to Cdc25	α_{Cdc25}	$0.12\,\text{min}^{-1}$
Cdk1-dependent Cdk1 inactivation due to Cdc25	β_{Cdc25}	$0.65\,\text{min}^{-1}$
Cdk1 at Cdc25 half activation	K_{Cdc25}	26.4 nM
Cdc25 activation Hill coefficient	n_{Cdc25}	5
Basal effective Cdc25 inhibition-degradation coefficient	δ_s	$10.0\,\text{min}^{-1}$
Cdc25 inhibitor production rate	α_θ	$1.0\,\text{nM}\,\text{min}^{-1}$
Cdk1 at half value of the Chk1 regulation function	K_{Chk1}	$48\,\text{nM}\,\text{min}^{-1}$
Cdk1-mediated Chk1 regulation Hill coefficient	n_{Chk1}	10
Basal Chk1 activity	h^*	0.9
Titration molecule at Chk1 half activation	K_Y	0.728 nM
Titration molecule production rate	α_Y	$0.5\,\text{nM}\,\text{min}^{-1}$
Titration molecule - importin binding rate	k_{YI}	$5.0\,\text{min}^{-1}$
Importin degradation rate	δ_I	$5.0\,\text{min}^{-1}$
Importin import rate	k_{imp}	$5.0\,\text{min}^{-1}$
Cyclin production chemical noise amplitude	σ_c	0.24
Cdk1 activation chemical noise amplitude	σ_a	0.24
Nuclear envelope breakdown Cdk1 threshold	a^*	29.0 nM
Mitotic exit Cdk1 threshold	a^{**}	14.0 nM
Degradation molecule threshold for transcription	Y^*	0.9 nM

Bibliographie

[1] Atlas Collaboration, "Observation of a new particle in the search for the Standard Model Higgs boson with the ATLAS detector at the LHC," *Physics Letters B*, 2012.

[2] LIGO Scientific Collaboration and Virgo Collaboration, "Observation of Gravitational Waves from a Binary Black Hole Merger," *Physical Review Letters*, 2016.

[3] The Event Horizon Telescope Collaboration, "First M87 Event Horizon Telescope Results. IV. Imaging the Central Supermassive Black Hole," *The Astrophysical Journal Letters*, 2019.

[4] W. Bialek, A. Cavagna, I. Giardina et al., "Statistical mechanics for natural flocks of birds," *Proceedings of the National Academy of Sciences*, 2012.

[5] D. L. Altshuler, W. B. Dickson, J. T. Vance, S. P. Roberts et M. H. Dickinson, "Short-amplitude high-frequency wing strokes determine the aerodynamics of honeybee flight," *Proceedings of the National Academy of Sciences*, 2005.

[6] P. Duhem, *La théorie physique. Son object, sa structure*. 1906.

[7] S. B. Carroll, "Zebra patterns in fly embryos : Activation of stripes or repression of interstripes ?" *Cell*, 1990.

[8] M. D. Petkova, G. Tkačik, W. Bialek, E. F. Wieschaus et T. Gregor, "Optimal Decoding of Cellular Identities in a Genetic Network," *Cell*, 2019.

[9] S. Klumpp, Z. Zhang et T. Hwa, "Growth Rate-Dependent Global Effects on Gene Expression in Bacteria," *Cell*, 2009.

[10] A. Mitchell, G. H. Romano, B. Groisman et al., "Adaptive prediction of environmental changes by microorganisms," *Nature*, 2009.

[11] T. M. Svitkina, E. A. Bulanova, O. Y. Chaga et al., "Mechanism of filopodia initiation by reorganization of a dendritic network," *Journal of Cell Biology*, 2003.

[12] A. Brugués, E. Anon, V. Conte et al., "Forces driving epithelial wound healing," *Nature Physics*, 2014.

[13] G. Reddy, B. I. Shraiman et M. Vergassola, "Sector search strategies for odor trail tracking," *Proceedings of the National Academy of Sciences*, 2022.

[14] N. Rigolli, G. Reddy, A. Seminara et M. Vergassola, "Alternation emerges as a multi-modal strategy for turbulent odor navigation," *eLife*, T. O. Sharpee et R. L. Calabrese, éd., 2022.

[15] S. J. Helms, W. M. Rozemuller, A. C. Costa, L. Avery, G. J. Stephens et T. S. Shimizu, "Modelling the ballistic-to-diffusive transition in nematode motility reveals variation in exploratory behaviour across species," *Journal of The Royal Society Interface*, 2019.

[16] D. W. Thompson, *On Growth and Form*, J. T. Bonner, éd. Cambridge : Cambridge University Press, 1992.

[17] E. Haeckel, *Kunsformen der Natur*. Leipzig und Wien : Verlag des Bibliographischen Instituts, 1899.

[18] Intergovernmental Panel on Climate Change (IPCC), *Climate Change 2022 – Impacts, Adaptation and Vulnerability : Working Group II Contribution to the Sixth Assessment Report of the Intergovernmental Panel on Climate Change*. Cambridge : Cambridge University Press, 2023.

[19] E. B. Mougey, M. O'Reilly, Y. Osheim, O. L. Miller, A. Beyer et B. Sollner-Webb, "The terminal balls characteristic of eukaryotic rRNA transcription units in chromatin spreads are rRNA processing complexes.," *Genes & Development*, 1993.

[20] A. Corsi, B. Wightman et M. Chalfie, "A Transparent Window into Biology : A Primer on Caenorhabditis elegans," *WormBook : the online review of C. elegans biology*, 2015.

[21] L. Rayleigh, "LIX. On convection currents in a horizontal layer of fluid, when the higher temperature is on the under side," *The London, Edinburgh, and Dublin Philosophical Magazine and Journal of Science*, 1916.

[22] Å. Nordlund, R. F. Stein et M. Asplund, "Solar Surface Convection," *Living Reviews in Solar Physics*, 2009.

[23] R. Bailleul, C. Curantz, C. Desmarquet-Trin Dinh, M. Hidalgo, J. Touboul et M. Manceau, "Symmetry breaking in the embryonic skin triggers directional and sequential plumage patterning," *PLOS Biology*, 2019.

[24] A. M. Turing, "The chemical basis of morphogenesis," *Philosophical Transactions of the Royal Society of London. Series B, Biological Sciences*, 1952.

[25] R. Rollin, J.-F. Joanny et P. Sens, "Physical basis of the cell size scaling laws," *eLife*, A. Amir, N. Barkai et J. Lin, éd., 2023.

[26] M. Lacroix, B. Smeets, C. Blanch-Mercader et al., "Emergence of bidirectional cell laning from collective contact guidance," *Nature Physics*, 2024.

[27] G. Peyret, R. Mueller, J. d'Alessandro et al., "Sustained Oscillations of Epithelial Cell Sheets," *Biophysical Journal*, 2019.

[28] M. R. Davidescu, P. Romanczuk, T. Gregor et I. D. Couzin, "Growth produces coordination trade-offs in Trichoplax adhaerens, an animal lacking a central nervous system," *Proceedings of the National Academy of Sciences*, 2023.

[29] C. D. Nobes et A. Hall, "Rho, Rac, and Cdc42 GTPases regulate the assembly of multimolecular focal complexes associated with actin stress fibers, lamellipodia, and filopodia," *Cell*, 1995.

[30] M. Kramar et K. Alim, "Encoding memory in tube diameter hierarchy of living flow network," *Proceedings of the National Academy of Sciences*, 2021.

[31] S. H. LARSEN, R. W. READER, E. N. KORT, W.-W. TSO et J. ADLER, "Change in direction of flagellar rotation is the basis of the chemotactic response in Escherichia coli," *Nature*, 1974.

[32] K. Wagh, M. Ishikawa, D. A. Garcia, D. A. Stavreva, A. Upadhyaya et G. L. Hager, "Mechanical Regulation of Transcription : Recent Advances," *Trends in Cell Biology*, 2021.

[33] E. Hannezo et C.-P. Heisenberg, "Mechanochemical Feedback Loops in Development and Disease," *Cell*, 2019.

[34] A. Bailles, E. W. Gehrels et T. Lecuit, "Mechanochemical Principles of Spatial and Temporal Patterns in Cells and Tissues," *Annual Review of Cell and Developmental Biology*, 2022.

[35] M. Saadaoui, D. Rocancourt, J. Roussel, F. Corson et J. Gros, "A tensile ring drives tissue flows to shape the gastrulating amniote embryo," *Science*, 2020.

[36] A. E. Bruce, "Zebrafish epiboly : Spreading thin over the yolk," *Developmental Dynamics*, 2016.

[37] P. Nurse, "A Long Twentieth Century of the Cell Cycle and Beyond," *Cell*, 2000.

[38] M.-L. Dequéant et O. Pourquié, "Segmental patterning of the vertebrate embryonic axis," *Nature Reviews Genetics*, 2008.

[39] S. H. Strogatz, *Nonlinear Dynamics and Chaos : With Applications to Physics, Biology, Chemistry and Engineering*. Westview Press, 2000.

[40] I. Prigogine et R. Lefever, "Symmetry Breaking Instabilities in Dissipative Systems. II," *The Journal of Chemical Physics*, 1968.

[41] J. J. Tyson, "What Everyone Should Know About the Belousov-Zhabotinsky Reaction," in *Frontiers in Mathematical Biology*, S. A. Levin, éd., Berlin, Heidelberg : Springer Berlin Heidelberg, 1994, isbn : 978-3-642-50124-1.

[42] M. Gardner, "MATHEMATICAL GAMES," *Scientific American*, 1970.

[43] D. Wirtz, K. Konstantopoulos et P. C. Searson, "The physics of cancer : the role of physical interactions and mechanical forces in metastasis," *Nature Reviews Cancer*, 2011.

[44] M. Gemberling, T. J. Bailey, D. R. Hyde et K. D. Poss, "The zebrafish as a model for complex tissue regeneration," *Trends in Genetics*, 2013.

[45] M. C. Vogg, B. Galliot et C. D. Tsiairis, "Model systems for regeneration : Hydra," *Development*, 2019.

[46] G. Serrano Nájera et C. J. Weijer, "Cellular processes driving gastrulation in the avian embryo," *Mechanisms of Development*, 2020.

[47] P. Caldarelli, A. Chamolly, O. Alegria-Prévot, J. Gros et F. Corson, "Self-organized tissue mechanics underlie embryonic regulation," *bioRxiv*, 2021.

[48] S. Lepage et A. Bruce, "Zebrafish epiboly : mechanics and mechanisms," en, *The International Journal of Developmental Biology*, 2010.

[49] N. I. Petridou, B. Corominas-Murtra, C.-P. Heisenberg et E. Hannezo, "Rigidity percolation uncovers a structural basis for embryonic tissue phase transitions," *Cell*, 2021.

[50] F. B. Hanson et F. R. Ferris, "A quantitative study of fecundity in Drosophila melanogaster," *Journal of Experimental Zoology*, 1929.

[51] M. A. Fernández-Moreno, C. L. Farr, L. S. Kaguni et R. Garesse, "Drosophila melanogaster as a Model System to Study Mitochondrial Biology," in *Mitochondria : Practical Protocols*, D. Leister et J. M. Herrmann, éd., Totowa, NJ : Humana Press, 2007, isbn : 978-1-59745-365-3.

[52] J. A. Farrell et P. H. O'Farrell, "From egg to gastrula : how the cell cycle is remodeled during the Drosophila mid-blastula transition.," eng, *Annual review of genetics*, 2014.

[53] G. von Dassow et G. Schubiger, "How an actin network might cause fountain streaming and nuclear migration in the syncytial Drosophila embryo.," eng, *The Journal of cell biology*, 1994.

[54] V. E. Deneke, A. Puliafito, D. Krueger et al., "Self-Organized Nuclear Positioning Synchronizes the Cell Cycle in Drosophila Embryos," *Cell*, 2019.

[55] V. E. Foe et B. M. Alberts, "Studies of nuclear and cytoplasmic behaviour during the five mitotic cycles that precede gastrulation in Drosophila embryogenesis.," eng, *Journal of cell science*, 1983.

[56] M. Rabinowitz, "Studies on the cytology and early embryology of the egg of Drosophila melanogaster," *Journal of Morphology*, 1941.

[57] P. W. Ingham, "The molecular genetics of embryonic pattern formation in Drosophila," *Nature*, 1988.

[58] S. F. Gilbert 1949- et M. J. F. Barresi 1974-, *Developmental biology*, English, Eleventh edition. Sunderland, Massachusetts : Sinauer Associates, Inc., 2018, isbn : 978-1-60535-470-5 1-60535-470-8.

[59] A. Mazumdar et M. Mazumdar, "How one becomes many : Blastoderm cellularization in Drosophila melanogaster," *BioEssays*, 2002.

[60] M. Leptin, "Gastrulation Movements : the Logic and the Nuts and Bolts," *Developmental Cell*, 2005.

[61] A. W. Shermoen et P. H. O'Farrell, "Progression of the cell cycle through mitosis leads to abortion of nascent transcripts," *Cell*, 1991.

[62] X. Lu, J. Drocco et E. F. Wieschaus, "Cell cycle regulation via inter-nuclear communication during the early embryonic development of Drosophila melanogaster," *Cell Cycle*, 2010.

[63] S. A. Blythe et E. F. Wieschaus, "Zygotic Genome Activation Triggers the DNA Replication Checkpoint at the Midblastula Transition," *Cell*, 2015.

[64] S. Syed, H. Wilky, J. Raimundo, B. Lim et A. A. Amodeo, "The nuclear to cytoplasmic ratio directly regulates zygotic transcription in *Drosophila* through multiple modalities," *Proceedings of the National Academy of Sciences*, 2021.

[65] L. Hayden, A. Chao, V. E. Deneke, M. Vergassola, A. Puliafito et S. Di Talia, "Cullin-5 mutants reveal collective sensing of the nucleocytoplasmic ratio in Drosophila embryogenesis," *Current Biology*, 2022.

[66] C. Hernández-López, A. Puliafito, Y. Xu, Z. Lu, S. Di Talia et M. Vergassola, "Two-fluid dynamics and micron-thin boundary layers shape cytoplasmic flows in early Drosophila embryos," *Proceedings of the National Academy of Sciences*, 2023.

[67] W. SEIFRIZ, "Mechanism of Protoplasmic Movement," *Nature*, 1953.

[68] K. Alim, G. Amselem, F. Peaudecerf, M. P. Brenner et A. Pringle, "Random network peristalsis in Physarum polycephalum organizes fluid flows across an individual," *Proceedings of the National Academy of Sciences*, 2013.

[69] P. Stewart A., "The Organization of Movement in Slime Mold Plasmodia," in *Primitive Motile Systems in Cell Biology (Second Edition)*, R. D. Allen et N. Kamiya, éd., Academic Press, 1964, isbn : 978-0-12-395681-1.

[70] S. Nonaka, Y. Tanaka, Y. Okada et al., "Randomization of Left–Right Asymmetry due to Loss of Nodal Cilia Generating Leftward Flow of Extraembryonic Fluid in Mice Lacking KIF3B Motor Protein," *Cell*, 1998.

[71] N. Hirokawa, Y. Tanaka, Y. Okada et S. Takeda, "Nodal Flow and the Generation of Left-Right Asymmetry," *Cell*, 2006.

[72] S. Shamipour, S. Caballero-Mancebo et C.-P. Heisenberg, "Cytoplasm's Got Moves," *Developmental Cell*, 2021.

[73] R. E. Goldstein et J.-W. van de Meent, "A physical perspective on cytoplasmic streaming," *Interface Focus*, 2015.

[74] W. Lu, M. Lakonishok, A. S. Serpinskaya, D. Kirchenbüechler, S.-C. Ling et V. I. Gelfand, "Ooplasmic flow cooperates with transport and anchorage in Drosophila oocyte posterior determination," *Journal of Cell Biology*, 2018.

[75] S. Ganguly, L. S. Williams, I. M. Palacios et R. E. Goldstein, "Cytoplasmic streaming in Drosophila oocytes varies with kinesin activity and correlates with the microtubule cytoskeleton architecture," *Proceedings of the National Academy of Sciences*, 2012.

[76] J. B. Glotzer, R. Saffrich, M. Glotzer et A. Ephrussi, "Cytoplasmic flows localize injected oskar RNA in Drosophila oocytes," *Current Biology*, 1997.

[77] M. E. Quinlan, "Cytoplasmic Streaming in the Drosophila Oocyte," *Annual Review of Cell and Developmental Biology*, 2016.

[78] U. Wolke, E. A. Jezuit et J. R. Priess, "Actin-dependent cytoplasmic streaming in C. elegansoogenesis," *Development*, 2007.

[79] N. T. Chartier, A. Mukherjee, J. Pfanzelter et al., "A hydraulic instability drives the cell death decision in the nematode germline," *Nature Physics*, 2021.

[80] M. Almonacid, M.-E. Terret et M.-H. Verlhac, "Control of nucleus positioning in mouse oocytes," *SI : Nuclear positioning*, 2018.

[81] K. Yi, J. R. Unruh, M. Deng, B. D. Slaughter, B. Rubinstein et R. Li, "Dynamic maintenance of asymmetric meiotic spindle position through Arp2/3-complex-driven cytoplasmic streaming in mouse oocytes," *Nature Cell Biology*, 2011.

[82] N. Klughammer, J. Bischof, N. D. Schnellbächer, A. Callegari, P. Lénárt et U. S. Schwarz, "Cytoplasmic flows in starfish oocytes are fully determined by cortical contractions," *PLOS Computational Biology*, 2018.

[83] E. Nazockdast, A. Rahimian, D. Needleman et M. Shelley, "Cytoplasmic flows as signatures for the mechanics of mitotic positioning," *Molecular Biology of the Cell*, 2017.

[84] R. Niwayama, K. Shinohara et A. Kimura, "Hydrodynamic property of the cytoplasm is sufficient to mediate cytoplasmic streaming in the Caenorhabiditis elegans embryo," *Proceedings of the National Academy of Sciences*, 2011.

[85] A. Royou, W. Sullivan et R. Karess, "Cortical recruitment of nonmuscle myosin II in early syncytial Drosophila embryos : its role in nuclear axial expansion and its regulation by Cdc2 activity.," eng, *The Journal of cell biology*, 2002.

[86] P. H. O'Farrell, "Growing an Embryo from a Single Cell : A Hurdle in Animal Life," *Cold Spring Harbor Perspectives in Biology*, 2015.

[87] ZALOKAR M et ERK I, "DIVISION AND MIGRATION OF NUCLEI DURING EARLY EMBRYOGENESIS OF DROSOPHILA MELANOGASTER.," English, *Journal de microscopie et de biologie cellulaire*, 1976.

[88] T. T. Su, F. Sprenger, P. J. DiGregorio, S. D. Campbell et P. H. O'Farrell, "Exit from mitosis inDrosophila syncytial embryos requires proteolysis and cyclin degradation, and is associated with localized dephosphorylation," *Genes & Development*, 1998.

[89] J.-y. Huang et J. W. Raff, "The disappearance of cyclin B at the end of mitosis is regulated spatially in Drosophila cells," *The EMBO Journal*, 1999.

[90] J. W. Raff, K. Jeffers et J.-y. Huang, "The roles of Fzy/Cdc20 and Fzr/Cdh1 in regulating the destruction of cyclin B in space and time," *Journal of Cell Biology*, 2002.

[91] L. Hayden, W. Hur, M. Vergassola et S. Di Talia, "Manipulating the nature of embryonic mitotic waves," *Current Biology*, 2022.

[92] B. He, K. Doubrovinski, O. Polyakov et E. Wieschaus, "Apical constriction drives tissue-scale hydrodynamic flow to mediate cell elongation," *Nature*, 2014.

[93] W. Alt et M. Dembo, "Cytoplasm dynamics and cell motion : two-phase flow models.," eng, *Mathematical biosciences*, 1999.

[94] G. T. Charras, J. C. Yarrow, M. A. Horton, L. Mahadevan et T. J. Mitchison, "Non-equilibration of hydrostatic pressure in blebbing cells," *Nature*, 2005.

[95] T. Mitchison, G. Charras et L. Mahadevan, "Implications of a poroelastic cytoplasm for the dynamics of animal cell shape," *Cell Shape and Tissue Morphogenesis*, 2008.

[96] E. Moeendarbary, L. Valon, M. Fritzsche et al., "The cytoplasm of living cells behaves as a poroelastic material," *Nature Materials*, 2013.

[97] E. M. Purcell, "Life at low Reynolds number," *American Journal of Physics*, 1977.

[98] J. C. Liao, "A review of fish swimming mechanics and behaviour in altered flows," *Philosophical Transactions of the Royal Society B : Biological Sciences*, 2007.

[99] H. E. Guderley et I. Tremblay, "Chapter 12 - Swimming in Scallops," in *Developments in Aquaculture and Fisheries Science*, S. E. Shumway et G. J. Parsons, éd., Elsevier, 2016, isbn : 0167-9309.

[100] R. M. Macnab, "Bacterial flagella rotating in bundles : a study in helical geometry.," *Proceedings of the National Academy of Sciences*, 1977.

[101] T. J. Böddeker, S. Karpitschka, C. T. Kreis, Q. Magdelaine et O. Bäumchen, "Dynamic force measurements on swimming Chlamydomonas cells using micropipette force sensors," *Journal of The Royal Society Interface*, 2020.

[102] L. G. Tilney et D. A. Portnoy, "Actin filaments and the growth, movement, and spread of the intracellular bacterial parasite, Listeria monocytogenes.," *Journal of Cell Biology*, 1989.

[103] F. Gerbal, P. Chaikin, Y. Rabin et J. Prost, "An Elastic Analysis of Listeria monocytogenes Propulsion," *Biophysical Journal*, 2000.

[104] A. Paluck, J. Osan, L. Hollingsworth, S. N. Talukdar, A. A. Saegh et M. Mehedi, "Role of ARP2/3 Complex-Driven Actin Polymerization in RSV Infection," *Pathogens*, 2022.

[105] K. Takeya, X. Wang, C. Sutherland et al., "The involvement of myosin regulatory light chain diphosphorylation in sustained vasoconstriction under pathophysiological conditions," *Journal of Smooth Muscle Research*, 2014.

[106] H. Yu, L. Ma, Y. Yang et Q. Cui, "Mechanochemical Coupling in the Myosin Motor Domain. I. Insights from Equilibrium Active-Site Simulations," *PLOS Computational Biology*, 2007.

[107] F. Nedelec et D. Foethke, "Collective Langevin dynamics of flexible cytoskeletal fibers," *New Journal of Physics*, 2007.

[108] J. Prost, F. Jülicher et J.-F. Joanny, "Active gel physics," *Nature Physics*, 2015.

[109] M. P. Murrell et M. L. Gardel, "F-actin buckling coordinates contractility and severing in a biomimetic actomyosin cortex," *Proceedings of the National Academy of Sciences*, 2012.

[110] M. Murrell, P. W. Oakes, M. Lenz et M. L. Gardel, "Forcing cells into shape : the mechanics of actomyosin contractility," *Nature Reviews Molecular Cell Biology*, 2015.

[111] D. S. Banerjee, A. Munjal, T. Lecuit et M. Rao, "Actomyosin pulsation and flows in an active elastomer with turnover and network remodeling," *Nature Communications*, 2017.

[112] D. Acheson, *Elementary Fluid Dynamics*. Clarendon Press, 1990, isbn : 978-0-19-859679-0.

[113] H. Kishi, L.-H. Ye, A. Nakamura et al., "Structure and Function of Smooth Muscle Myosin Light Chain Kinase," in *Mechanisms of Work Production and Work Absorption in Muscle*, H. Sugi et G. H. Pollack, éd., Boston, MA : Springer US, 1998, isbn : 978-1-4684-6039-1.

[114] J. Baker, W. Theurkauf et G. Schubiger, "Dynamic changes in microtubule configuration correlate with nuclear migration in the preblastoderm Drosophila embryo," *Journal of Cell Biology*, 1993.

[115] O. Deshpande, J. de-Carvalho, D. V. Vieira et I. A. Telley, "Astral microtubule cross-linking safeguards uniform nuclear distribution in the Drosophila syncytium," *Journal of Cell Biology*, 2021.

[116] L. A. Stiffler, J. Y. Ji, S. Trautmann, C. Trusty et G. Schubiger, "Cyclin A and B functions in the early Drosophila embryo.," eng, *Development (Cambridge, England)*, 1999.

[117] F. Verde, M. Dogterom, E. Stelzer, E. Karsenti et S. Leibler, "Control of microtubule dynamics and length by cyclin A- and cyclin B-dependent kinases in Xenopus egg extracts.," eng, *The Journal of cell biology*, 1992.

[118] P.-F. Lenne, J.-F. Rupprecht et V. Viasnoff, "Cell Junction Mechanics beyond the Bounds of Adhesion and Tension," *Developmental Cell*, 2021.

[119] O. Grimm, M. Coppey et E. Wieschaus, "Modelling the Bicoid gradient," *Development*, 2010.

[120] W. Driever et C. Nüsslein-Volhard, "A gradient of bicoid protein in Drosophila embryos," *Cell*, 1988.

[121] W. Driever et C. Nüsslein-Volhard, "The bicoid protein determines position in the Drosophila embryo in a concentration-dependent manner," *Cell*, 1988.

[122] D. S. Johnston et C. Nüsslein-Volhard, "The origin of pattern and polarity in the Drosophila embryo," *Cell*, 1992.

[123] T. Gregor, W. Bialek, R. R. d. R. van Steveninck, D. W. Tank et E. F. Wieschaus, "Diffusion and scaling during early embryonic pattern formation," *Proceedings of the National Academy of Sciences*, 2005.

[124] I. Hecht, W.-J. Rappel et H. Levine, "Determining the scale of the Bicoid morphogen gradient," *Proceedings of the National Academy of Sciences*, 2009.

[125] S. C. Little, G. Tkačik, T. B. Kneeland, E. F. Wieschaus et T. Gregor, "The Formation of the Bicoid Morphogen Gradient Requires Protein Movement from Anteriorly Localized mRNA," *PLOS Biology*, 2011.

[126] I. Viktorinová, T. König, K. Schlichting et C. Dahmann, "The cadherin Fat2 is required for planar cell polarity in the Drosophila ovary," *Development*, 2009.

[127] K. Barlan, M. Cetera et S. Horne-Badovinac, "Fat2 and Lar Define a Basally Localized Planar Signaling System Controlling Collective Cell Migration," *Developmental Cell*, 2017.

[128] S. J. Streichan, M. F. Lefebvre, N. Noll, E. F. Wieschaus et B. I. Shraiman, "Global morphogenetic flow is accurately predicted by the spatial distribution of myosin motors," *eLife*, F. Jülicher, éd., 2018.

[129] N. J. Carroll, K. H. Jensen, S. Parsa, N. M. Holbrook et D. A. Weitz, "Measurement of Flow Velocity and Inference of Liquid Viscosity in a Microfluidic Channel by Fluorescence Photobleaching," *Langmuir*, 2014.

[130] S. Berg, D. Kutra, T. Kroeger et al., "ilastik : interactive machine learning for (bio)image analysis," *Nature Methods*, 2019.

[131] D. N. Arnold, F. Brezzi et M. Fortin, "A stable finite element for the stokes equations," *CALCOLO*, 1984.

[132] K. Doubrovinski, M. Swan, O. Polyakov et E. F. Wieschaus, "Measurement of cortical elasticity in Drosophila melanogaster embryos using ferrofluids," *Proceedings of the National Academy of Sciences*, 2017.

[133] M. Chertkov, L. Kroc, F. Krzakala, M. Vergassola et L. Zdeborová, "Inference in particle tracking experiments by passing messages between images," *Proceedings of the National Academy of Sciences*, 2010.

[134] D. MacKay, D. Kay et Cambridge University Press, *Information Theory, Inference and Learning Algorithms*. Cambridge University Press, 2003, isbn : 978-0-521-64298-9.

[135] M. Bayati, D. Shah et M. Sharma, "Max-Product for Maximum Weight Matching : Convergence, Correctness, and LP Duality," *IEEE Transactions on Information Theory*, 2008.

[136] J. S. Bois, F. Jülicher et S. W. Grill, "Pattern Formation in Active Fluids," *Physical Review Letters*, 2011.

[137] M. F. Staddon, E. M. Munro et S. Banerjee, "Pulsatile contractions and pattern formation in excitable actomyosin cortex," *PLOS Computational Biology*, 2022.

[138] L. Barberi et K. Kruse, "Localized States in Active Fluids," *Phys. Rev. Lett.*, 2023.

[139] A. De Wit, "Chemo-Hydrodynamic Patterns and Instabilities," *Annual Review of Fluid Mechanics*, 2020.

[140] M. Almonacid, W. W. Ahmed, M. Bussonnier et al., "Active diffusion positions the nucleus in mouse oocytes," *Nature Cell Biology*, 2015.

[141] R. B. Vallee et S. A. Stehman, "How dynein helps the cell find its center : a servomechanical model," *Trends in Cell Biology*, 2005.

[142] A. J. Jimenez, A. Schaeffer, C. De Pascalis et al., "Acto-myosin network geometry defines centrosome position," *Current Biology*, 2021.

[143] T. Vicsek, A. Czirók, E. Ben-Jacob, I. Cohen et O. Shochet, "Novel Type of Phase Transition in a System of Self-Driven Particles," *Phys. Rev. Lett.*, 1995.

[144] J. Toner et Y. Tu, "Long-Range Order in a Two-Dimensional Dynamical $\mathrmXY$ Model : How Birds Fly Together," *Phys. Rev. Lett.*, 1995.

[145] T. H. Tan, A. Mietke, J. Li et al., "Odd dynamics of living chiral crystals," *Nature*, 2022.

[146] S. Ketzetzi, M. Rinaldin, P. Dröge, J. d. Graaf et D. J. Kraft, "Activity-induced interactions and cooperation of artificial microswimmers in one-dimensional environments," *Nature Communications*, 2022.

[147] A. Bahat, I. Tur-Kaspa, A. Gakamsky, L. C. Giojalas, H. Breitbart et M. Eisenbach, "Thermotaxis of mammalian sperm cells : A potential navigation mechanism in the female genital tract," *Nature Medicine*, 2003.

[148] M. Sekiguchi, S. Kameda, S. Kurosawa, M. Yoshida et K. Yoshimura, "Thermotaxis in Chlamydomonas is brought about by membrane excitation and controlled by redox conditions," *Scientific Reports*, 2018.

[149] G. Zhong, L. Kroo et M. Prakash, "Thermotaxis in an apolar, non-neuronal animal," *Journal of The Royal Society Interface*, 2023.

[150] J. N. Wilking, V. Zaburdaev, M. De Volder, R. Losick, M. P. Brenner et D. A. Weitz, "Liquid transport facilitated by channels in Bacillus subtilis biofilms," *Proceedings of the National Academy of Sciences*, 2013.

[151] E. C. Hammer, C. Arellano-Caicedo, P. M. Mafla-Endara et al., "Hyphal exploration strategies and habitat modification of an arbuscular mycorrhizal fungus in microengineered soil chips," *Fungal Ecology*, 2024.

[152] A. C. Martin, M. Kaschube et E. F. Wieschaus, "Pulsed contractions of an actin–myosin network drive apical constriction," *Nature*, 2009.

[153] E. W. Gehrels, B. Chakrabortty, M.-E. Perrin, M. Merkel et T. Lecuit, "Curvature gradient drives polarized tissue flow in the Drosophila embryo," *Proceedings of the National Academy of Sciences*, 2023.

[154] R. Milo et R. Phillips, *Cell Biology by the Numbers*. 2015.

[155] V. E. Deneke, A. Melbinger, M. Vergassola et S. Di Talia, "Waves of Cdk1 Activity in S Phase Synchronize the Cell Cycle in Drosophila Embryos," *Developmental Cell*, 2016.

[156] J. B. Chang et J. E. Ferrell Jr, "Mitotic trigger waves and the spatial coordination of the Xenopus cell cycle," *Nature*, 2013.

[157] M. Vergassola, V. E. Deneke et S. D. Talia, "Mitotic waves in the early embryogenesis of *Drosophila* : Bistability traded for speed," *Proceedings of the National Academy of Sciences*, 2018.

[158] S. Balachandra, S. Sarkar et A. A. Amodeo, "The Nuclear-to-Cytoplasmic Ratio : Coupling DNA Content to Cell Size, Cell Cycle, and Biosynthetic Capacity," *Annual Review of Genetics*, 2022.

[159] X. Lu, J. M. Li, O. Elemento, S. Tavazoie et E. F. Wieschaus, "Coupling of zygotic transcription to mitotic control at the Drosophila mid-blastula transition," *Development*, 2009.

[160] Y. Shindo et A. A. Amodeo, "Dynamics of Free and Chromatin-Bound Histone H3 during Early Embryogenesis," *Current Biology*, 2019.

[161] Y. Shindo et A. A. Amodeo, "Excess histone H3 is a competitive Chk1 inhibitor that controls cell-cycle remodeling in the early Drosophila embryo," *Current Biology*, 2021.

[162] J. Crapse, N. Pappireddi, M. Gupta, S. Y. Shvartsman, E. Wieschaus et M. Wühr, "Evaluating the Arrhenius equation for developmental processes," *Molecular Systems Biology*, 2021.

[163] G. Petavy, J. David, P. Gibert et B. Moreteau, "Viability and rate of development at different temperatures in Drosophila : a comparison of constant and alternating thermal regimes," *Journal of Thermal Biology*, 2001.

[164] S. G. Kuntz et M. B. Eisen, "Drosophila Embryogenesis Scales Uniformly across Temperature in Developmentally Diverse Species," *PLOS Genetics*, 2014.

[165] J. Chong, C. Amourda et T. E. Saunders, "Temporal development of Drosophila embryos is highly robust across a wide temperature range," *Journal of The Royal Society Interface*, 2018.

[166] E. M. Lucchetta, J. H. Lee, L. A. Fu, N. H. Patel et R. F. Ismagilov, "Dynamics of Drosophila embryonic patterning network perturbed in space and time using microfluidics," *Nature*, 2005.

[167] E. M. Lucchetta, M. S. Munson et R. F. Ismagilov, "Characterization of the local temperature in space and time around a developing Drosophila embryo in a microfluidic device," *Lab on a Chip*, 2006.

[168] Z. Bai, H. Bao, Y. Yuan, X. Yang, Y. Xi et M. Wang, "Real-time observation of perturbation of a Drosophila embryo's early cleavage cycles with microfluidics," *Analytica Chimica Acta*, 2017.

[169] E. M. Lucchetta, M. E. Vincent et R. F. Ismagilov, "A Precise Bicoid Gradient Is Nonessential during Cycles 11–13 for Precise Patterning in the Drosophila Blastoderm," *PLOS ONE*, 2008.

[170] Z. Lv, J. Rosenbaum, S. Mohr et al., "The Emergent Yo-yo Movement of Nuclei Driven by Cytoskeletal Remodeling in Pseudo-synchronous Mitotic Cycles," *Current Biology*, 2020.

[171] D. T. Gillespie, "Stochastic Simulation of Chemical Kinetics," *Annual Review of Physical Chemistry*, 2007.

[172] U. Strausfeld, J. C. Labbé, D. Fesquet et al., "Dephosphorylation and activation of a p34cdc2/cyclin B complex in vitro by human CDC25 protein," *Nature*, 1991.

[173] L. L. Parker et H. Piwnica-Worms, "Inactivation of the p34cdc2-Cyclin B Complex by the Human WEE1 Tyrosine Kinase," *Science*, 1992.

[174] C. McGowan et P. Russell, "Cell cycle regulation of human WEE1.," *The EMBO Journal*, 1995.

[175] I. Hoffmann, P. Clarke, M. Marcote, E. Karsenti et G. Draetta, "Phosphorylation and activation of human cdc25-C by cdc2–cyclin B and its involvement in the self-amplification of MPF at mitosis.," *The EMBO Journal*, 1993.

[176] S. Y. Kim et J. E. Ferrell, "Substrate Competition as a Source of Ultrasensitivity in the Inactivation of Wee1," *Cell*, 2007.

[177] N. B. Trunnell, A. C. Poon, S. Y. Kim et J. E. Ferrell, "Ultrasensitivity in the Regulation of Cdc25C by Cdk1," *Molecular Cell*, 2011.

[178] Q. Yang et J. E. Ferrell, "The Cdk1–APC/C cell cycle oscillator circuit functions as a time-delayed, ultrasensitive switch," *Nature Cell Biology*, 2013.

[179] M. Patil, N. Pabla et Z. Dong, "Checkpoint kinase 1 in DNA damage response and cell cycle regulation," *Cellular and Molecular Life Sciences*, 2013.

[180] L. Knoblochova, T. Duricek, M. Vaskovicova et al., "CHK1-CDC25A-CDK1 regulate cell cycle progression and protect genome integrity in early mouse embryos," *EMBO reports*, 2023.

[181] J. J. Tyson, "Modeling the cell division cycle : cdc2 and cyclin interactions.," *Proceedings of the National Academy of Sciences*, 1991.

[182] B. Novak et J. J. Tyson, "Numerical analysis of a comprehensive model of M-phase control in Xenopus oocyte extracts and intact embryos," *Journal of Cell Science*, 1993.

[183] Y. Shindo et A. A. Amodeo, "Modeling the role for nuclear import dynamics in the early embryonic cell cycle," *Biophysical Journal*, 2021.

[184] S. Di Talia, R. She, S. A. Blythe, X. Lu, Q. F. Zhang et E. F. Wieschaus, "Posttranslational Control of Cdc25 Degradation Terminates Drosophila's Early Cell-Cycle Program," *Current Biology*, 2013.

[185] L. A. Johnston, "Cell cycle : The trouble with tribbles," *Current Biology*, 2000.

[186] J. A. Farrell et P. H. O'Farrell, "Mechanism and Regulation of Cdc25/Twine Protein Destruction in Embryonic Cell-Cycle Remodeling," *Current Biology*, 2013.

[187] Melissa Rinaldin, Alison Kickuth, Benjamin Dalton, Yitong Xu, Stefano Di Talia et Jan Brugués, "Robust cytoplasmic partitioning by solving an intrinsic cytoskeletal instability," *bioRxiv*, 2024.

[188] Y. Xu, A. Chao, M. Rinaldin, A. Kickuth, J. Brugués et S. D. Talia, "The cell cycle oscillator and spindle length set the speed of chromosome separation in Drosophila embryos," *bioRxiv*, 2024.

[189] D. Di Pietro et A. Ern, *Mathematical Aspects of Discontinuous Galerkin Methods*. 2012, isbn : 978-3-642-22979-4.

[190] S. Redner, *A Guide to First-Passage Processes*. Cambridge : Cambridge University Press, 2001, isbn : 978-0-521-65248-3.

Claudio HERNÁNDEZ-LÓPEZ **26ème septembre 2024**

Sujet : La Physique du Développement Précoce de la Drosophile

Résumé : Cette thèse porte sur le développement embryonnaire de la Drosophile depuis un point de vue physique. Les organismes multicellulaires ont de gros défis à surmonter : leur développement doit aboutir à une grande variété de formes et de tissus qui se différentient à des positions spécifiques à partir d'une céllule initiale, et ce de manière reproductible. La Drosophile Melanogaster est depuis longtemps étudiée, ce qui en fait un terrain de jeu parfait pour utiliser les outils de la physique afin de comprendre l'ensemble de procesus qui rendent cela possible, en particulier le couplage entre la biochimique et la mécanique. Le chapitre I introduit la biophysique et son approche, caractérise le développement embryonnaire des organismes multicellulaires, et décrit les premières phases du développement de la mouche. Le chapitre II aborde la modélisation des écoulements cytoplasmiques produits par des contractions d'actomyosine quelques cycles cellulaires après la fertilisation, grâce à un couplage méchanochimique noyaux-cortex. Le modèle reproduit les observations expérimentales sur la forme des écoulements, leur amplitude et le transport des noyaux. Le chapitre III aborde les résultats théoriques sur les écoulements décrits dans le chapitre II, en introduisant un modèle simplifié. Le modèle explicite des expressions sur la puissance des écoulements et le mouvement résultant des noyaux pour différentes géometries, et fait des prédictions sur la stabilité des distributions de myosine et la formation de motifs. Le chapitre IV traite des cycles nucléaires qui précèdent la gastrulation. Après la diffusion des noyeaux dans l'oeuf, ils atteignent la cortex embryonnaire, et l'horloge cellulaire qui contrôle les divisions se ralentissent en préparation à la gastrulation. Des expériences ont trouvé que la dynamique des noyaux dépend de la densité nucléaire et le profil de température dans l'oeuf. On explore un modèle qui reproduit des observations sur la propagation des ondes mitotiques dans des embryons type sauvage et mutants. On fait ainsi des prédictions pour des expériences futures.

Mots clés : Biophysique, Biologie du développement, Drosophile, Actomyosine, Écoulements multiphasiques, Oscillateurs non linéaires

Subject : The Physics of Early Drosophila Development

Abstract: This work presents a physics approach to the early embryonic development of Drosophila. The development of multicellular organisms must tackle diverse challenges, in particular, producing a great variety of shapes and tissues that differentiate in specific locations starting from a single cell, in a robust way. Orchestrating all of this requires the interplay between biochemistry and mechanics, hence the relevance of the physics toolkit to integrate these elements. These ideas will be explored in a well-established model system in biology, the fruit fly Drosophila Melanogaster. Chapter I introduces general notions of biophysics and its approach, characterizes the embryonic development of multicellular organisms, and gives an overview of the early development of the fruit fly. Chapter II describes the modeling of cytoplasmic flows produced by actomyosin contractions a few cellular cycles after fertilization, controlled by a mechanochemical coupling between the nuclei and the cortex. The model reproduces experimental observations on the flow shape, amplitude, and nuclear transport. Chapter III introduces a simplified model that allows for a theoretical treatment of the cytoplasmic flows described in Chapter II. We obtain analytical expressions of the strength and shape of the flows and the timescale of nuclear centering for different geometries and make predictions on the stability of myosin distribution and pattern formation. Chapter IV describes the pre-gastrulating nuclear cycles, where after having spread in the bulk of the embryo, the nuclei migrate to the cortex and the cell cycle slows down in preparation for gastrulation. Experiments have shown that the dynamics of the nuclei at the cortex depend on nuclear density and the temperature profile in the embryo. We explore a model that reproduces experimental observations in wild-type and mutant embryos, particularly considering the spreading of mitotic waves, and make predictions that suggest new experiments.

Keywords : Biophysics, Developmental biology, Drosophila, Actomyosin, Multiphase flows, Nonlinear oscillators